IDŐJÁRÁS

QUARTERLY JOURNAL
OF THE HUNGARIAN METEOROLOGICAL SERVICE

CONTENTS

****

VOL. 119 * NO. 4 * OCTOBER – DECEMBER 2015

IDŐJÁRÁS

Quarterly Journal of the Hungarian Meteorological Service

Editorial Office: Kitaibel P.u. 1, H-1024 Budapest, Hungary
P.O. Box 38, H-1525 Budapest, Hungary
E-mail: journal.idojaras@met.hu
Fax: (36-1) 346-4669

Indexed and abstracted in Science Citation Index Expanded™ and Journal Citation Reports/Science Edition
Covered in the abstract and citation database SCOPUS®

Subscription by mail:
IDŐJÁRÁS, P.O. Box 38, H-1525 Budapest, Hungary
E-mail: journal.idojaras@met.hu

IDŐJÁRÁS

Quarterly Journal of the Hungarian Meteorological Service
Vol. 119, No. 4, October – December, 2015, pp. 425–441

Climatic threats determining future adaptive forest management – a case study of Zala County

Borbála Gálos[1]*, Ernő Führer[2], Kornél Czimber[3], Krisztina Gulyás[1], András Bidló[1], Andreas Hänsler[4], Daniela Jacob[4], and Csaba Mátyás[1]

[1] *Institute of Environmental and Earth Sciences, Faculty of Forestry, University of West Hungary, Bajcsy-Zs. u. 4, 9400 Sopron, Hungary*

[2] *National Agricultural Research and Innovation Centre, Forest Research Institute, Paprét 17, 9400 Sopron, Hungary*

[3] *Institute of Geomatics and Civil Engineering, Faculty of Forestry, University of West Hungary, Bajcsy-Zs. u. 4, 9400 Sopron, Hungary*

[4] *Climate Service Center 2.0, Germany – eine Einrichtung am Helmholtz-Zentrum Geesthacht, Fischertwiete 1, 20095 Hamburg, Germany*

* *Corresponding authors E-mail: galos.borbala@emk.nyme.hu*

(Manuscript received in final form May 20, 2015)

Abstract— Research of future climate tendencies is a precondition for appropriate climate change adaptation strategies in forestry and agriculture. The aim of this paper is to investigate the expected probability and magnitude of threatening climate conditions that are of primary importance in terms of forest management. Until 2100, precipitation and temperature results of an ensemble of 12 regional climate model simulations as well as derived indicators (e.g., Forestry Aridity Index and Ellenberg's climate quotient) have been analyzed for the A1B emission scenario. For the case study area in Southwest Hungary (Zala County), projections indicate an increasing tendency of warming and drying of summers towards the end of the 21st century. In the period 2071–2100, decrease of summer precipitation sum may exceed 25% compared to 1981–2010. Both extreme droughts and heavy precipitation events are expected to be more frequent. Consequently, the already observed climate change impacts and damages in forestry are very likely to occur with higher probability and severity. Including these results, a GIS-based "Agroclimate" decision support system is under development that contains a coherent data chain from climate change simulations, through impact assessments to adaptation support in order to provide quantified information on the possible yield potential and production risk for sustainable forest management.

Key-words: regional climate modeling, climate change impact, forest ecosystem, adaptation, decision support

1. Introduction

1.1. Climatic extremes threatening forests in the Carpathian Basin

The Carpathian Basin is considered to be highly sensitive and vulnerable to climate change and the related increase of the probability and intensity of extreme events. Droughts are recurrent features in the climate of the region, and relatively high amounts of precipitation is required to recover from a severe dry period (*Antofie et al.,* 2015). For the high drought risk, climate change, land cover changes, and intensive land use jointly are responsible (*Spinoni et al.,* 2013).

Precipitation is the determining and limiting factor of the distribution of climate dependent tree species in the forest/grassland transition zone ("xeric limits"; *Mátyás,* 2009) in Eastern-Central Europe and Southeast Europe. Primarily consecutive drought periods threaten the survival and adaptation of forest ecosystems (*Mátyás,* 2009; *Mátyás et al.,* 2010). In the last 50 years, the frequency, severity, and duration of extremely dry and warm weather events have increased (*Szinell et al.,* 1998; *Spinoni et al.,* 2013), their impacts on the most sensitive tree species are already visible.

Summer droughts of the last decades (especially in 1983–1995 and 2000–2003) have led to vitality loss of beech forests and to the drastic reduction of their climatically suitable niche in Hungary (*Berki et al.,* 2009). Health status decline has been observed also in sessile oak stands (*Berki et al.,* 2014). Under drier climate conditions, *Führer et al.,* (2013) found less organic matter production of above-ground dendromass. Climatic extremes are being observed to affect the water uptake of forests from groundwater and the whole water balance of forested catchments (*Gribovszki,* 2014). As result of a drought induced damage chain, increasing number of pests and diseases has been detected in beech and oak forests (*Lakatos* and *Molnár,* 2009; *Csóka* and *Hirka* 2011). Lack of adaptation may lead to increasing forest die-back and mortality (*Mátyás et al.,* 2010; *Czúcz et al.,* 2011; *Rasztovits et al.,* 2014; *Hlásny et al.,* 2014).

1.2. Projected climate tendencies

Regional climate change projections largely agree in a statistically significant warming in all seasons over Europe (*Christensen et al.,* 2007; *Jacob et al.,* 2008; *van der Linden* and *Mitchell,* 2009). The annual precipitation sum shows an increase in the northern and a decrease in the southern regions towards the end of the 21st century. In the transition zone, changes are smaller and statistically not significant (*Kjellström et al.,* 2011). This zone is projected to shift northwards in summer resulting in a decrease of the precipitation amount in the Carpathian Basin, whereas the southward shift of the transition zone in winter may lead to precipitation increase (*Bartholy et al.,* 2007, 2008; *Jacob et al.,*

2008). Projected increase of warm extremes as well as of drought frequency, magnitude, and length are statistically the most significant in the Southern European regions, whereas the risk of wet extremes is the most pronounced in the northernmost areas of the continent (*Heinrich* and *Gobiet,* 2011). In the Carpathian Basin, more irregular rainfall can lead both to more frequent heavy precipitation events and severe droughts (*Gálos et al.,* 2007; *Szépszó,* 2008; *Pongrácz et al.,* 2014). Recently, in the frame of the World Climate Research Program Coordinated Regional Downscaling Experiment (EURO-CORDEX) initiative, new regional climate projections have been provided for Europe in higher horizontal resolution (*Jacob et al.,* 2013). The results of the multi-model ensemble confirm the above introduced tendencies, the magnitude and the main spatial patterns of the expected climate change, however, they show more spatial details (*Jacob et al.,* 2013; *Vautard et al.,* 2013, 2014).

1.3. Decision support system development

In Hungary, silvicultural technologies and species preferences are prescribed by binding regulation based on climate conditions that are assumed to be constant over time. Severe droughts of the last decades and observed tree mortality shed light on the need to rethink forest management planning. Reliable projections of health status, production, growth, and yield are essential for the next decades in order to decide about sustainable tree species preference and to assess the economic impacts of possible species changes. The "Agroclimate" decision support system will provide coherent, GIS-supported information about the most important regional and local risks and adaptation options for three climate-dependent sectors (forestry, rainfed agriculture, and animal husbandry on nature-close pastures; *Mátyás et al.,* 2013). In the first step, Zala County in Southwest Hungary was selected as pilot region.

This paper introduces the climate part of the decision support system. The aim is to analyze future climate projections that are providing input for the assessment of forest responses to climate change. Special focus is on the expected probability and magnitude of threatening climate conditions that are of primary importance in terms of forest management (Section 3). Examples are shown for application of regional climate model outputs for impact research in the GIS-supported system (Section 4).

2. Sources of climate information and methods for analyzing

2.1. Applied climate data and models

For the period 1961–2010, daily observation series of temperature and precipitation have been used. The gridded data are available from the CARPATCLIM EU-project (www.carpatclim-eu.org, *Lakatos et al.,* 2013) in

$0.1° \times 0.1°$ horizontal resolution. In the project, the MASH (Multiple Analysis of Series for Homogenization; *Szentimrey,* 2011) procedure has been used for homogenization of long-term observation series. Interpolation of the homogenized time series was carried out by applying the MISH (Meteorological Interpolation based on Surface Homogenized data basis; *Szentimrey* and *Bihari,* 2007) method. Since the target region of the CARPATCLIM project does not cover the whole Zala County, data from further stations of the Hungarian Meteorological Service were also involved in the investigations.

For the 21st century, results of 12 regional climate model simulations have been analyzed that were created in the frame of the ENSEMBLES EU FP6 project (www.ensembles-eu.org). The data are accessible at daily time scale, in $0.22° \times 0.22°$ spatial resolution. The models are already validated (*Jacob et al.,* 2008), their uncertainties (related to the model, scenario, boundaries, and the variability of the climate system; *Prein et al.*, 2011) have been investigated and evaluated in many research projects (e.g., *Christensen et al.,* 2007). This ensemble of regional climate change projections for the SRES A1B emission scenario (IPCC, 2007) are considered as state-of-the-art for European climate impact assessments, so far.

2.2. Methods of analyzing

Climate model results have been included in the GIS-based decision support system, transformed into a common grid applying the DigiTerra Map GIS software and its newly developed Climate Database Query Module (*Czimber,* 2014). Inclusion of all available information (e.g., elevation, hydrology, soil and climate conditions, and satellite images of land use, land cover, and forest inventory data) into a geoinformatic system allows the integrated data processing of the different raster and vector layers. It is possible to query data from the database and the map, and to make geostatistical analyses. For finding spatial correlations and developing functions for impact assessments, the latest image processing technologies (fuzzy membership functions based and maximum likelihood classifiers) has been used.

Applying the Climate Database Query Module, monthly, seasonal, and annual temperature means and precipitation sums as well as their means over the vegetation period have been determined using the daily time series of 12 different regional climate models. For calculating general extreme indices (e.g., total number of summer days, hot days, frost days, dry days, heavy precipitation days), minimum and maximum temperatures from 6 models are available. Moderate and severe dry summers have been defined based on *Gálos et al.* (2007). *Table 1* contains the variables and derived indices selected and investigated in this paper.

Table 1. Climate variables and indices analyzed in this study

Temperature means (*T*)	• annual, seasonal, monthly, vegetation period
Derived extreme indices from daily temperature minima (*Tmin*) and temperature maxima (*Tmax*)	• extremely hot days (*Tmax* ≥ 35 °C) • hot days (T*max* ≥ 30 °C) • frost days (*Tmin* < 0 °C) • ice days (*Tmax* < 0 °C)
Precipitation sums (*P*)	• annual, seasonal, monthly, vegetation period
Derived extreme indices from daily precipitation sums	• wet days ($P \geq 20$ mm day^{-1})
Ellenberg's climate quotient (*EQ*; *Ellenberg,* 1988)	$EQ = \frac{T_{July}}{P_{Annual}} * 1000$
Forestry aridity index (*FAI*; *Führer*, 2010)	$FAI = \frac{T_{July-August}}{P_{May-July} + P_{July-August}} * 100$

Projected climate conditions have been analyzed for three 30-year time periods in the 21st century: 2011–2040, 2041–2070, and 2071–2100, respectively. Expected changes of temperature and precipitation as well as of the probability and severity of climate extremes have been determined relative to the reference period 1981–2010.

Results of an ensemble of different regional climate model simulations have been considered rather than one single climate projection. In this way, the spread and robustness of the projections as well as the likelihood of the possible changes can be evaluated (it is not possible to state a concrete value for future climate change in a specific region). According to the IPCC, the change has been categorized as "likely" when 66% of all changes projected through the various models lie within this range.

3. Climate tendencies in Zala County

3.1. Observed climate

Based on meteorological observations, Zala County can be characterized by 10.4 °C annual mean temperature and 717 mm annual precipitation sum for the time period 1981–2010 that has been applied as reference of the projected climate change (*Table 2*). Summer is the warmest (19.7 °C) and wettest (241 mm), whereas winter is the coldest (0.5 °C) and driest (121 mm) among the seasons.

Table 2. Observed temperature and precipitation in Zala County for the time period 1981–2010

	Temperature mean [°C]	Precipitation sum [mm]
Annual	10.4	717
Spring	10.6	162
Summer	19.6	241
Autumn	10.5	193
Winter	0.5	121
Vegetation period	15.9	494

Measured data of Zalaegerszeg (in Zala County) indicate that in the last decade, almost all summers were warmer than the average of 1981–2010 (*Fig. 1*). Extremely dry periods (at the beginning of the 1990s, 2000s, and 2010s) can be clearly detected that could induce the reported drought damages in forestry (Section 1.1). Summers with precipitation sum below the 30-year mean often have extreme high temperatures as well (*Fig. 1*). Observed tendencies of general climate indices (*Table 1*) show that frequency of hot days ($Tmax \geq 30$ °C) and extremely hot days ($Tmax \geq 35$ °C) increased during the investigated time period (*Fig. 2*). Whereas there was only 1 year in the last 8 years when the total number of frost days ($Tmin < 0$ °C) exceeded the long term mean (*Fig. 2*), which indicates the recent warming of the region.

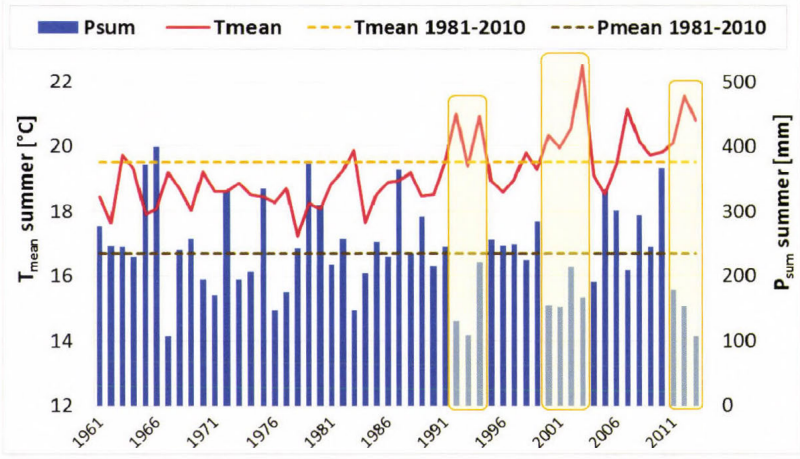

Fig. 1. Summer (June-July-August) temperature means and precipitation sums observed in Zalaegerszeg in the time period 1961–2013.

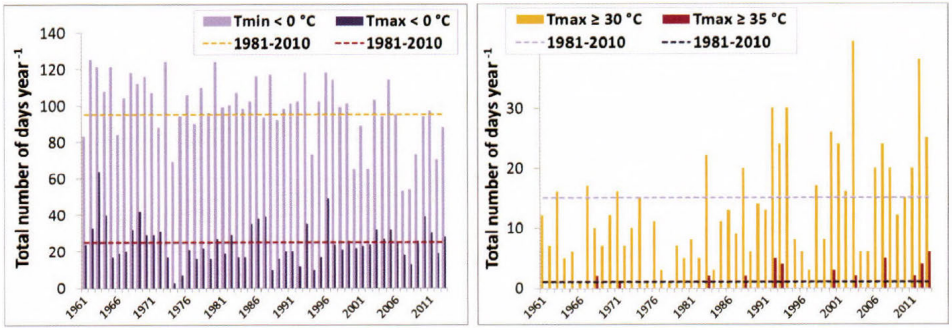

Fig. 2. Left part: total number of frost days ($Tmin < 0$ °C) and ice days ($Tmax < 0$ °C), right part: total number of hot days ($Tmax \geq 30$ °C) and extremely hot days ($Tmax \geq 35$ °C) observed in Zalaegerszeg.

3.2. Projected changes of temperature means and precipitation sums

Regional climate model simulations agree on a significant increase of temperature for all investigated time periods. Annual temperature means are "likely" to be 0.5–1.5 °C higher in 2011–2040, 1.5–2.8 °C higher in 2041–2070, and 2.4–4.2 °C higher in 2071–2100 relative to the time period 1981–2010 (*Fig. 3, Table 2*). The magnitude of warming is expected to increase in all seasons towards the end of the century. Summer temperature means shows the largest changes (for the mean projection of change by up to +3.9 °C in 2071–2100 compared to the reference period), whereas the smallest warming is projected for spring.

Change of annual precipitation sum is not significant, simulation results show a relatively large spread in magnitude and uncertainty in sign (*Fig. 3*). However, the inter-annual distribution of precipitation may change. The winter precipitation amount can be 12% larger for the period 2071–2100. Together with the higher temperatures, more rain is expected instead of snow.

Summers are projected to be significantly drier towards the end of the century. Considering the mean of the simulated changes, decrease of the precipitation sum can exceed the 7%, 12%, and 25%, respectively, in the analyzed 30-year future time periods compared to 1981–2010 (*Fig. 3*). In this case, Zala County might be characterized by similar summer precipitation conditions for the end of the century, like one of the driest regions in Hungary now. From forestry point of view it is important, that less precipitation is projected for the vegetation period, as well. For spring and autumn, expected changes are smaller and less clear in sign. The bandwidth of climate projections is the largest in summer and in the far future time period for both temperature and precipitation.

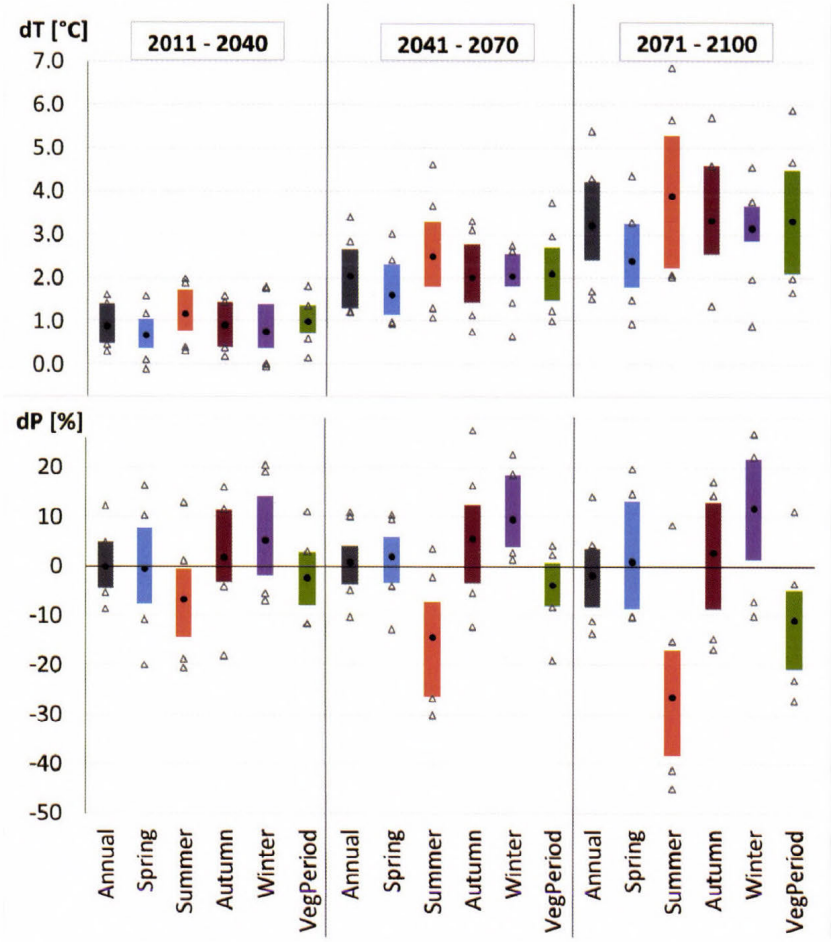

Fig. 3. Projected change of the temperature means (*dT*; top) and precipitation sums (*dP*; bottom) for the 30-year periods in Zala County. Columns: 66% of all projected changes fall within this range. Filled dots: mean projection of 12 regional climate models. Empty dots: bandwidth of all projected changes.

3.3. *Projected changes of the probability of temperature and precipitation extremes*

Additionally to the increase of the 30-year mean temperature, the distribution of its daily values is projected to shift into the warmer direction. That can lead to higher probability of extremely warm days and to less extremely cold days (*Fig. 4*). The "likely" range of the simulation results shows a clear signal in sign. Considering the mean of the projected changes, the total number of hot days

(*Tmax*≥30 °C) can increase by 17 days/year for the middle of the 21st century compared to 1981–2010. It would mean that the period when daily temperature maximums are greater than 30 °C may last 1 month/year. In the time period 1981–2010, only 1 extremely hot day/year (*Tmax*≥35 °C) in average was observed (*Fig. 2*). This amount might be 20 days/year higher by the end of the century. The total number of frost days may decrease by up to 1 month/year for 2071–2100 relative to the reference time period (*Fig. 4*).

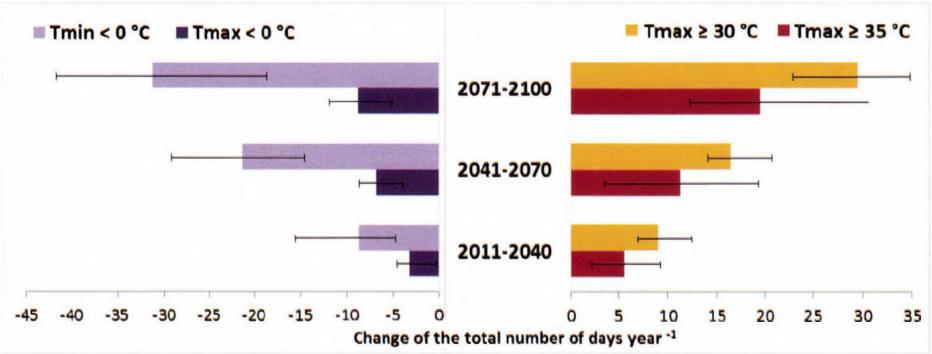

Fig. 4. Left part: mean annual change of the total number of frost days (*Tmin* < 0 °C) and ice days (*Tmax* < 0 °C); right part change of the total number of hot days (*Tmax* ≥ 30 °C) and extremely hot days (*Tmax* ≥ 35 °C) for the 30-year periods in Zala County based on the mean projection of 6 regional climate models. Error bars: 66% of all projected changes fall within this range.

Simulation results show that the change of the temporal distribution of precipitation can result in more intense precipitation events, especially in autumn and winter (*Fig. 5*). The bandwidth of the projections is relatively large on annual timescale, but for 2041–2100, more than 66% of the climate models agree in the direction of the change.

The total number of summer droughts is expected to increase. Not only the probability but also the severity of these events can be higher for the end of the 21st century (*Fig. 6*). For 2071–2100, more than half of the 30-year period can be extremely dry. Consequently, the consecutive dry periods may last longer compared to the end of the 20th century (*Gálos et al.,* 2014). More frequent warm extremes (*Fig. 4*) strengthen the effects of dry conditions due to the higher atmospheric evaporative demand.

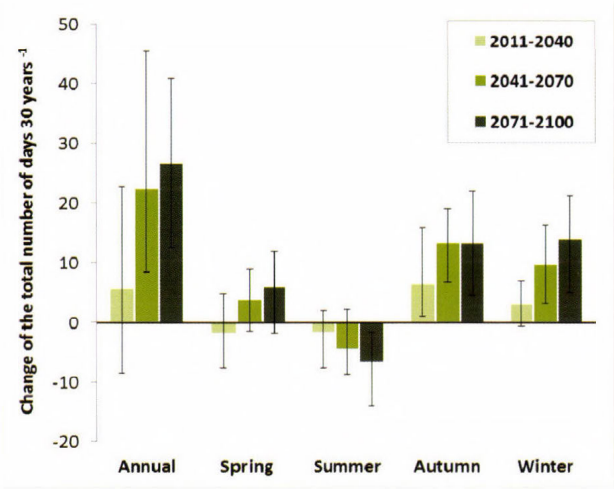

Fig. 5. Change of the total number of wet days ($P > 20$ mm day^{-1}) for the 30-year periods in Zala County based on the mean projection of 12 regional climate models. Error bars: 66% of all projected changes fall within this range.

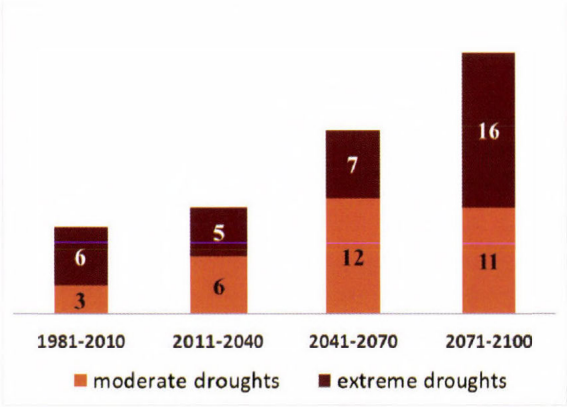

Fig. 6. Total number of summer droughts for the investigated time periods in Zala County (for 1981-2010: observed data, for the future time periods: observed data + simulated changes based on the mean projection of 12 regional climate models. Drought definition is based on *Gálos et al.*, 2007).

4. Application of the results for decision support in the forestry sector

Long term climate projections introduced in Section 3 provide information for two main user-groups: for climate impact researchers and for end users in the affected sectors.

4.1. Climate information for impact research in forestry

In terms of forest management, projection of forest yield conditions is highly important. Their estimation on a geoinformatic basis requires correlations between growth and vitality of species and the determining climatic factors. Different approaches are simultaneously applied in the *D*ecision *S*upport *S*ystem.

- *Forest yield potential.* The Ellenberg's climate quotient (*EQ*; *Ellenberg,* 1988; *Table 1*) has been used for instance to estimate the yield potential of beech. *Fig. 7* shows that beech sites with warmer and dryer conditions (indicated by higher *EQ* values) can be characterized by lower yield potential. Yield potentials with the same *EQ* values show large standard deviation that can be explained by the effect of other site conditions, in particular by soil texture and topsoil layer thickness (*Bidló,* 2014). Connection of yield potential and locally determined drought index may be interpreted also as a series of data predicting yield change over time. Projected increase of *EQ* values by 7.7 units for the end of the 21st century (*Table 3*) would mean a yield potential loss of beech (*Fig. 7*).

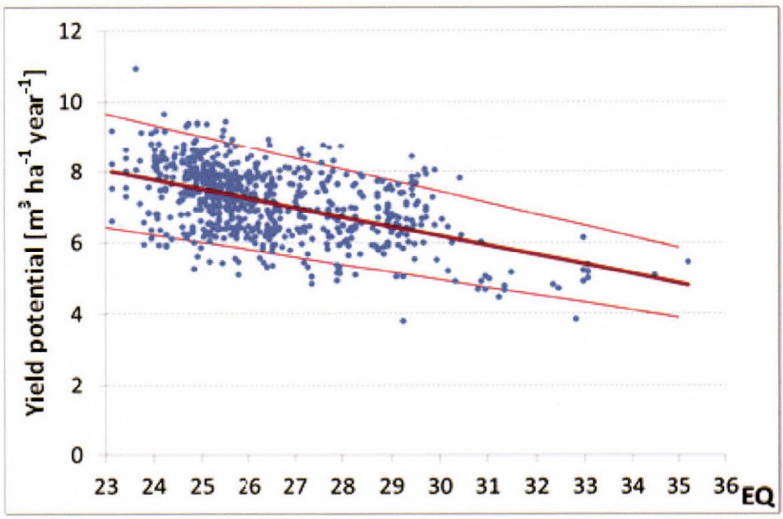

Fig. 7. Yield potential of beech forests in Southwest Hungary calculated as mean annual increment at age 80, in function of long-term values of the Ellenberg's climate quotient (*EQ*). Limiting lines stand for ±20% error (*Veperdi*, 2014).

Table 3. Ellenberg's climate quotient (*EQ*) and its projected change (*dEQ*) for the 30-year time periods in the entire Zala County based on the results of 12 regional climate models. Likely range: 66% of all projections fall within this range

	EQ	***dEQ*** (reference period: 1981–2010)		
Time period	**1981-2010**	**2011–2040**	**2041–2070**	**2071–2100**
Mean over the time period	28.5	+2.1	+3.9	+7.7
Likely range of changes		–1 – +4.9	+0.6 – +5.7	+2.4 – +11.6

- *Climate extremes and their effect on mortality.* Effects of extremes are determining the vitality of forest stands rather than average climate conditions. Projected increase of probability and severity of droughts (*Fig. 6*) overwrites the projections of yield potential functions. Consecutive periods characterized by *EQ* values above a threshold are the basis for modeling present and future tree species distribution as well as tree mortality induced by drought stress (*Móricz et al.,* 2013; *Rasztovits et al.,* 2014).
- *Genetically directed adaptation.* Survival of forest populations is also influenced by genetic factors. Increase of *EQ* indicate the increment decline beech due to suboptimal adaptation (*Horváth* and *Mátyás*, 2014). According to the climate tolerance limit, genetic diversity of oak stands may drastically decline (*Borovics* and *Mátyás,* 2013).

In addition to projections of yield, a number of other important aspects of the climate impact research in forestry will be imported into the decision support system such as:

- *Forest climate zones and production capacity.* Among the site conditions, climate is changing the most dynamically. Therefore for decision support, appropriate determination of climate tendencies and forestry climate categories are essential. Contrary to the climate classification derived from the forest inventory database, a meteorology-based forestry aridity index (*FAI*) has been developed (*Führer*, 2010; *Table 1*) and applied to assess the ecological and economic impacts climate change (*Führer et al.,* 2011, 2013). *FAI* considers not only the distribution and vitality of tree species but also their complex relationships with growth and production.
- *Changes of the forestry climate classes* in Zala County also refer to the more frequent and severe drought periods in the last 30 years (*Fig. 2*). For 1981–2010, most of the climatically suitable areas of beech changed to hornbeam-oak compared to 1961–1990 (*Fig. 8*). In case of the projected

temperature increase and precipitation decrease for May-August (*Fig. 3*), climate conditions are assumed to be favorable for sessile oak – turkey oak rather than for beech in the case study region (*Fig. 8*).

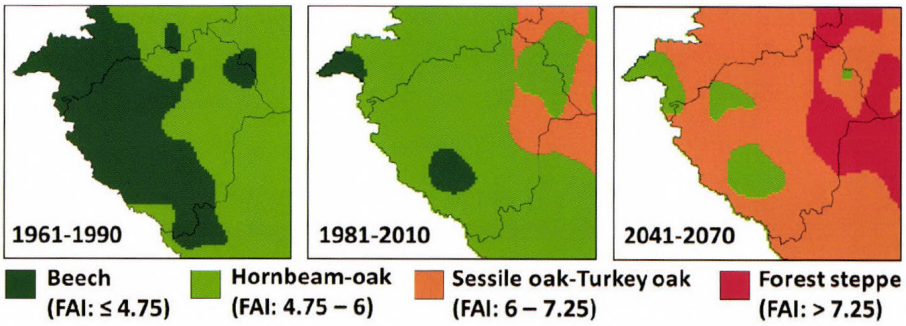

Fig. 8. Climatically suitable areas of different forests derived from the *FAI*-based forestry climate classification (*Führer,* 2010). For 1961–1990 and 1981–2010: observed data, for 2041–2070: observed data + simulated changes based on the mean projection of 12 regional climate models.

- *Water cycle of forested catchments*. Monthly temperature means and precipitation sums are the input of water balance models. The tendency towards a warmer and drier climate (*Fig. 3*) may result in a larger amount of annual evapotranspiration in Zala County, whereas the runoff may decrease to the one third by end of the century (*Csáki et al.,* 2014). Distribution of daily precipitation and its projected changes are used for deriving rainfall interception functions (*Zagyvainé Kiss et al.,* 2014).
- *Soil conditions*. More frequent heavy precipitation days or extreme winds may lead to the decrease of the topsoil layer thickness through higher erosion and deflation risks (*Bidló et al.*, 2014).
- *Potential biotic damages, pests and diseases*. For projecting the frequency of biotic damages as well as the appearance of new insects and diseases, more complex analyses are essential (*Csóka* and *Hirka,* 2011), these cannot be directly derived from the climate input.
- *Wildlife management in forests*. From the projected change of the probability distribution of temperature and from the related reduction of snowfall and snow cover, consequences are drawn for the game damage risks.

4.2. Decision support for end users

Forest management planning needs concrete and quantified information about the possible change of the yield potential, including the economic consequences of premature harvesting due to stability loss on the level of forest sub-compartments, in order to make decisions on species preference. It is a challenge for the decision support system to translate and interpret projected climate change (including the range and likelihood of the simulation results) as well as the standard deviation of the possible impacts as a quantified risk factor, so far.

5. Summary

Long term climate projections have been analyzed that serves as basis of climate impact research and adaptation support in forestry, focusing on the expected probability and magnitude of threatening climate conditions. In the case study region (Zala County in Southwest Hungary), simulation results of an ensemble of regional climate models indicate a significant warming in all seasons towards the end of the 21st century (by up to 3.9 °C for summer in 2071–2100). Both increasing frequency of warm temperature extremes and less cold extremes confirm the warming tendency. Although the mean annual values of precipitation remain almost constant, in winter an increase, whereas in summer a decrease of precipitation can be expected. The latter can exceed 25% until the end of the century in Zala County compared to the climate baseline period 1981–2010. Warmer and drier conditions in summer can result in an increase of the probability and severity of droughts. Heavy precipitation days can be more frequent, especially in autumn and winter. Magnitude of all simulated changes is expected to increase towards the end of the century.

These climate projections have been included as one of the basic datasets in the GIS-based "Agroclimate" decision support system. From the climate input, general climate indices (e.g., hot days, extremely hot days, wet days) and forestry climate indicators (e.g., Ellenberg's climate quotinent; *Ellenberg,* 1988 and forestry aridity index; *Führer,* 2010) are derived. They are used to develop correlation functions for forest growth, yield potential, and production as well as to model many other variables such as species distribution, water and carbon cycle of forests, etc. (see Section 4). Results of climate impact assessments indicate that in case of projected warming and drying of summers, the already observed damages in forestry are very likely to occur with higher probability and severity.

The geoinformatic system allows the integrated data processing and the complex investigation of the climate influenced processes in forest ecosystems. In this way, the GIS-supported climate services can provide a basis of new scientific results in impact research.

However, there is still a gap between provided climate information and required data for impact assessments regarding to the spatial and temporal resolution and the appropriate bias correction methods. Forest responses are also influenced by other factors (e.g., site conditions beyond climate, biotic damages and adaptive capacity) that have been shown to contribute to the relatively large standard deviation of the estimated impacts. The main challenge is to interpret the different bandwidths and uncertainties and to provide a quantified risk factor regarding to possible climate change impacts for end-users in forest management planning.

Climate impact research is being continued in the frame of the "Agroclimate-2" project, where results are planned to be extended to country scale and to the climate-dependent sectors of agriculture by continuous update with recent data and climate projections.

Acknowledgements: Climate data are derived from the regional climate model simulation results of the EU FP6 Integrated Project ENSEMBLES (Contract number 505539; www.ensembles-eu.org). The authors thank to the regional climate modeling group of the Climate Service Center 2.0 Germany for the scientific background. Development of the decision support system is supported by the "Agroclimate" (TÁMOP-4.2.2.A-11/1/KONV) and "Agroclimate-2" (VKSZ_12-1-2013-0034) EU-national joint founded research projects.

References

Antofie, T., Naumann, G., Spinoni, J., and *Vogt, J.,* 2015: Estimating the water needed to end the drought or reduce the drought severity. *Hydrol. Earth Syst. Sc. 19,* 177–193.

Bartholy, J., Pongrácz, R., and *Gelybó, Gy.,* 2007: Regional climate change expected in Hungary for 2071-2100. *Appl.Ecol. Environ. Res. 5,* 1–17.

Bartholy J., Pongrácz R., Gelybó Gy., and *Szabó P.,* 2008: Analysis of expected climate change in the Carpathian basin using the PRUDENCE results. *Időjárás 112,* 249–264.

Berki, I., Rasztovits, E., Móricz, N., and *Mátyás, Cs.,* 2009: Determination of the drought tolerance limit of beech forests and forecasting their future distribution in Hungary. *Cereal Res. Commun. 37,* 613–616.

Berki, I., Rasztovits, E., and *Móricz, N.,* 2014: Erdőállományok egészségi állapotának értékelése – egy új megközelítés. *Erdészettudományi Közlemények 4,*149–155. (in Hungarian)

Bidló, A., Horváth, A., and *Gálos, B.,* 2014: Változó termőhely – változatlan erdők? In (Eds. *Bidló, A., Horváth, A.,* and *Szűcs, P.*) Nyugat-magyarországi Egyetem, Erdőmérnöki Kar, IV. Kari Tudományos Konferencia. NymE Erdőmérnöki Kar Sopron. (in Hungarian)

Bidló, A., 2014: Termőhelyi változás hatása a fatermésre. In: (*Bidló, A., Király, A.,* and *Mátyás Cs.,* (szerk)) Agrárklíma. Nyugat-magyarországi Egyetem Kiadó Sopron. (in Hungarian)

Borovics, A., and *Mátyás, C., 2013:* Decline of genetic diversity of sessile oak at the retracting (xeric) limits. *Ann. Forest Sci. 70,* 835–844.

Csáki, P., Kalicz, P., Brolly, G., Csóka, G., Czimber, K., and *Gribovszki, Z,.* 2014: Hydrological Impacts of Various Land Cover Types in the Context of Climate Change for Zala County. *Acta Silv. Lign. Hung. 10,* 117–131.

Christensen, J.H., Carter, T.R., Rummukainen, M., and *Amanatidis G.,* 2007: Evaluating the performance and utility of regional climate models: the PRUDENCE project. *Clim. Change 81,* 1–6.

Czúcz, B., Gálhidy, L., and *Mátyás, Cs.,* 2011: Present and forecasted xeric climatic limits of beech and sessile oak distribution at low altitudes in Central Europe. *Ann. Forest Sci. 68,* 9–108.

Csóka, G., and *Hirka, A.*, 2011: Alien and invasive forest insects in Hungary (A review). Biotic Risks and Climate Changes in Forest. *Berichte Freiburger Forstliche Forschung 89,* 54–60.

Czimber, K., 2014: Geoadat orientált döntéstámogató rendszer fejlesztése a klímaváltozás hatásainak elemzéséhez. In: ((Szerk.: *Márkus B.* Térinformatika) Székesfehérvár, 309–318. (in Hungarian)

Ellenberg, H., 1988: Vegetation ecology of Central Europe. 4th ed., Cambridge University Press, Cambridge.

Fischer, E.M. and *Schär, C.*, 2010: Consistent geographical patterns of changes in high-impact European heatwaves. *Nature Geosci. 3,* 398–403.

Führer, E., 2010: Tree growth and the climate (in Hungarian). *"Klíma-21" Füzetek, 61,* 98–107.

Führer, E., Horváth, L., Jagodics, A., Machon, A., and *Szabados, I.*, 2011: Application of a new aridity index in Hungarian forestry practice. *Időjárás, 115,* 205–216.

Führer, E., Jagodics, A., Juhász, I., Marosi, Gy., and *Horváth, L.*, 2013: Ecological and economical impacts of climate change on Hungarian forestry practice. *Időjárás 117,* 159–174.

Gálos, B., Lorenz, Ph., and *Jacob D.*, 2007: Will dry events occur more often in Hungary in the future? *Environ. Res. Lett. 2.* 034006.

Gálos, B., Antal, V., Czimber, K., and *Mátyás, Cs.*, 2014: Forest ecosystems, sewage works and droughts – possibilities for climate change adaptation. In (Eds.: *Santamarta J.C., Hernandez-Gutiérrez L.E.*, and *Arraiza M.P.,*) Natural Hazards and Climate Change/Riesgos Naturales y Cambio Climático. Madrid: Colegio de Ingenieros de Montes.

Gribovszki, Z., 2014: Diurnal Method for Evapotranspiration Estimation from Soil Moisture Profile. *Acta Silv. Lign. Hung. 10,* 67–75.

Heinrich, G. and *Gobiet, A.*, 2011: The future of dry and wet spells in Europe: A comprehensive study based on the ENSEMBLES regional climate models. *Int. J. Climatol.* 32, 1951–1970.

Hlásny, T., Mátyás, Cs., Seidl, R., Kulla, L., Mergaicová, K., Trombik, J., Dobor, L., Barcza, Z., and *Konopka, B.*, 2014: Climate change increases the drought risk in Central European forests: What are the options for adaptation? *Lesn. Cas. For. J. 60,* 5–18.

Horváth, A. and *Mátyás, Cs.*, 2014: Növedékcsökkenés előrevetítése egy bükk származási kísérlet alapján. *Erdészettudományi Közlemények 4,* 91–99. (in Hungarian)

IPCC, 2007: Climate change 2007: Synthesis Report. Contribution of Working Groups I, II and III to the Fourth Assessment Report of the Intergovernmental Panel on Climate Change (Pachauri, R.K. and Reisinger, A., eds.), IPCC, Geneva, Switzerland. pp 104. http//:www.ipcc.ch.

Jacob, D., Kotova, L., Lorenz, P., Moseley, Ch., and *Pfeifer, S.*, 2008: Regional climate modeling activities in relation to the CLAVIER project. *Időjárás 112,* 141–153.

Jacob, D., et 38 coauthors EURO–CORDEX, 2013: New high–resolution climate change projections for European impact research. *Reg. Environ. Change 14*, 563–578.

Kjellström, E., Nikulin, G., Hansson, U., Strandberg, G., and *Ullerstig, A.*, 2011: 21st century changes in the European climate: uncertainties derived from an ensemble of regional climate model simulations. *Tellus 63A,* 24–40.

Lakatos, M., Szentimrey, T., Bihari, Z., and *Szalai, S.*, 2013: Creation of a homogenized climate database for the Carpathian region by applying the MASH procedure and the preliminary analysis of the data. *Időjárás 117,* 143–158.

Lakatos, F., and *Molnár, M.*, 2009: Mass mortality of beech on Southwest Hungary. *Acta Silv. Lign. Hung. 5,* 75–82.

van der Linden, P., and *Mitchell, J.F.B.*, eds., 2009: ENSEMBLES: Climate Change and its Impacts: Summary of research and results from the ENSEMBLES project. Met Office Hadley Centre, FitzRoy Road, Exeter EX1 3PB, UK.

Mátyás, Cs., 2009: Ecological perspectives of climate change in Europe's continental, drought-threatened Southeast. In (Eds. *Groisman, P.Y.*, and *Ivanov, S.*) Regional aspects of climate-terrestrial-hydrologic interactions in non-boreal Eastern Europe. NATO Science Series, Springer Verl. 31–42.

Mátyás, Cs., Berki, I., Czúcz, B., Gálos, B., Móricz, N., and *Rasztovits, E.*, 2010: Future of beech in Southeast Europe from the perspective of evolutionary ecology. *Acta Silv. Lign. Hung. 6,* 91–110.

Mátyás, Cs., Gálos, B., Berki, I., Bidló, A., Drüszler, Á., Eredics, A., Illés, G., Móricz, N., Rasztovits, E., and *Czimber, K.*, 2013: A Decision Support System for Climate Change Adaptation in Rainfed Sectors of Agriculture for Central Europe. *Geophys. Res. Abstracts 15,* EGU2013-2942.

Móricz, N., Rasztovits, E., Gálos, B., Berki, I., Eredics, A., and *Loibl, W.,* 2013: Modeling the Potential Distribution of Three Climate Zonal Tree Species for Present and Future Climate in Hungary. *Acta Silv. Lign. Hung. 9,* 85–96.

Pongrácz, R., Bartholy, J., and *Kis, A.,* 2014: Estimation of future precipitation conditions for Hungary with special focus on dry periods. *Időjárás 118,* 305–321.

Prein, A.F., Gobiet, A., and *Truhetz, H.,* 2011: Analysis of uncertainty in large scale climate change projections over Europe. *Meteorol. Z. 20,* 383–395.

Rasztovits, E., Berki, I., Mátyás, Cs., Czimber, K., Pötzelsberger, E., and *Móricz, N.,* 2014: The incorporation of extreme drought events improves models for beech persistence at its distribution limit. *Annals For. Sci. 71,* 201–210.

Spinoni, J., Antofie, T., Barbosa, P., Bihari, Z., Lakatos, M., Szalai, S., Szentimrey, T., and *Vogt, J.,* 2013: An overview of drought events in the Carpathian Region in 1961–2010, *Adv. Sci. Res. 10,* 21–32.

Szentimrey, T., 2011: Manual of homogenization software MASHv3.03. *Hungarian Meteorological Service.*

Szentimrey, T., and *Bihari, Z.,* 2007: Mathematical background of the spatial interpolation methods and the software MISH (Meteorological Interpolation based on Surface Homogenized Data Basis). *Proceedings from the Conference on Spatial Interpolation in Climatology and Meteorology,* Budapest, Hungary, 2004, COST Action 719, COST Office, 17–27.

Szépszó, G., 2008: Regional change of climate extremes in Hungary based on different regional climate models of the PRUDENCE project. *Időjárás 112,* 265–83.

Szinell, Cs., Bussay, A., and *Szentimrey, T.,* 1998: Drought tendencies in Hungary. *Int. J. Climatol. 18,* 1479–1491.

Vautard, R., et 25 coauthors 2013: The simulation of European heat waves from an ensemble of regional climate models within the EURO–CORDEX project. *Clim. Dynam. 41,* 2555–2575.

Vautard, R., Gobiet, A., Sobolowski, S., Kjellström, E., Stegehuis, A., Watkiss, P., Mendlik, T., Landgren, O., Nikulin, G., Teichmann, C., and *Jacob, D.,* 2014: The European climate under a 2 °C global warming. *Environ. Res. Lett. 9,* 034006

Veperdi, G., 2014: Az erdőállományok növekedésmenetének és természeti kockázatainak változásai. In: (Szerk. *Bidló, A., Király, A.,* and *Mátyás Cs.,*) Agrárklíma. Nyugat-magyarországi Egyetem Kiadó Sopron. (in Hungarian)

Zagyvainé Kiss, K.A., Kalicz, P., Csáfordi, P., and *Gribovszki, Z.,* 2014: Forest litter interception model for a sessile oak forest. *Acta Silv. Lign. Hung. 10,* 91–101.

IDŐJÁRÁS

Quarterly Journal of the Hungarian Meteorological Service
Vol. 119, No. 4, October – December, 2015, pp. 443–474

A new hail size forecasting technique by using numerical modeling of hailstorms: A case study in Hungary

Kálmán Csirmaz

Hungarian Meteorological Service Storm Warning Observatory
Vitorlás u. 17. H-8600 Siófok, Hungary
csirmaz.k@met.hu

(Manuscript received in final form March 30, 2015)

Abstract—A new forecasting method for maximum size of hail stones is presented in this paper by using the outputs of a high-resolution, non-hydrostatic numerical weather prediction model (NWP). The method was tested applying simulations of a real case supercell storm producing damaging hail with the Weather, Research and Forecasting (WRF) model. Numerical simulations were made with two distinct horizontal resolutions, 2 km and 100 m, applying nesting technique to assess the effect of the resolution on the storm microphysical properties and the maximum size of the hail stones on the surface. The WRF was able to simulate the main observed characteristics of the supercell on both resolutions. However, the numerical simulation with finer resolution gave better agreement with the radar observation and the observed maximum hail size on the surface. It was found that the horizontal resolution has significant influence on the magnitude and evolution of the microphysical processes in the storm. The numerical simulation with finer resolution produced not only significantly larger maximum mixing ratios of graupel/hail than the 2 km one did, but the volume integrated content of graupel/hail particles in the storm was also larger in the case of finer resolution. This difference can be attributed to the stronger updraft in the case of 100 m resolution. The analysis of various production shows that graupel/hail particles were mainly formed by the heterogeneous freezing of supercooled rain drops and by the freezing of rain drops due to the collision with cloud ice in the midlevels (between 3 and 8 km). Subsequent accretion of graupel/hail particles occurred by the collision with cloud and rain water. Larger graupel/hail content aloft in the case of finer simulation resulted in larger surface mixing ratios which directly led to larger maximum hail sizes on the ground.

Key-words: supercell, hail, WRF

1. Introduction

Hail is a threatening atmospheric phenomenon and storms with hail on the ground (hereafter hailstorms) frequently cause large fraction of weather-related damages. The annual crop losses often reach several hundreds of million dollars (*Changnon et al.,* 2000) in the USA. Hungary is an exposed region, as well: in the 70s, the hail-related annual insurance charges in Baranya county – before the installation of the hail suppression system – totaled to 100–200 million forints. Therefore, prediction of hail on the ground – especially its existence and a characteristic diameter of hailstones –, is a crucial segment of mesoscale forecasts and warning systems. The difficulties of forecasting hail come from the large spatial and temporal variability of hailfalls and relatively low frequency of their occurrence over a certain point of the ground. This makes the verification and validation of any forecasting techniques quite complicated.

The first methods were based on statistical relationships between the observed state of the atmosphere and the existence and size of the hail on the ground (e.g., *Fawbush* and *Miller*, 1953; *Miller*, 1972). From the sixties-seventies, as the capacity of computers had gradually improved, it became possible to explicitly simulate the hail formation and growth in thunderstorms producing hail on the ground. The initial attempts were one-dimensional steady-state "jet" models (e.g., *Simpson* and *Wiggert*, 1969; *Weinstein*, 1972; *Zoltán* and *Geresdi*, 1984) and one-dimensional, time-dependent models (*Ogura* and *Takashi*, 1971; *Wisner et al.*, 1972; *Ćurić* and *Janc*, 1989 and 1993). Since that time, the statistical methods for forecasting hail have been coupled with one-dimensional cloud models to evaluate the maximum updraft speed (e.g., *Renick* and *Maxwell*, 1977; *Moore* and *Pino*, 1990) or complex microphysics schemes have been combined with simple steady-state cumulus models (e.g., *Brimelow et al.*, 2002, *Brimelow* and *Reuter*, 2006; *Geresdi et al.*, 2004 etc.). The development of two- or three-dimensional, time-dependent cloud models enabled the more reliable simulations and complex analyses of the microphysical processes and their relationships to the airflow in and around multi- and supercell storms (*Orville* and *Kopp*, 1977; *Takahashi*, 1976; *Johnson et al.*, 1993 and 1995; *Geresdi*, 1990 and 1996). However, these models involve bulk microphysics schemes, therefore, they are not able to explicitly compute the evolution of hydrometeor sizes, but only the parameters of their preset size distributions. Though detailed spectral (bin) microphysical models work with size categories, they are computationally more expensive (*Farley* and *Orville,* 1986; *Farley,* 1987 a,b; *Geresdi*, 1998), which inhibits their wide-spread application in multidimensional microphysical numerical experiments and operational application.

Due to the appearance of the new generation of mesoscale, non-hydrostatic models, such as the Weather Research and Forecasting Model (WRF – *Skamarock et al.*, 2008), three-dimensional, real-data simulations of hailstorms became routinely executable in an operational manner via their complex bulk

microphysical schemes. Moreover, using this type of numerical models, explicit prediction of hail or other hydrometeor categories on the ground is also possible. Still, to date, there is barely known any hail forecasting methods based upon the explicit microphysical outputs of mesoscale numerical weather prediction models (NWP). Though *Milbrandt* and *Yau* (2006) developed a method to estimate the maximum size of hailstones at the surface based on the three-moment size distribution of the hail category predicted by NWP, they did not suggest that method as a possible way for operationally forecasting the existence and size of hail stones. In this paper, the description and results of recently developed method about the forecast of the maximum hail size is presented.

The effect of resolution on the morphology of thunderstorms has been thoroughly studied (e.g., *Grabowski et al.*, 1998; *Adlerman* and *Droegemeier,* 2002; *Petch et al.*, 2002). It was found that the properties of the simulated mesoscale phenomena were very sensitive to the applied horizontal resolution of the model. In relation with this issue, numerous experiments were made to determine the "ideal" resolution to a physically consistent cloud-resolving model regime. *Bryan et al.* (2003), for example, found that a horizontal resolution of about 100 m is necessary for a correct simulation of an idealized squall line case. *Craig* and *Dörnback* (2008) proposed that the horizontal resolution of a consistent mesoscale simulation should be determined by either of horizontal scale of a buoyant bubble or the buoyancy height which requires tens of meters of resolution. *Friori et al.* (2010) examined the effects of resolution and various turbulence schemes on the morphology of a supercell by numerical simulation of idealized cases, and they found the values of storm-scale properties to converge at horizontal resolution of 200 m. To summarize, simulation with horizontal resolution on the order of hundreds of meters is necessary in order to obtain physically as consistent results as possible regarding the microphysical properties of a hailstorm.

Supercells, as effective hail-producing storms, occurs over Hungary every year mainly during the warm season (*Horváth* and *Geresdi*, 2003), and there were successful attempts to simulate them with state-of-the-art NWP's (*Horváth* and *Geresdi*, 2003; *Horváth et. al.*, 2009; *Putsay et al.*, 2011). However, these studies did not cover the microphysical aspects of the simulations. Therefore, in this paper, a detailed analysis of microphysical processes focusing on the formation and growth of solid hydrometeors (graupel/hail) is given. The analysis was performed, on one hand, on a coarser model grid with O (1 km) grid spacing corresponding to the present-day, operationally applied resolution in NWP forecasts and, on the other hand, on a high-resolution domain with O (100 m) grid distance which yields physically the most consistent cloud-resolving simulation. The comparison of the storm's microphysical properties on the two distinct grids is also carried out to study the effect of the resolution on the hydrometeor fields in the storm. In Section 2, the methodology of the research and the method for assessing hail-size on the ground are shown. In

Section 3, we describe the details of a case study, and the results of the numerical simulations and hail-size calculations are presented. Summary and plans for future work are given in Section 4.

2. *Methodology*

2.1. Description of the modeling environment

The simulations were carried out with the WRF-ARW non-hydrostatic mesoscale numerical model version 3.1.1 (*Skamarock et al.*, 2008) using nested domains with different horizontal resolutions. The largest domain (Domain 1) has a resolution of 6 km and it covers an area of 700 km × 850 km in the Carpathian Basin. The second, smaller domain (Nest 1) includes Hungary, too, but it has 2 km resolution and covers a region of 450 km × 360 km. The smallest domain (Nest 2) is embedded in Nest 1. This domain is used to focus on the particular storm, therefore its horizontal resolution is 100 m and covers only an area of 44 km × 30 km. This resolution was chosen according to the results published by *Bryan et al.* (2003). They found that – in the case of idealized boundary conditions – the simulated properties of a squall line showed convergence if the horizontal resolution was equal to or less than 100 m. This means that the further decrease of horizontal grid distances hardly affects the output of the numerical model. It is supposed that the above-mentioned conclusion of *Bryan et al.* (2003) is valid for the supercell case presented in this paper, too. The vertical resolution was the same in each nest: 37 terrain-following levels were applied with larger vertical resolution near to the surface and with stretched resolution at higher altitudes. The lowest model level was about ten meters above the ground and the top of the domain was at 50 hPa. All in all, we performed one model run on three domains (Domain 1, Nest 1 and Nest 2) connected via one-way nesting technique, but only the results on Nest 1 and Nest 2 were evaluated. We consider the model run on Nest 1 and Nest 2 as distinct simulations, therefore, hereafter we are referring to these simulations as Simulation1 (Nest 1) and Simulation2 (Nest 2). See *Fig. 1* for the location of domains of the simulations.

The formation and evolution of different types of hydrometeor species was simulated by the Thompson's one-moment bulk microphysical scheme (*Thompson et al.*, 2004) adapted from the Reisner scheme (*Reisner et al.*, 1998). The Thompson's parametrization is a state-of-the-art Simulation of the microphysical processes, especially in the case of mixed phase clouds. This scheme allows us to study the characteristics of different types of ice particles in severe thunderstorms. The scheme involves prognostic equations of mixing ratios for five different species: cloud water, cloud ice (cloud particles), snow, rain, and graupel/hail (precipitation particles). The parametrization does not include hail as a distinct category but larger graupel particles computed implicitly by the model can be

treated as hailstones[1]. Grell's cumulus parameterization scheme (*Grell* and *Dévényi*, 2002) is used to simulate the formation of convective clouds. In the cases of larger resolution (i.e., Simulation1 and Simulation2), this parameterization scheme was switched off and the model was let to develop the convection directly. Independently of the horizontal resolution, the Mellor-Yamada-Janjic's (MYJ – *Mellor* and *Yamada*, 1982) planetary boundary layer (PBL) parametrization scheme is activated coupled horizontally with Smagorinsky's first order closure treatment for the sub-grid diffusion. A proper selection from the schemes describing the turbulence is crucial. The main problem about the choosing of the appropriate scheme is that different resolutions need different treatments of the turbulence. As the horizontal resolution is increased from 2 km to 100 m, the averaged momentum equations of the model begin to resolve the boundary layer eddies (large eddy simulation – hereafter LES). This range of resolution is named "terra incongnita" by *Wyngaard* (2004). Eddies in this size interval possess the main fraction of the turbulent energy spectrum regarding cumulus convection. Nevertheless, a Simulation in "terra incongnita" is not able to adequately resolve the energy-containing eddies based on subgrid diffusion closure with a scalar diffusivity. Instead, *Wyngaard* (2004) suggested that a tenzor of three-dimension scalar diffusivity coefficients should be applied in such Simulations. In addition, for a nested, real data case simulated by WRF, *Talbot et al.* (2012) showed that applying LES in "terra incognita" yielded mixed results in the model performance. In addition, they found that the results on the nest with ultra-fine resolution (on the order of 100 m's) were even more sensitive to the lateral boundary conditions and to the initial forcing (represented by the analysis) than to the chosen turbulence closure. These are the reason why the same schemes – the MYL-scheme for handling the vertical diffusion and the Smagorinsky first order scheme for parameterization of the horizontal eddy diffusivity coefficients – were used both in the case of Simulation1 and Simulation2.

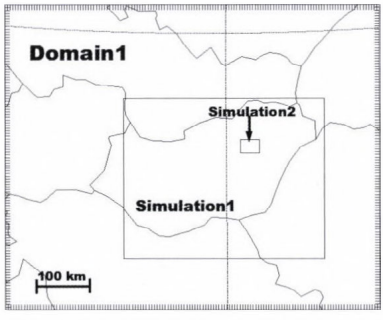

Fig. 1. Location of Domain1 and the nests of Simulation1 and Simulation2 in the WRF model run.

1 In this case, implicit means that the scheme only returns with the mixing ratio of graupel/hail in a grid box. However, upon this quantity and the size distribution, hypothetical and possible particle sizes with their concentration can be assessed.

Initial and lateral boundary conditions for Domain 1, Nest 1, and Nest 2 were provided by the ECMWF global model, by the outputs of Domain 1, and by the outputs of Nest 1, respectively. (The WRF model outputs were generated in every 5 minutes in the case of Simulation1, and in every 1 minute both in Simulation2 and Simulation1 during the time interval when the storm was in the volume defined by Nest 1. Analyses and hail-size calculations were performed on the model's terrain-following eta-system. For the plotting of vertical cross sections, the data were transformed into a Cartesian system with height above the mean sea level as a vertical coordinate.

2.2. Description of the data collected for validation

The results of the numerical model and that of the recently developed hail size forecasting method are intended to compare with observation data. The reliability of the forecast of maximum hail size depends both on the quality of the model output and on the accuracy of the method used on the calculation of the maximum hail size from the model output. Therefore, for the validation of the forecast of maximum hail stone size, such a case was chosen where the model was able to simulate the characteristics of a severe storm correctly, and surface observation data about the size of the hail stones were available. Database of well-documented cases of severe hailstorms was searched to find the appropriate case. This means that, besides the data of hail existence, data on the hailstone sizes should be also available. In the eighties a hail pad network operated in the southern parts of Hungary associated with the hail suppression activity. Unfortunately, this type of hail size measurements was ceased in the early 90's. Since then, there have been no directly observed, quantitative data about the hailstone sizes on the surface, but only qualitative and indirectly observed data about the characteristics of the hailstones are available. The source of data is the followings: 1) Online sources of falling hailstones on various commercial and amateur meteorological sites where extensive documentation of significant severe weather events can be found. These documentations were done mostly by voluntary people who uploaded their photos and videos of hailstones to these sites. These sources, though to a limited extent, can be used for verification. 2) Radar observation data which are not suitable for direct evaluation of hailstone sizes at the ground due to the uncertain relation between the observed reflectivity and hail stone size. However, high reflectivity itself can indicate the existence of hail or perhaps severe hail. Therefore, comparison between the measured and simulated reflectivity is also performed in order to evaluate the model's ability to reproduce the microphysical characteristics of real storms. The simulated radar intensity was calculated by the NCAR Command Language (NCL) post-processing module of WRF-ARW.

2.3. *Description of the hail-size calculation method*

Forecasting of maximum hail-size is based on the followings: the model computes the graupel/hail mixing ratios on the three-dimensional model grid at every time step. These calculations are carried out by taking the size following gamma size distribution of graupel/hail particles (*Fig. 2*) defined by the scheme (see *Thompson et al.*, 2004) at the lowest model level (η=0.997):

$$N(D) = N_0 D e^{-\lambda D}, \tag{1}$$

where D is the diameter of graupel/hail particles (they are supposed to be spherical objects)

$$N_0 = 2.38\left[\frac{\pi\rho_g}{q\rho_a}\right]^{0.92}, \tag{2}$$

where is ρ_g the density of a graupel/hail particle (400 kgm^{-3}) and ρ_a is the density of air.

The λ parameter can be obtained from the mixing ratio via the following relationship:

$$q = \frac{1}{\rho_a}\int_0^{\infty} N_0 \frac{D^3\pi}{6} \rho_g D e^{-\lambda D} dD \tag{3}$$

After calculating the integral on the right hand side of Eq. (3), the λ parameter can be given in an explicit form:

$$\lambda = \left[\frac{4N_0\pi\rho_g}{q\rho_a}\right]^{0.2}. \tag{4}$$

The number concentration of graupel/hail particles can be computed via the following equation:

$$n = \int_0^{\infty} N_0 D e^{-\lambda D} dD = \frac{N_0}{\lambda^2}. \tag{5}$$

A definite integral of Eq. (5) between X and ∞ gives the number concentration of particles larger than X. The algorithm of hail size forecast is based on the following equation:

$$n_X = \int_X^{\infty} N_0 D e^{-\lambda D} dD = N_0 \frac{e^{-\lambda X}}{\lambda^2}(\lambda X + 1), \tag{6}$$

where n_x is a predefined threshold number concentration of graupel/hail particles. The Newton-Raphson iteration technique was used to calculate the value of the variable X, the diameter of graupel/hail particles which concentration is equal to n_x. The value of this threshold number concentration was chosen to be equal to 10^{-4} m^{-3} (*Milbrandt* and *Yau*, 2006). This value means that there is exactly one hail stone in a volume of column with height of 1 m and with cross section of 100 m × 100 m^2. The hail stones of lower concentration than the threshold are very difficult to detect. Therefore, X can be defined as maximum observable (possible) hail size.

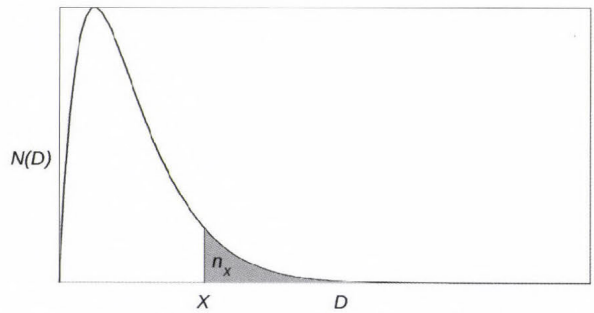

Fig. 2. The gamma distribution of graupel/hail particles used in the Thompson's scheme. D on the abscissa represents the graupel diameter, $N(D)*dD$ along the y-axis is the number concentration of graupel in the infinitesimal D, $D+dD$ interval. X denotes the diameter above which the concentration is equal to n_x. See text for further description.

3. Results

3.1. *Case study: synoptic features and observation data*

On June 7, 2009, an isolated supercell passed through the northeastern part of Hungary, produced large hail (the maximum hail stone diameter was reported to be about the size of a tennis ball) causing severe hail-related damages in several locations. The synoptic feature of this event was characterized by a quasi-stationary waving cold front at northwest of Hungary (*Fig. 3a*). East of the front, over Hungary, warm and moist air advected from the south at low-levels. At upper-levels, at the western part of Hungary, the front is accompanied by a trough (not shown) moving slowly eastward. Downstream of the trough, high

wind speeds prevailed aloft (~30 m/s at 500 hPa). These conditions resulted in considerable instability and significant vertical wind shear: ~1000 J/kg convective available potential energy values and 25–30 m/s as magnitudes of vector differences between winds at the surface and 6 km (*Fig. 3b*). These parameters are good indicators regarding the large chance of developing supercells (*Thompson et al.*, 2003).

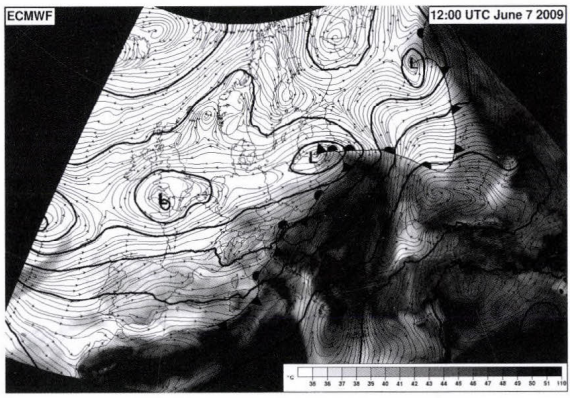

Fig. 3a. The synoptic situation of the waving front over Central Europe at 12:00 UTC, on June 7, 2009 according to the ECWMF analysis. Shading represents the equivalent potential temperature field (in Celsius) at 850 hPa, black solid lines denote the geopotential height of the 850 hPa pressure level (contoured with 40 m intervals), streamlines denote the wind at 850 hPa. Letter L denotes low heights (low pressures).

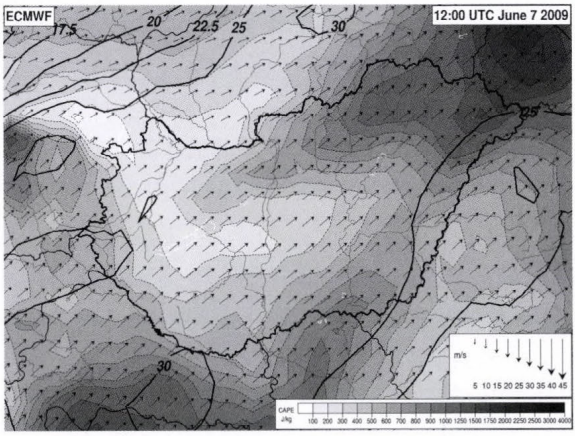

Fig. 3b. Convective available potential energy (shaded), 0–6 km vertical wind shear (magnitude of the vector difference, m/s, solid black lines), and 0–6 km mean wind (black arrows) at 12:00 UTC, on June 7, 2009 above Hungary according to the ECWMF 12:00 UTC analysis.

According to composite radar images generated in every 15th minute, the supercell developed at 12:30 UTC over the central part of Hungary, then rapidly propagated (with an average speed of 75 km/h) northeastward, passed north of Nyíregyháza, left the country at 14:30 UTC, and dissipated at 16:30 UTC in Ukraine. Thus, its lifetime reached three and a half hours. The reflectivity inside the hail storm reached its maximum value of 67.5 dBz at 13:45 UTC (*Fig. 4*). Based on news reports, the cell caused the most hail-related damages along the line of Tiszavasvári-Nyírszőlős-Kemecse-Nyírbogdány-Demecser-Berkesz villages (see their location in *Fig. 4*). Voluntary observers reported maximum hailstone size of around 4 cm (*Fig. 5*).

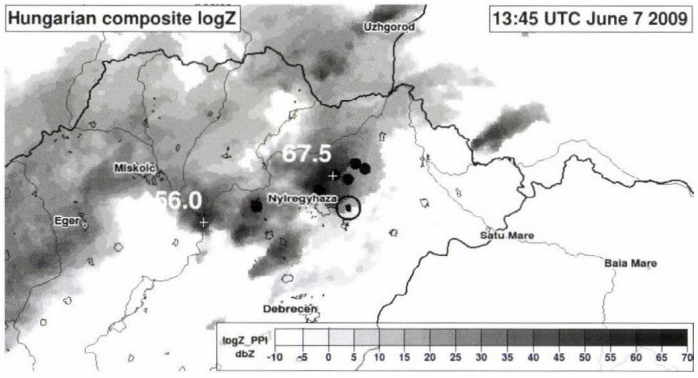

Fig. 4. Observed radar picture of the simulated thunderstorm at 13:45 UTC, on June 7, 2009. Shading represents the intensity in dBz, which is the column maximum reflectivity. Maximum values are indicated by white numbers. Villages exposed to large, damaging hail are denoted by dots. The location of the closest radar site (Napkor) is depicted by a black circle. The direction of propagation of the storm is denoted by a black arrow.

Fig. 5. Observed typical hail sizes in the villages (see text) crossed by the supercell on June 7, 2009. (Source: idokep.hu)

Analysis of reflectivity and radial velocity data proved that the hailstorm was a supercell with considerable rotational features. The storm moved along slightly north to the location of the radar at Napkor, east of Nyíregyháza (as seen in *Fig. 4*). According to the results of the analysis of Doppler radar data (*Fig. 6*), the storm did not showed features of low-level rotation in its development phase (from its formation at around 12:30 UTC to 14:30 UTC). However, considerable midlevel vortex (not shown) and, as a sign of highly sheared environment, a significant weak-echo region (WER) with high-reflectivity regions aloft on its downshear (to the east) side (not shown) were detected. After the storm passed Napkor, between 13:45 and 14:00 UTC, a well-visible hook echo feature developed on its southern side accompanied by a bounded weak echo region (BWER), and a vault extended on its downshear flank. At the same time, a low-level vortex (depicted by a rectangle in *Fig. 6*) formed around the hook echo region. According to *Lemon* and *Doswell* (1979), these features suggest that the hailstorm – during the long period of its lifetime – behaved as a supercell storm.

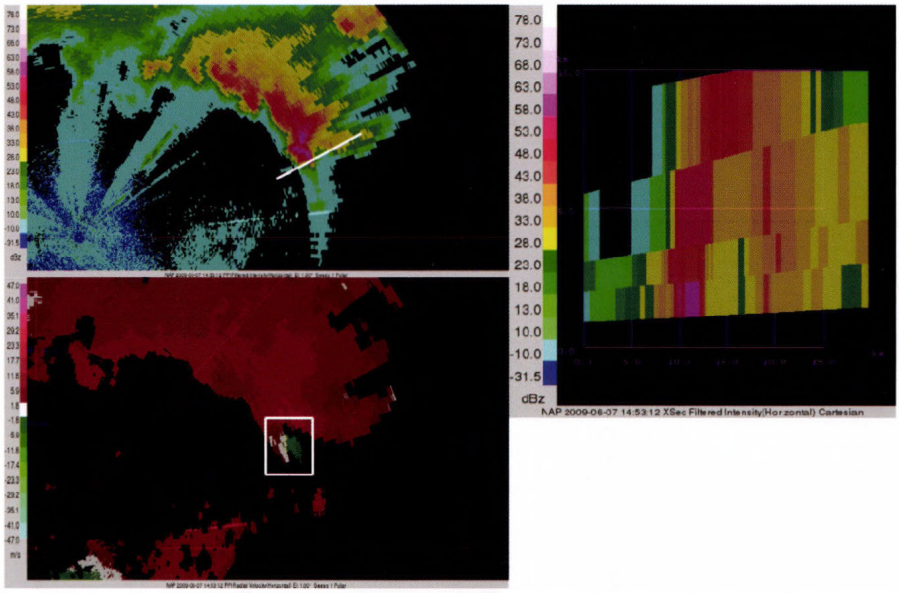

Fig. 6. PPI reflectivity (upper left), storm-relative radial velocity (lower left) at an elevation angle of 1 degree and vertical cross section of reflectivity (right) through the storm observed by the Napkor radar at 14:53 UTC, on June 7, 2009. Circles in the pictures on the left depict distances of 30 km, 48 km, and 115 km from the radar. The white line in the PPI denotes the orientation of the cross-section on the right. In the radial wind picture, red colors indicate approach, greenish colors mean drawing-away. The rectangle on the left lower picture encloses the area of significant radial shear, i. e., the location of a mesocyclone which has an altitude of around 1 km.

3.2. Results of numerical Simulation

The Simulations of WRF were initialized at 06:00 UTC, June 7, 2009 from the 00:00 UTC, June 7, 2009 ECMWF run, and was run until 18:00 UTC, June 7, 2009. The finest, 100 m grid (Simulation2) extended to a 44 km × 30 km area (440 × 300 horizontal grid points) was located in the path of storm formed in Simulation1.

3.2.1. Verification

The simulated reflectivity data on both grids at a given time are shown in *Fig. 7*. The reflectivity structure of the simulated thunderstorm is similar to that of the observed one (*Fig. 4*): an isolated high-reflectivity core with a significant gradient at the southern part of the cell and a much smoother gradient downstream with an accompanying larger scale weak-reflectivity pattern can be observed both in *Fig. 4.* and *Fig. 7.* These features indicate the presence of a supercell with rotating mesocyclone in a highly sheared environment.

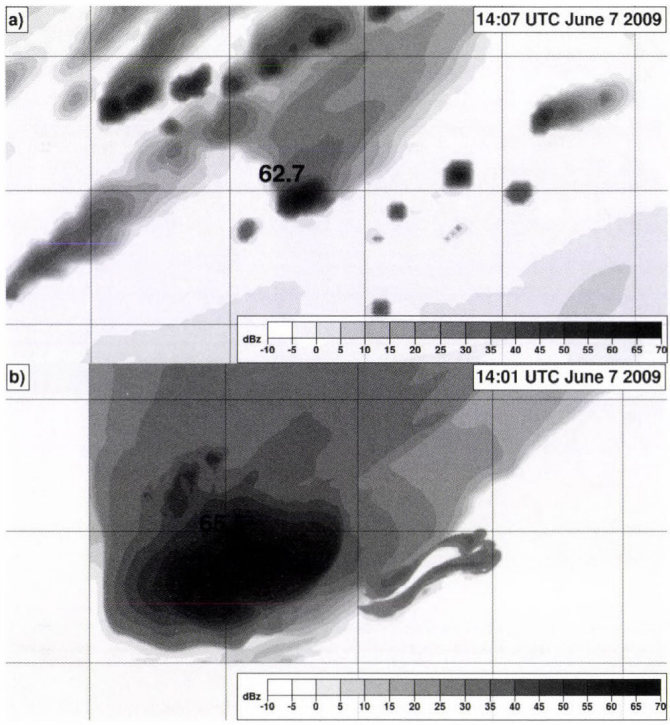

Fig. 7. Calculated column-maximum reflectivity in dBz a) in Simulation1 at 14:07 UTC and b) in Simulation2 at 14:01 UTC, June 7, 2009. The numbers denote the maximum values. The square boxes represent 25 km × 25 km and 10 km × 10 km areas in a) and in b), respectively.

Time evolution of both simulated and observed maximum values of reflectivity can be seen in *Fig. 8a*, which shows that Simulation1 underestimated the intensity of the cell throughout its lifetime. In the case of Simulation2, the cell entered Nest 2 has a maximum reflectivity of 62 dBz, and five minutes later it reached 66 dBz. These values are much closer to the observed ones than the simulated reflectivity values in the case of Simulation1. Note, that data for this high reflectivity core are only available between 13:45 and 14:30 UTC in Simulation2, because Nest 2 was rather small (only 44 km × 30 km), and the fast-moving cell (at a speed of about 55 km/h) quickly passed it.

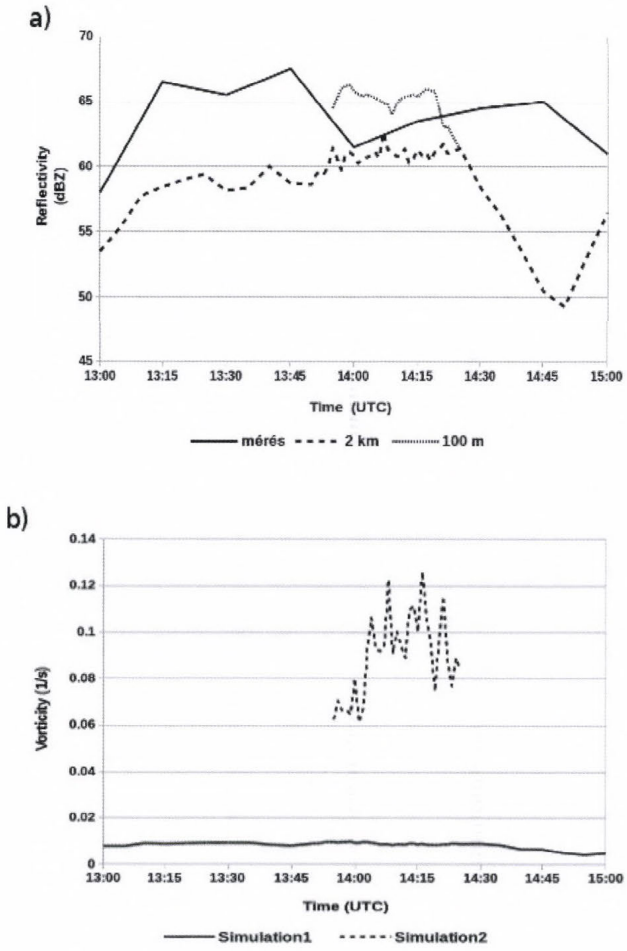

Fig. 8. Time evolution of a) the observed and simulated maximum reflectivities and b) the maximum relative vertical vorticity in the supercell in the case of Simulation1 and Simulation2 on June 7, 2009.

In order to assess the model's capability of simulating the dynamics and related structures of the supercell, spatial and temporal evolution of the vertical vorticity field were also investigated. *Fig. 8b* shows the time evolution of maximum midlevel (between 3 and 7 km) vertical vorticities. In the case of Simulation1, the maximum vertical vorticity remains near to 0.01 1/s (or slightly below). On the other hand, the supercell in Simulation2 developed a much more intense vortex with values larger than 0.06 1/s (for a short time even larger than 0.1 1/s). Horizontal cross-sections of vertical vorticity field around the simulated cell at a certain time step, together with other ultimate parameters, are plotted in *Fig. 9*. The cross sections are given at the height of 5 km, thus they characterize the midlevel structure of the storm. In the case of Simulation1 (*Fig. 9a*), an area of a strong updraft with vertical velocities between 20 and 30 m/s is coupled with moderately strong positive vertical vorticity in such a way, that the maximum of vertical vorticity lies on the right flank of maximum updraft velocities. This configuration corresponds well with both the observational (*Lemon* and *Doswell*, 1979) and simulated (*Klemp*, 1987) structures of supercells. The intensity of vertical vorticity hardly reaches the value of 0.01 1/s, which is a threshold for the formation of a mesocyclone (*Doswell*, 1996). The accompanying storm-relative streamlines show no pure vortices (the streamlines are curved but not enclosed). However, the areas of downdraft (indicated by the rainwater at the surface) and the updraft are horizontally well separated, which is a necessary condition for long-lived thunderstorms (*Browning*, 1968). Similar structure developed in the case of Simulation2 (*Fig. 9b*). The features are more obvious than in the case of Simulation1. The vertical vorticity is more intense (with maximum value of 0.05 1/s); the closing streamlines depict a true cyclonic vortex to the right of the updraft and a pure anticyclonic vortex deep in the precipitation zone; and the surface rain mixing ratio is much higher (above 10 g/kg), as well. It can be concluded that both Simulations were able to catch the essential structure of supercell, but the Simulation with finer resolution generated a cell with much more expressed features.

3.2.2. Comparison and evaluation of microphysical properties and production terms of graupel/hail of Simulation1 and Simulation2

The time evolution of maximum in-storm values of mixing ratios of all hydrometeor categories (cloud water, cloud ice, rain, snow, and graupel/hail) in Simulation1 and Simulation2 are plotted in *Figs. 10a* and *b*. The spatial resolution seems to have a significant effect on the amount of the precipitation particles. The simulation with finer resolution produced larger maximum mixing ratios of graupel/hail particles and that of rain water (*Fig. 10a*). The mean maximum mixing ratios of these precipitation species are 3–4 g/kg and 5–7 g/kg higher in the case of Simulation2 than in the case of Simulation1. No significant differences were found in the case of maximum mixing ratio of the snow. If we

assess the differences in cloud particle mass (cloud water and ice) and relative humidity maximum between the two resolutions (*Fig. 10b*), then the following conclusions can be drawn: while Simulation1 and Simulation2 give similar maximum cloud water mixing ratios (~2–4 g/kg), the maximum value of cloud ice mixing ratio is significantly larger in the case of Simulation1, than in Simulation2 (~0.4–0.6 g/kg versus ~0.2 g/kg). The obtained in-cloud (above 3km) maximum water vapor mixing ratio was about 6–7 g/kg on both grids with a bit higher value on the 100 m resolution grid.

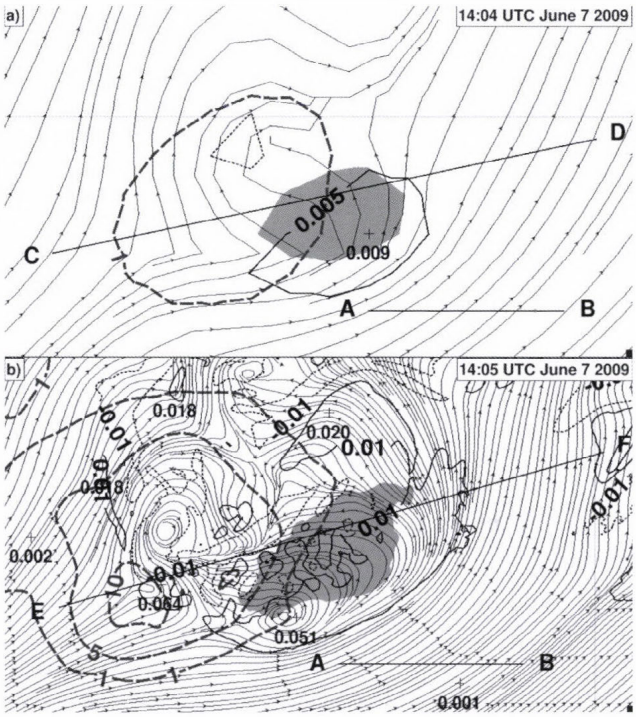

Fig. 9. Simulated horizontal, storm-relative streamlines; relative vertical vorticity (light solid contour of positive values; light dashed contours of negative values); vertical velocity (grey shaded area above the value of 20 m/s) at z=5 km, and rainwater mixing ratio (dark grey bold dashed contours of 1, 5, and 10 g/kg) at z=50 m.
a) in Simulation1 at 14:04 UTC on, June 7, 2009. As for vertical vorticity, only the 0.005 1/s and –0.005 1/s isolines are shown. The length of AB line is 10 km. The CD line represents the horizontal orientation of the vertical cross section in *Figs. 13a* and *b*, and *Figs. 14a* and *b*.
b) in Simulation2 at 1405 UTC on, June 7, 2009. As for vertical vorticity, only the 0.01 1/s and –0.01 1/s isolines are shown. The length of AB line is 2,5 km. The EF line represents the horizontal orientation of the vertical cross section in *Figs. 13c* and *d*, and *Figs. 14c* and *d*.
In both pictures, the local maximum values of vertical vorticity (1/s) are indicated by numbers.

The microphysical processes regarding the formation of graupel/hail in the cloud were analyzed by plotting the time evolution of the production terms of graupel/hail mass. The following production terms are included in the Tompson's scheme (without the melting): deposition/sublimation of water vapor onto/from the graupel/hail surface (gde), conversion of snow into graupel/hail due to riming (sgc), freezing of supercooled rainwater (frz), collision of rainwater and snow (rcs), collection/accretion of graupel/hail by cloud water (gcw), collision of rainwater and graupel/hail (rcg), freezing of rainwater by its collision with cloud ice (rci), and graupel/hail production due to ice multiplication during riming process (ihm) (*Hallet* and *Mossop*, 1974). These production terms were averaged around the location of the maximum mixing ratio of graupel/hail in a volume, which involves 3×3 (in Simulation1) and 60×60 (in Simulation2) grid points horizontally (each represents a 6 km × 6 km square) and 3 grid points vertically (in both simulations). Note, that results of Simulation2 are plotted only between 13:55 and 14:25 UTC because this was the time period when the cell stayed inside of Nest 2.

Time evolution of the production terms in *Figs. 10c* and *d* show that the larger amount of graupel/hail in the case of Simulation2 is the consequence of the considerably larger freezing rate of rainwater (the difference between Simulation2 and Simulation1 is about an order of one magnitude). Subsequently, the amount of graupel/hail further increased due to the more efficient accretion by supercooled cloud water drops (this latter production term is two times larger in Simulation2 than in Simulation1). The riming of cloud ice by cloud water acts as a strong sink of cloud ice (much more efficient than cloud ice-rain collision). Because the formation of snow is more efficient due this process in Simulation2 than in Simulation1 (not shown), more cloud ice particles remain in the latter case. As a consequence, the graupel/hail production due to rain-ice collision is significantly larger in Simulation1 than in Simulation2. The height of maximum graupel/hail mixing ratio is larger in Simulation2 than in Simulation2 during the first half of the 13:55–14:25 UTC time period (slightly below 7 km in Simulation1 and between 7–8 km in Simulation2). After this time period, it rapidly decreases below 5 km in Simulation2 (in Simulation1 the decrease is gradual).The larger height of maximum in Simulation2 can be attributed to the larger vertical velocities (see next paragraph), which can transport the graupel/hail mass to higher altitudes.

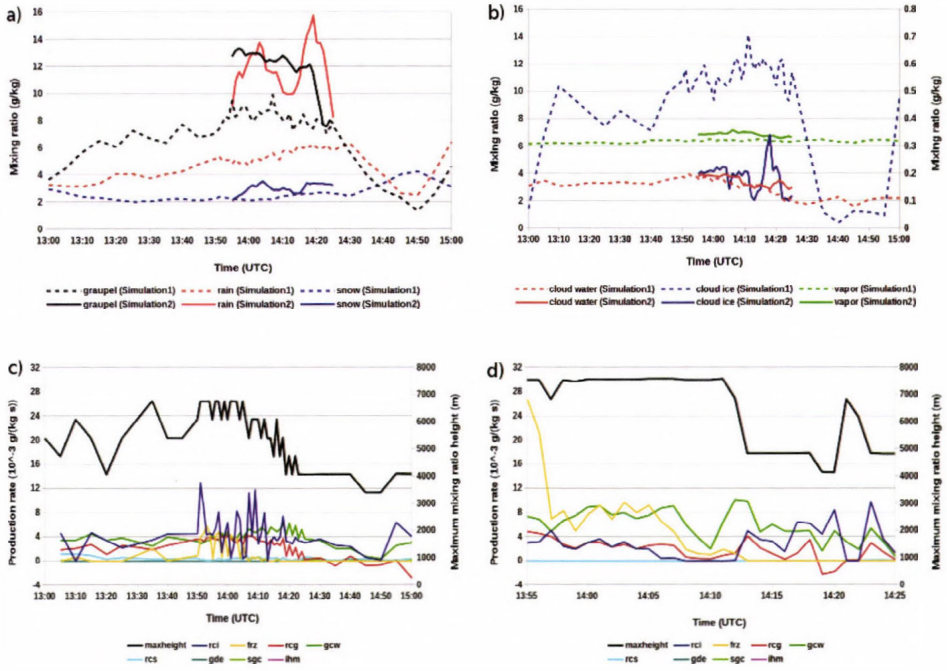

Fig. 10. Time evolution of maximum in-storm values of a) precipitation particles (graupel, rain, and snow in g/kg), b) cloud particle mixing ratios (g/kg) of both nests. c) and d) shows the tendency of graupel production terms (in mg/kg s) averaged around the maximum graupel mixing ratio (see text) in Simulation1 and Simulation2, respectively. For the description of abbreviations in the legend of c) and d) see text. Curve maxheight represents the height (above ground level) of the maximum graupel mixing ratio.

Maximum of updraft and downdraft velocities in the vicinity of the maximum mixing ratio of graupel/hail and the time evolution of maximum graupel/hail mixing ratio on the surface are plotted in *Fig. 11*. In the case of the updraft, vicinity means that the maximum values are chosen from a volume contains $3 \times 3 \times 5$ and $11 \times 11 \times 5$ grid points around the location of the graupel/hail maximum in Simulation1 and Simulation2, respectively. The maximum value of downdraft was taken from a volume contains the location of maximum graupel/hail mixing ratio on the surface. The bottom of this volume is on the surface, its horizontal extension is the same as it was mentioned above. The depth of the volume is 6 km. The maximum vertical velocity was larger in the case of Simulation2 (peaked at around 35 m/s) than in Simulation1 (below 30 m/s, around 25 m/s) almost all the time during the simulation. This difference could explain why maximum graupel/hail mixing ratios aloft is greater in Simulation2. The stronger updraft could hold up larger amount of graupel/hail

aloft, and the larger vertical velocity might resulted in larger upward vapor flux, which subsequently could promote the enhanced production of rainwater and graupel/hail. Furthermore, due to larger condensation rate, more latent heat is released which could further intensify the updraft. The strong relation between the updraft intensity and the maximum mixing ratios of precipitation particles aloft is clearly visible by comparing the plots in *Fig. 11* and *Fig. 10a*. These figures show that the time evolution of the maximum of mixing ratios (both rain and graupel/hail) and maximum of updraft velocities run parallel. On the surface, the maximum of graupel/hail mixing ratio is considerably larger in Simulation2 than in Simulation1. Sometimes this difference is as large as one order of magnitude (~2–3 g/kg in Simulation2 and 0.3–0.6 g/kg in Simulation1). This is the consequence of the larger maximum mixing ratio of graupel/hail aloft in Simulation2. The larger amount of graupel/hail aloft generates stronger downdraft by loading, evaporative cooling, and melting effects. This is the reason why stronger downdraft developed in the case of Simulation2 than in the case of Simulation1 (~10–15 m/s versus ~5 m/s).

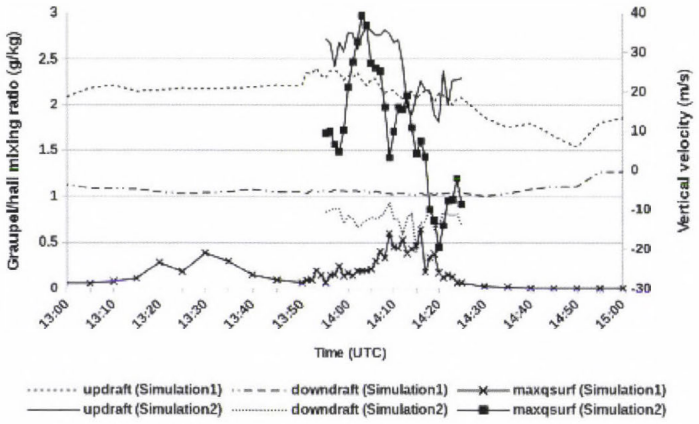

Fig. 11. Time evolution of maximum updrafts and downdrafts (m/s) and the mixing ratios of graupel particles at the lowest model level (g/kg) in the simulated cells in both cases.

It is important to clarify, whether these above mentioned differences between the results of Simulation1 and Simulation2 on the surface are valid also for the volume integrated values of graupel/hail mixing ratios, or they represent the differences only for the maximum values. This problem is critical if the amount of the hail on surfaces is intended to be forecast. Time evolutions of graupel/hail mixing ratios integrated over a square of 196 km^2 are plotted in *Fig. 12*. The location of the center of this square is fitted to the grid point where the mixing ratio of the graupel/hail has maximum value on the surface. *Fig. 12*

also shows the time evolution of the extent of the region where the graupel/hail mixing ratio exceeded 0.001 g/kg on the surface. The comparison of the curves shows, that not only the maximum graupel/hail mixing ratio is larger in Simulation2, but the total amount of graupel/hail mass is also significantly greater. In the case of the areas where the mixing ratio of the graupel/hail is larger than 1 mg/kg, the difference between the two Simulations is not significant, yet Simulation1 gives larger area during a relatively long time period.

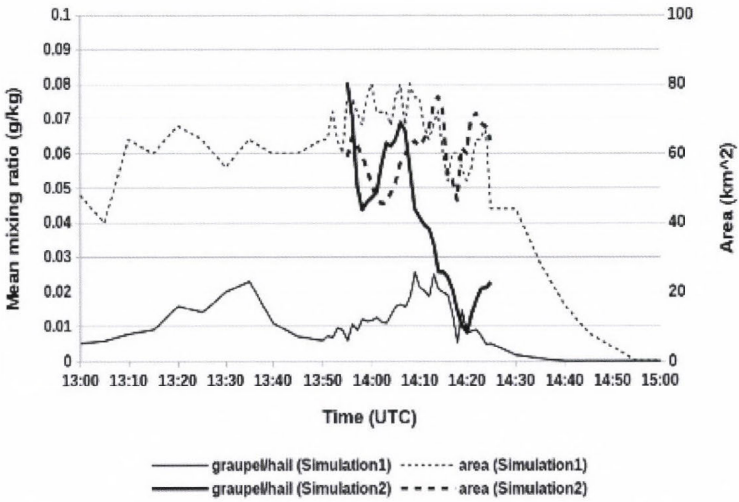

Fig. 12. Time evolution of mean values of graupel particle mixing ratios (g/kg) and the area of graupel mixing ratios above 0.001 g/kg (km^2) at the lowest model level in the simulated cells in both nests for the June 7, 2009 case.

The influence of the spatial resolution on the microphysical properties of the simulated thunderstorm is shown by vertical cross sections of the storm. *Figs. 13a-d* show the cross section calculated in Simulation1 and in Simulation2, respectively. The morphology of the thunderstorm is clearly visible in the case of both resolutions: (i) the horizontally separated updraft and downdraft regions; the rearward tilted updraft region; (ii) the mid-level maximum of the graupel/hail mixing ratios at mid-level; (iii) the WER (in Simulation2, even a slight BWER structure visible at $z = 4$ km – see *Fig. 13d*) at low altitudes due to the intense updraft; (iv) the fall-out of graupel/hail and rain in the rear side of downdraft; (v) the downwind advection of the graupel/hail, snow, and cloud ice (right side of the cross sections) aloft forming an anvil-like structure.

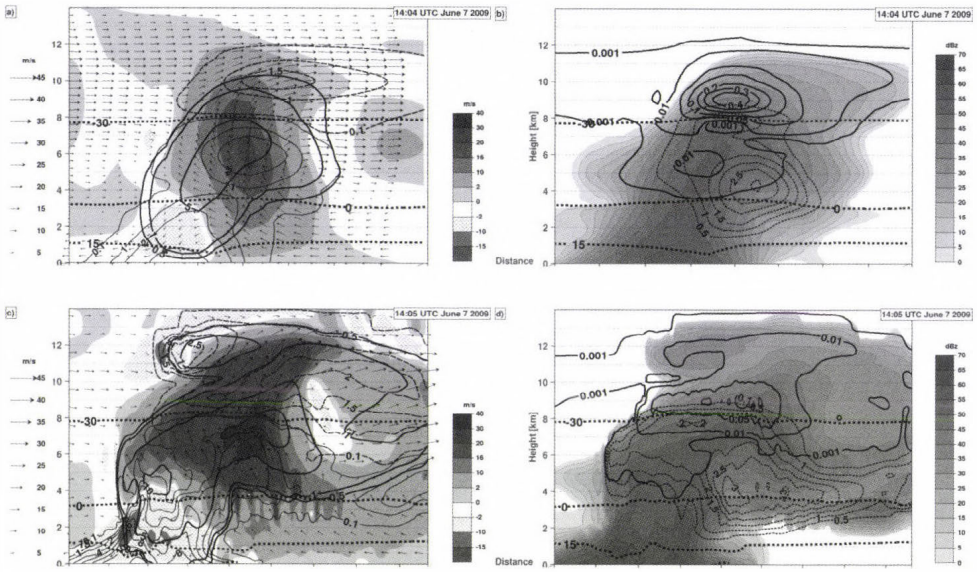

Fig. 13. Vertical cross sections of the thunderstorm in Simulation1 at 14:04 UTC and in Simulation2 at 14:05 UTC on June 7, 2009. The vertical dimension is in km unit. Cross sections in a) and b) were created by Simulation1 and marked by the CD line in *Fig. 9a*. Cross sections in c) and d) were created by Simulation2 and marked by the EF line in *Fig. 9b*. The displayed quantities are the followings:
a) and c): vertical wind speed (shaded), storm-relative streamlines in the plane of the cross section (arrows), graupel mixing ratio (thick solid contours of 0.5, 1, 5, 7.5, 10 g/kg and above 10 g/kg with intervals of 5 g/kg), rainwater mixing ratio (light solid contours of 0.1, 1, and 2 g/kg and above 2 g/kg with intervals of 2 g/kg), and snow mixing ratio (light dashed contours of 0.1, 1 g/kg and above 1 g/kg with intervals of 0.5 g/kg). Thick dashed lines denote the isolines of 15, 0, and –30 °C.
b) and d): simulated radar reflectivity (dBz units), cloud ice mixing ratio (thick solid contours of 0.001, 0.01, and 0.05 g/kg, 0.1 g/kg, and above 0.1 g/kg with intervals of 0.1 g/kg), cloud water mixing ratio (dashed light contours with intervals of 0.5 g/kg), and the isolines of the 0 and –30 °C temperatures (dashed thick contours). Thick dashed lines denote the isolines of 15, 0, and –30 °C.

Nevertheless, the differences between the two cases are also apparent. The updraft intensity in the case of finer resolution is much greater than on the coarser grid (30–40 m/s maximum of updraft velocity in Simulation2 versus 20–30 m/s in Simulation1). The differences in the cloud dynamics correspond to the height of the cloud top. It is about 14 km in the case of Simulation2 and around 12 km in the case of Simulation1 (the cloud ice isoline of 1 mg/kg is defined as an upper boundary of the cloud). The maximum of graupel/hail mixing ratio is between 10–15 g/kg and between 7.5–10 g/kg in Simulation2 (*Fig. 13c*) and in Simulation1 (*Fig. 13a*), respectively. The altitudes of the maximum of graupel/hail mixing ratio are also different in the two cases (~7–8 km versus ~6–

7 km). The mixing ratio of graupel/hail particles on the surface is an important characteristic of the morphology, too. While the isoline of 1 g/kg graupel/hail mixing ratio reaches the surface in Simulation2, even the bottom of the isoline of 0.5 g/kg is above the surface in the case of Simulation1. This means that – in agreements with the previous findings upon the time evolutions in *Fig. 11*, the fine-resolution storm produced considerably greater graupel/hail mixing ratio values on the surface than its coarse-resolution counterpart does. This result has consequences on the the maximum possible hail-size (see Section 3.2.3. for details). In both cases, the location of maximum of graupel/hail mixing ratio mass is in spatial correlation with the maximum of updraft velocity. The significant rearward advection of graupel/hail and rain results in rear-flank downdraft and mixed phase precipitation on the surface (*Figs. 13a* and *c*). The amount of the rain on the surface is almost twice larger in Simulation2 than in Simulation1 (9–10 g/kg versus 4–5 g/kg). Similarly to the previous findings, the high-resolution storm in Simulation2 produced larger simulated radar intensity (*Figs. 13b* and *d*) than in Simulation2 (above 60 dBz versus below 60 dB). It is a remarkable feature that the maximum radar reflectivity is at low-levels in both Simulations which can be attributed to the melting graupel/hail inducing great reflectivity. Considering the isolines of cloud water mixing ratio (*Figs. 13b* and *d*), their structures and maximum values are very similar (~3 g/kg). However, while in Simulation2, the isoline of 1.5 g/kg extends up to 8 km, the top of this isoline is at 6 km in Simulation1. This indicates that due to larger vertical velocities, the cloud water is transported to higher altitudes in Simulation2 than in Simulation1. The cloud ice content is significantly larger in Simulation1 (~0.4 g/kg maximum values) than in Simulation2 (~0.1 g/kg maximum values). In Simulation1, a secondary local maximum can be found at lower levels (between 5 and 6 km). This secondary peak in Simulation2 is absent. The higher amount of cloud ice in Simulation1 can be attributed to the fact that in that simulation, weaker updraft developed which resulted in smaller mean drop diameters. Then the smaller drops transported in sub-zero regions formed ice crystals instead of graupels.

The height of the 0 °C and –30 °C isotherms in *Fig. 13* inside the storms are similar in both cases (height of the 0 °C level is at ~3–4 km, the –30 °C level is at ~8 km). However, in Simulation2, the anomaly of these levels in the updraft region is somewhat larger than in Simulation1. This difference can be explained by the larger releasing latent heat of freezing and condensation in the case of Simulation2. More significant difference can be found if the shapes of the 15 °C isotherms are compared. The shape of this isotherm is affected by the latent heat of cooling due to melting and evaporation. A notable difference is, however, that the maximum of the height anomaly of this isotherm (reaching about several hundreds of meters and being slightly larger in Simulation2) is at the rear edge of the downdraft in Simulation2, while in Simulation1, it is located rather in the forward region of the downdraft.

Not only the intensity of updraft, but the strength of the downdraft is also strongly affected by the spatial resolution (*Figs. 13a* and *c*): the downdraft is more intense in Simulation2 than in Simulation1. The maximum value of downdraft is above 15 m/s in the case of Simulation2 and it is about 10 m/s in the case of Simulation1. Not only the maximum value of the downdraft is larger in the case of Simulation2, but the downdraft region is deeper, as well (~4 km versus ~3 km deep). The overlapping of the downdraft region, the height anomaly of the 15 °C isotherm, and the region where the graupel/hail mixing ratio is large suggest that the intensity of downdraft depends on the loading effect (represented by the sum of the mixing ratios of the precipitation elements – rain and graupel/hail particles) and on the cooling caused by the melting and evaporation of these species.

In order to identify the location and sources of the formation and growth of graupel/hail particles, production terms are plotted in *Fig. 14* in the same vertical cross sections as in *Fig. 13*. The following production terms are considered: (i) accretion of graupel/hail particles by rain drops; (ii) freezing of supercooled rain drops; (iii) freezing of supercooled rain drops due to the collision with cloud ice particles; (iv) riming of graupel/hail particles due collision with cloud drops; (v) collision between rain drops and snowflakes. The other sources, like evaporation/sublimation, snow-graupel/hail conversion through riming, and ice multiplication were found to be negligible comparing to the other, above mentioned terms (see *Fig. 15* for discussion). *Fig. 14* shows that most of the graupel/hail particles were formed in cloud volume between the altitudes of 3 km and 9 km. The vertical extension of this volume does not depend on the applied spatial resolution. Above and below that layer, the existence of graupel/hail is mainly due to the advection/convection and fall-out processes. The midlevel accretion rates of graupel/hail particles (*Figs. 14a* and *c*) by rain are similar in Simulation1 and Simulation2 ($\sim 10 \cdot 10^{-3}$ g/(kg·s)). However, the maximum of the riming rates of graupel/hail particles by cloud water (*Figs. 14a* and *c*) was significantly larger in the case of Simulation2 than in the case of Simulation1. ($\sim 15 \cdot 10^{-3}$ g/(kg·s) versus $\sim 10 \cdot 10^{-3}$ g/(kg·s)), which is a direct consequence of greater transport of cloud water by stronger updraft (refer to *Figs. 13b* and *d*). The larger amount of the rain between the melting level and the surface in Simulation2 (refer to *Fig. 13a* versus *Fig. 13c*) is the consequence of the melting of larger graupel/hail content. The collision between rain and snow much less efficiently produces graupel/hail particles than freezing of the rain drops. In Simulation2, it operates only in the right flank of the midlevel updraft, under the forward sheared anvil, where the snow begins to descend and can encounter to some amounts of rain. However, in the case of Simulation1, besides the anvil region, there is another and more significant maximum of this process in the updraft at around 7 km, as well.

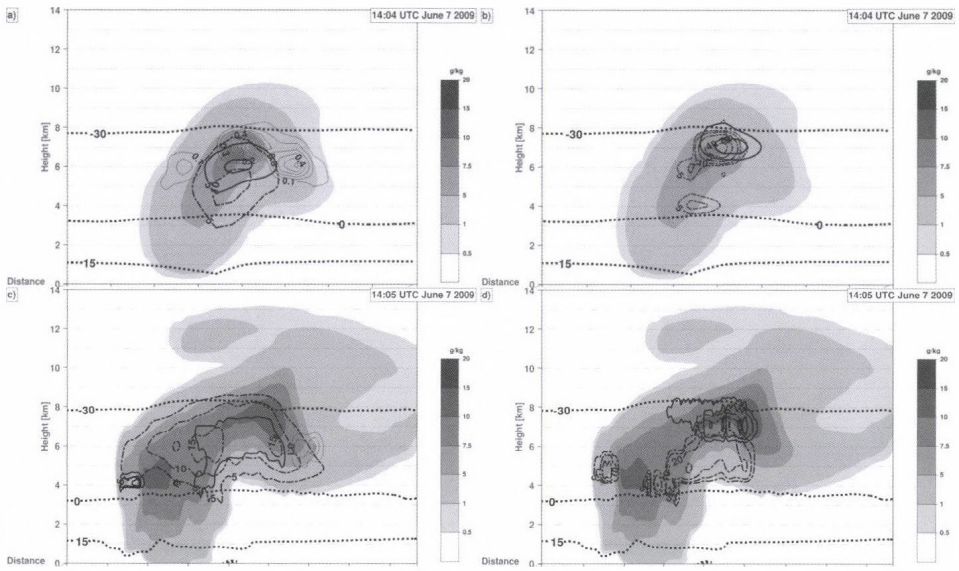

Fig. 14. Vertical cross sections of graupel production terms through the simulated thunderstorm on June 7, 2009 a) and b) in the case of Simulation1 at 14:04 UTC, c) and d) in the case of Simulation2 at 14:05 UTC. The orientation of cross sections is identical to the ones in *Fig. 13* (marked in *Fig. 9*). The displayed quantities are the followings:
a) and c) Shading represents the graupel mixing ratio (scale and legend are displayed in the pictures), thick solid lines show the values of production due to rain and graupel collision (contoured with intervals of $10 \cdot 10^{-3}$ g/(kg·s) and the minimum value is $5 \cdot 10^{-3}$ g/(kg·s)), the thick dot-dashed lines depict the accretion rate of cloud water by graupel (with contour intervals of $5 \cdot 10^{-3}$ g/(kg·s)), the light solid lines represent the collision between rain and snow (with contour intervals of $0.1 \cdot 10^{-3}$ g/(kg·s)) Thick dashed contours represent the isolines of 15, 0 and –30 °C.
b) and d) Shading represents the graupel mixing ratio (the scale and legend is displayed in the pictures), thick solid lines represent the freezing process of supercooled rainwater (contoured with intervals of $10 \cdot 10^{-3}$ g/(kg·s) and the minimum value is $5 \cdot 10^{-3}$ g/(kg·s)), the light dot-dashed lines show the production rate due to collision between rain and cloud ice (contoured with intervals of $10 \cdot 10^{-3}$ g/(kg·s), and the minimum value is $5 \cdot 10^{-3}$ g/(kg·s)). The thick dashed contours represent the isolines of 15, 0 and –30 °C.

The production rate by collision between supercooled rain drops and cloud ice particles (*Figs. 14b* and *d*) is two times smaller in the case of Simulation2 than in the case of Simulation1. This can be due to the larger cloud ice content aloft in Simulation1 (refer to *Fig. 13b*). A local maximum of this production rate can be also observed just above the melting level. This stems from the fact, that the ice crystals can form due to the break of the small ice fragments from the surface of the graupel/hail particles due to the collision between the graupel/hail particles and water drops (ice multiplication – *Hallet* and *Mossop*, 1974). The graupel/hail formation due to the freezing of the supercooled rain drops mostly occur in the region between the height of 6 and 8 km. The freezing rate is about two times larger in the case of Simulation2 than in the case of Simulation1 (~20–30·10^{-3} g/(kg·s) versus ~10–15·10^{-3} g/(kg·s)).

Time evolution of the volume integrated values of the above mentioned production terms were also investigated. The storm was divided into three volumes: (i) 8–14 km, (ii) 3–8 km, and (iii) 0 (surface) – 3 km. Production terms integrated over these volume characterize the microphysical processes in the low-, mid-, and upper-level parts of the storm. Results are summarized in *Fig. 15*. *Figs. 15a* and *b*, imply a clear evidence, that above $z = 8$ km, the graupel/hail mainly forms by the freezing of supercooled rain water and grows by collecting of supercooled cloud water. Another important process affecting the mixing ratio of graupel/hail is the transport by the vertical velocity (not shown) from lower elevations. Analysis of the plots in *Figs. 15a* and *b* shows that the sum of production terms integrated in time is much lesser than the graupel/hail mass formed in this volume, therefore, there has to be other sources than the productions of it. In the model, the only other source is the transport by convection. This confirms that besides the microphysical processes, the three-dimensional advection also plays important role in the evolution of the three dimensional structure of the graupel/hail particles. Due to the larger updraft in the case of Simulation2, significantly more graupel/hail particles can accumulate in the region above the height of 8km. The stronger convection of the cloud drops results in more efficient graupel/hail formation by freezing and larger riming rate as well.

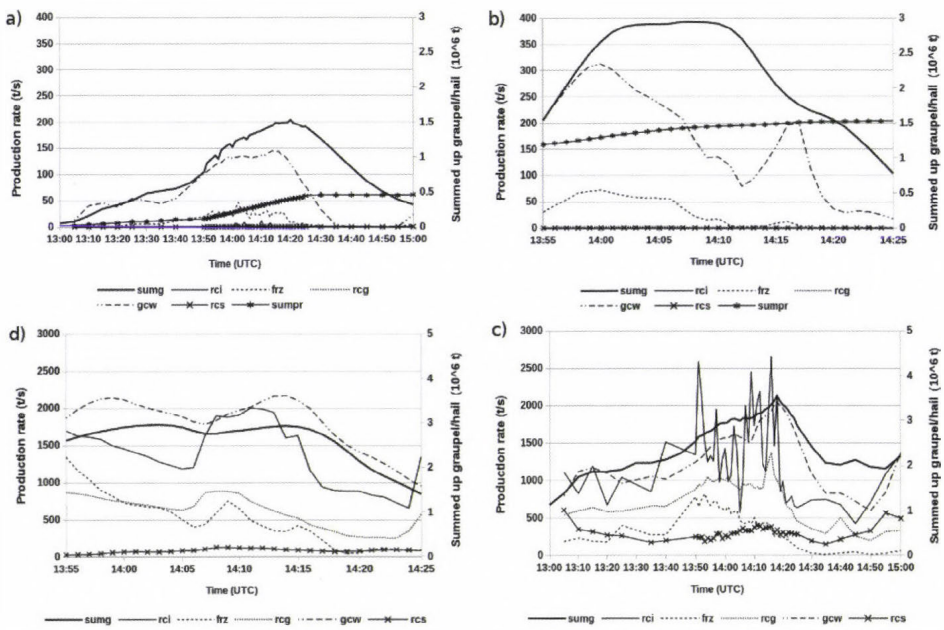

Fig. 15 a)-d). Time evolution of graupel production terms (in t/s), and graupel mass integrated over the volume of the storm a) between 8 and 14 km altitudes in the case of Simulation1, b) between 8 and 14 km altitudes in the case of Simulation2, c) between 3 and 8 km altitudes in the case of Simulation1, d) between 3 and 8km altitudes in the case of Simulation2. Abbreviations are the same as in *Figs. 10 c* and *d*. Curve sumg represents the total graupel content (in 10^6 t). While curve sumpr in a) and b) depicts the sum of all production terms integrated in time (in 10^6 t).

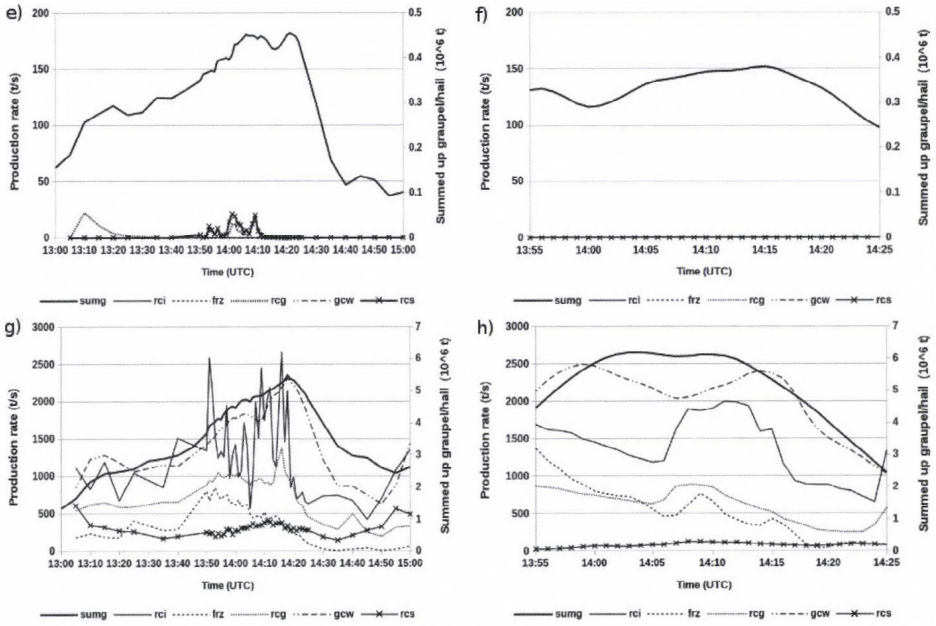

Fig. 15 e)-h). Time evolution of graupel production terms (in t/s), and graupel mass integrated over the volume of the storm e) between 3 km and the surface in the case of Simulation1, f) between 3 km and the surface in the case of Simulation2, g) over the whole column of the storm in the case of Simulation1, h) over the whole column of the storm in the case of Simulation2. Abbreviations are the same as in *Figs. 10 c* and *d*. Curve sumg represents the total graupel content (in 10^6 t).

Most of the graupel/hail content can be found in the middle region (between 3 and 8 km) in both cases (*Figs. 15c* and *d*). While the maximum of the graupel/hail mixing ratio was larger in the case of Simulation2 than in the case of Simulation1, the difference between the volume integrated values is nearly the opposite: the maximum of the volume integrated graupel/hail mass is between $3 \cdot 10^6$ and $4 \cdot 10^6$ T in Simulation1, while in Simulation2 it remains below $3 \cdot 10^6$ T during the Simulation. Most of graupel/hail particles formed by heterogeneous freezing of rain drops and freezing of supercooled rain drops due to collision with cloud ice. The latter process shows a rather hectic behavior with large jumps in intensity in Simulation1 with larger maximum than in Simulation2. This difference between the Simulations can be attributed to the greater cloud ice content in midlevels in Simulation1 (see again *Figs. 13b* and *d*). Formation of the graupel/hail particles was significantly affected by the horizontal resolution. As for the heterogeneous freezing of supercooled rain drops, Simulation2 produced similar rates as Simulation1. The amount of

graupel/hail formed by collision of snowflakes and rain drops was negligible in the case of Simulation2, however, in Simulation1, especially in the first minutes of the period, the snow-rain interaction played non-negligible role in creating graupel/hail (it even exceeds the production rate of the freezing of rain) and was more significant than in Simulation2 throughout the period. Subsequent growth of graupel/hail was largely driven by the accretion processes (accretion by cloud water and rain drops). In both simulations, accretion of graupel/hail by cloud water was more efficient than by rain water.

In the low-level region of the storm, below $z = 3$ km, which is the melting layer, positive values of graupel production are negligible according to *Figs. 15e* and *f*, and there is only one sink term: the sublimation of graupel particles. Production due to collision processes with rain and cloud drops is exactly zero, because in the melting region, all the liquid water amount collided with graupel particles is instantaneously shed to form rain drops. In the case of the total graupel/hail amount in this layer, Simulation1 exceeds the values of Simulation2 at the main part of the integration. This means that the cell in Simulation1 produced more graupel/hail at lower levels than its high-resolution counterpart, though this relation is not valid for the mean graupel/hail values at the surface according to the previous results (see *Fig. 12*). One explanation of this contradiction is that under a certain threshold of mixing ratio, all the graupel/hail particles melt during its falling. If this threshold is exceeded – this could be the case in Simulation2, where we found higher maximum values –, then there is some amount of solid particles which do not melt and, therefore, reach the surface. Based on these results, we can state that compared to its coarser counterpart, the finer resolution Simulation created a storm which produced higher low-level maximum values of graupel/hail mixing ratio but less total graupel/hail content than the storm simulated on the coarser resolution.

Figs. 15g and *h* shows that the total amount of graupel/hail formed in the whole cloud volume only slightly depends on the horizontal resolution ($6 \cdot 10^6$T in the case of Simulation2 versus $5.5 \cdot 10^6$ T in the case of Simulation1). In both cases, most of the graupel/hail particles formed by freezing of supercooled rain due to collision with cloud ice and due to heterogeneous freezing. In both Simulations, the first process is dominant over the second one. While in Simulation1 there is a non-negligible contribution to graupel/hail production by the rain-snow collision, this process has a negligible effect in the case of Simulation2. The graupel/hail particles subsequently grow by collision with cloud and rain water. The accretion by cloud water was more efficient than by rain water, in both simulations.

3.2.3. Results of the maximum hail size calculation method

According to Eqs. (4) and (6), the maximum size of the graupel/hail particles is a function of their mixing ratio. The shape of this function is similar to that of

the square root function (*Fig. 16*). This means that the value of the maximum hail size is more sensitive to the mixing ratio if the value of the mixing ratio is small, and near linearly increases with the mixing ratio above the value of 4 g/kg. Because Simulation1 and Simulation2 cases gave different amounts of graupel/hail on the surface (*Fig. 11*), the maximum hail sizes are expected to be also significantly different. Time evolutions of the largest maximum hail size on the surface are plotted in *Fig. 17*. The figure shows that the maximum hail size calculated by Simulation1 was less than 2 cm during most of the Simulation time; it increases above 2 cm only in a short time period of 10 minutes. However, the forecast maximum hail size in Simulation2 is above 3 cm almost throughout the whole time period and comes near to maximum value of 5 cm. According to the photo documentations and inflicted damages described in Section 3.2.1., the implemented hail size method yielded diameters closer to the observations in the case of Simulation2 than in the case of Simulation1.

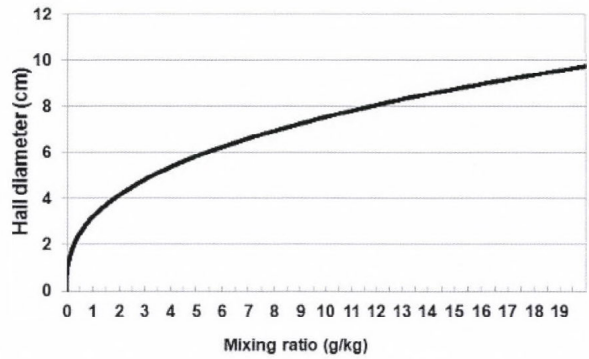

Fig. 16. The dependence of the hail size diameter (calculated by the method - cm) on the graupel mixing ratio (g/kg). The calculation was done in an environment of the following atmospheric conditions: T (temperature) = 25 °C, P (pressure) = 101000 Pa, r (water vapor mixing ratio) = 5 g/kg.

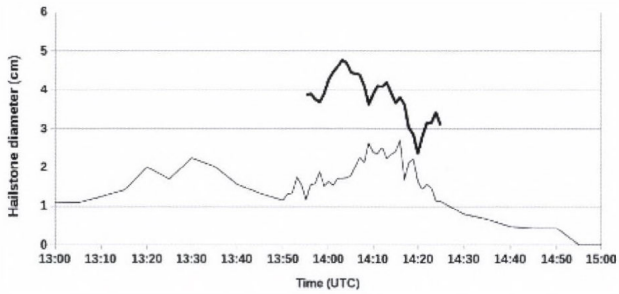

Fig. 17. Time evolution of the maximum hail size at the lowest model level. Light and thick solid lines denote the forecast maximum sizes in the case of Simulation1 and Simulation2, respectively. The units are cm (as diameters).

To illustrate the typical horizontal distribution of the expected hail sizes on the ground, horizontal cross sections of calculated hail sizes at the lowest model level are displayed at a given time in *Figs. 18a* and *b*. The maximum values in Simulation1 slightly exceeds 2.5 cm in one grid point which represents a 4 km^2 area. The maximum in-storm hail size in the finer simulation is above 4.5 cm on an area of roughly 1 km^2, and the isoline of 2.5 cm encloses an area of around 8 km^2, which is twice as high as in Simulation1. That is, the simulation with higher resolution resulted in not only larger maximum hail sizes, but the area exposed by these larger hail stones is also significantly larger in Simulation2 than in Simulation1.

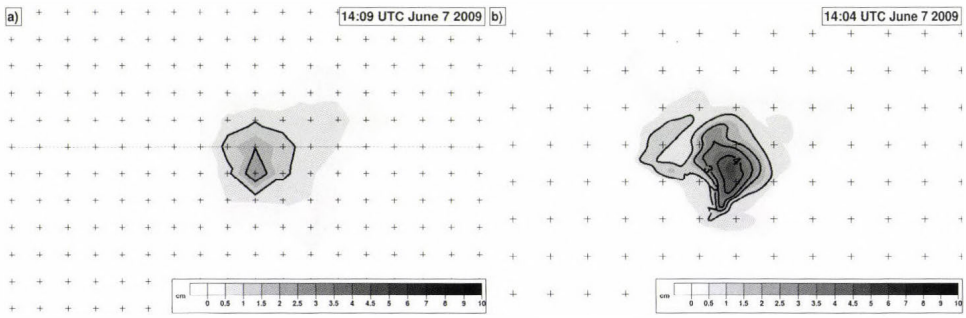

Fig. 18. Horizontal cross sections of the maximum hail sizes produced by the storm at the lowest model level a) Simulation1 at 14:09 UTC and b) Simulation2 at 14:04 UTC. The scale of the shading is as in the legend, its isolines are denoted by black solid lines. The distance between two neighboring crosses represents 2 km on both nests.

4. Summary and conclusion

In this paper, an algorithm was developed to evaluate a forecast method for the maximum hail size on the ground. The input data for this algorithm are given by WRF-ARW model with the Thompson's one-moment microphysical scheme, which treats graupel and hail as one hydrometeor category (graupel/hail). Besides that, a detailed analysis was made to reveal the dependence of microphysical processes (focusing on the graupel/hail formation and growth) on the horizontal resolution. The results were evaluated on two nests with horizontal resolution of 2 km (Simulation1) and 100 m (Simulation2). In order to better understand the mechanisms led to graupel/hail formation in the cloud, the production terms responsible for the graupel/hail formation and growth were also analyzed. A case study of a supercell produced large and damaging hail was selected to achieve these goals. Both Simulations were able to reproduce the main characteristics of the observed supercell, such as: radar reflectivity,

morphology, and vorticity fields. On the other hand, the details of these properties were significantly better simulated if the finer resolution was used.

The Simulation with finer resolution resulted in larger maximum values of graupel/hail and rain mixing ratios, but smaller maximum mixing ratios of cloud ice were calculated. The location of the maximum of graupel/hail mixing ratio was found in the updraft region between the heights of 5 and 8 km in both cases. The maximum values of cloud water and snow mixing ratio were found to be similar in both Simulations. Although the maximum of the graupel/hail mixing ratio was significantly larger in the case of Simulation2 than in the case of Simulation1, considering the total mass of graupel/hail particles in the storm, the two Simulations produced almost the same amount. The higher maximum values can be explained by the stronger updrafts occurred in the case of Simulation2. The stronger updraft resulted in more intense upward flux of water vapor, and it was able to held larger amount graupel/hail aloft. In addition, due to the stronger updraft in Simulation2, the maximum graupel/hail mixing ratio was located at higher altitudes than in Simulation1. The maximum of downdraft velocity was also larger in the case of Simulation2 due to the larger loading effect and cooling rate by melting and evaporation.

The graupel/hail in the storm formed mainly by the freezing of supercooled rain due to its collision with cloud ice, and secondly, by the heterogeneous freezing of supercooled rain. Nevertheless, the latter process was more intense in the finer Simulation than in its counterpart, while the rain-cloud ice collision at times was found more effective graupel/hail producer in Simulation1 than in Simulation2. This latter difference and the smaller maximum of graupel mixing ratio aloft, too, can be attributed to the larger amount of cloud ice remained in Simulation1, because the weaker updraft in that case produced smaller water drops which subsequently formed ice crystals instead of graupel particles. In addition, in the case of Simulation1, rain-snow collision resulted in significant amount of graupel/hail. The formed graupel/hail content subsequently grew mainly by the accretion by cloud water, and to a lesser extent, the accretion by rain water. However, the overall greater formation rate of graupel/hail resulted in more efficient accretion. The analysis of production terms in the various layers of the storm shows, that the most of the graupel/hail particles were formed between the height of 3 and 8 km, while above and below of this layer, the graupel/hail particles were mainly transported by the advection and by their fallout falling.

The application of both Simulations resulted in reasonable maximum hail size on the surface. However, significantly larger maximum hail size (around 4 cm) was forecast in the case of Simulation2 than in the case of Simulation1 (about 2 cm). In addition, the horizontal extent of the area with large hail size (above 2 cm) was about twice larger in the case of Simulation2than in the case of Simulation1.

The method for the forecast of maximum hail size can be applied not only in supercell cases but with ordinary and multicell storms, as well. Therefore, in the future, more case studies involving these types of storms must be elaborated to test the universal abilities of this method. In addition, numerical Simulation with other two-moment microphysics schemes (*Morrison et al.*, 2005; *Milbrandt* and *Yau*, 2005; etc.) which allow greater degree of freedom on the size distribution should be performed to investigate their effect on the surface. Though the Simulation on the 100 m resolution nest was performed with applying a PBL scheme, it is necessary to clarify whether using a LES closure in that range ("terra incognita") would lead to consistent results.

References

Adlerman E.J., and *Droegemeier, K.K.*, 2002: The sensitivity of numerically simulated cyclic mesocyclogenesis to variations in physical and computational parameters. *Mon. Weather Rev. 130*, 2671–2691.

Brimelow, J.C., Reuter, G.W., and *Poolman, E.P.*, 2002: Modeling maximum hail size in Alberta thunderstorms. *Weather Forecast. 17*, 1048–1062.

Brimelow, C. and *Reuter, G.W.*, 2006: Spatial Forecasts of Maximum Hail Size Using Prognostic Model Soundings and HAILCAST. *Weather Forecast. 21*, 206–219.

Browning, K.A., 1968: The organization of severe local storms. *Weather 23*, 429–434.

Bryan, G.H., Wyngaard, J.C., and *Fritsch, J.M.*, 2003: Resolution requirements for the simulation of deep moist convection. *Mon. Weather Rev. 131*, 2394–2416.

Changnon, S.A., Pielke, R.A. Jr., Changnon D., Sylves, R.T., and *Pulwarty, R.*, 2000: Human factors explain the increased losses from weather and climate extremes. *B. Am. Meteorol. Soc. 81*, 437–442.

Craig, C.G. and *Dörnbrack, A.*, 2008: Entrainment in cumulus clouds: What resolution is cloud-resolving? *J. Atmos. Sci. 65*, 3978–3988.

Ćurić, M., and *Janc, D.*, 1989: The behavior of a hailstone in a forced 1-D Cb cloud model. *Meteorol. Atmos. Phys.* 41, 45–54.

Ćurić, M., and *Janc, D.*, 1993: Predictive capability of a one-dimensional convective cloud model with forced lifting and a new entrainment formulation. *J. Appl. Meteorol. 32*, 1733–1740.

Doswell III, C.A., 1996: What is a supercell?. Preprints 18th Conf. Severe Local Storms (San Francisco, CA). Amer. Meteor. Soc, 641.

Farley, R.D. and *Orville, H.D.*, 1986: Numerical Modeling of Hailstorms and Hailstone Growth. Part I: Preliminary Model Verification and Sensitivity Tests. *J. Climate Appl. Meteorol. 25*, 2014–2035.

Farley, R.D., 1987a: Numerical Modeling of Hailstorms and Hailstone Growth. Part II: The Role of Low-Density Riming Growth in Hag Production. *J. Clim. Appl. Meteorol. 26*, 234–254.

Farley, R.D., 1987b: Numerical Modeling of Hailstorms and Hailstone Growth. Part III: Simulation of an Alberta Hailstorm—Natural and Seeded Cases. *J. Clim. Appl. Meteorol. 26*, 789–812.

Fawbush, E.J., and *R.C. Miller*, 1953: A method of forecasting hailstone size at the earth's surface. *Bull. Amer. Meteorol. Soc. 34*, 235–244.

Fiori, E., Parodi, A., and *Siccardi, F.*, 2010: Turbulence Closure Parameterization and Grid Spacing Effects in Simulated Supercell Storms. *J. Atmos. Sci. 67*, 3870–3890.

Geresdi, I., 1990: Two-dimensional simulation of a small hailstorm. *Időjárás 94*, 346–359.

Geresdi, I., 1996: Precipitation formation in a severe thunderstorm. *Atmos. Res. 41*, 71–81.

Geresdi, I., 1998: Idealized simulation of the Colorado hailstorm case: Comparison of bulk and detailed microphysics. *Atmos. Res. 45*, 237–252.

Geresdi, I., Horváth, Á., and *Mátyus, Á.*, 2004: Nowcasting of the precipitation type Part II: Forecast of thunderstorms and hailstone size. *Időjárás 108*, 33–49.

Grabowski, W.W., Wu, X., Moncrieff, M.W., and *Hall, W.D.,* 1998: Cloud-resolving modeling of tropical cloud systems during phase III of GATE. Part II: Effects of resolution and the third spatial dimension. *J. Atmos. Sci. 55*, 3264–3282.

Grell, G.A., and *Dévényi, D.,* 2002: A generalized approach to parameterizing convection combining ensemble and data assimilation techniques. *Geophys. Res. Lett., 29(14),* Article 1693.

Hallett, J., and *Mossop, S.C.,* 1974: Production of secondary ice particles during the riming process, *Nature 249*, 26–28.

Horváth, Á. and *Geresdi, I.,* 2003: Severe storms and nowcasting in the Carpathian Basin. *Atmos. Res., 67–68*, 319–332.

Horváth, Á., Geresdi, I., Németh, P., Csirmaz, K., and *Dombai, F.,* 2009: Numerical modeling of severe convective storms occurring in the Carpathian Basin. *Atmos. Res. 93*, 221–237.

Johnson, D.E., Wang, P.K., and *Straka, J.M.,* 1993: Numerical Simulations of the 2 August 1981 CCOPE Supercell Storm with and without Ice Microphysics. *J. Appl. Meteorol. 32*, 745–759.

Johnson, D.E., Wang, P.K., and *Straka, J.M.,* 1995: A study of microphysical processes in the 2 August 1981 CCOPE supercell storm. *Atmos. Res. 33*, 93–123.

Klemp, J.B., 1987: Dynamics of tornadic thunderstorms. *Annual Rev. Fluid Mech. 19*, 396–402.

Lemon, L.R., and *Doswell III, C.A.,* 1979: Severe thunderstorm evolution and mesocyclone structure as related to tornadogenesis. *Mon. Weather Rev. 107*, 1184–1197.

Mellor, G.L. and *Yamada, T.*, 1982: Development of a turbulence closure model for geophysical fluid problems. *Rev. Geophys. Space Phys.*, 20, 851–875.

Milbrandt, J.A. and *Yau, M.K.,* 2005: A multimoment bulk microphysics parameterization. Part I: Analysis of the role of the spectral shape parameter. *J. Atmos. Sci. 62*, 3051–3064.

Milbrandt, J.A. and *Yau, M.K.,* 2006: A Multimoment Bulk Microphysics Parameterization. Part III: Control simulation of a Hailstorm. *J. Atmos. Sci. 63*, 3114–3136.

Miller, R.C., 1972: Notes on analysis and severe-storm forecasting procedures of the Air Force Global Weather Central. Air Weather Service Tech. Rep. 200 (Rev.), Air Weather Service, Scott Air Force Base, IL, 190 pp. [Available from Air Weather Service Technical Library, 859 Buchanan St., Scott AFB, IL 62225-5118.]

Moore, J.T. and *Pino, J.P.,* 1990: An interactive method for estimating maximum hailstone size from forecast soundings. *Weather Forecast. 5*, 508–526.

Morrison, H., Curry, J.A., and *Khvorostyanov, V.I.,* 2005: A new double-moment microphysics parameterization for application in cloud and climate models, Part I: Description. *J. Atmos. Sci. 62*, 1665–1677.

Ogura, Y., and *Takahashi, T.,* 1971: Numerical simulation of the life cycle of a thunderstorm cell. *Mon. Weather Rev. 99*, 895–911.

Orville H.D. and *Kopp, F.J.,* 1977: Numerical simulation of the Life History of a Hailstorm. *J. Atmos. Sci. 34*, 1596–1618.

Petch, J.C., Brown, A.R., and *Gray, M.E.B.*, 2002: The impact of horizontal resolution on the simulations of convective development over land. *Q. J. Roy. Meteor. Soc. 128*, 2031–2044.

Putsay, M., Simon, A., Szenyán, I., Kerkmann, J., and *Horváth, Gy.,* 2011: Case study of the 20 May 2008 tornadic storm in Hungary — remote sensing features and NWP simulation. *Atmos. Res. 100*, 657–679.

Reisner, J., Rasmussen, R.M., and *Bruintjes, R.T.,* 1998: Explicit forecasting of supercooled liquid water in winter storms using the MM5 mesoscale model. *Q. J. Roy. Meteor. Soc. 124*, 1071–1107.

Renick, J.H., and *Maxwell, J.B.,* 1977: Forecasting hailfall in Alberta. Hail: A Review of Hail Science and Hail Suppression, Meteor. Monogr., No. 38, Amer. Meteor. Soc., 145–151.

Simpson, J. and *Wiggert, V.,* 1969: Models of precipitating cumulus towers. *Mon. Weather Rev.* 97, 471–489.

Skamarock, W.C., Klemp, J.B., Dudhia, J., Gill, D.O., Barker, D.M., Duda, M.G., Huang, X.-Y., Wang, W., and *Powers, J.G.*, 2008. A description of the advanced research WRF version 3. NCAR Technical Note NCAR/TN-475+STR, June 2008. 113.

Takahashi, T., 1976: Hail in an Axisymmetric Cloud Model. *J. Atmos. Sci. 33*, 1579–1601.

Talbot, C., Bou-Zeid, E., and *Smith, J.,* 2012: Nested Mesoscale Large-Eddy simulations with WRF: Performance in Real Test Cases. *J. Hydrometeor. 13*, 1421–1441.

Thompson, G., Rasmussen, R.M., and *Manning, K.*, 2004. Explicit forecasts of winter precipitation using an improved bulk microphysics scheme. Part-I: description and sensitivity analysis. *Mon. Weather Rev. 132*, 519–542.

Thompson, R.L., Edwards, R., Hart, J.A., Elmore, K.L., and *Markowski, P.*, 2003: Close proximity soundings within supercell environments obtained from the rapid update cycle. *Weather Forecast. 18*, 1243–1261.

Weinstein, A.I., 1972: Ice-Phase Seeding Potential for Cumulus Cloud Modification in the Western United States. *J. Appl. Meteor. 11*, 202–210.

Wisner, C., Orville, H.D., and *Myers, C.*, 1972: A Numerical Model of a Hail-Bearing Cloud. *J. Atmos. Sci., 29*, 1160–1181.

Wyngaard, J.C., 2004: Toward numerical modeling in the ''terra incognita''. *J. Atmos. Sci. 61*, 1816–1826.

Zoltán, Cs. and *Geresdi, I.*, 1984: A one-dimensional steady-state jet model for thunderclouds. *Időjárás 88*, 21–31.

IDŐJÁRÁS

Quarterly Journal of the Hungarian Meteorological Service
Vol. 119, No. 4, October – December, 2015, pp. 475–491

Examining the probable length in days of wet and dry spells in Khuzestan province

Seyed Hossein Mirmousavi

University of Zanjan, Faculty of Humanities,
University Blvd.,45371-38791, Iran
hossein.mousavi047@gmail.com

(Manuscript received in final form November 11, 2014)

Abstract—This study evaluated the probable length in days of dry and wet spells in Khuzestan province using daily rainfall data from 11 synoptic stations during the period 1990–2012. Transfer matrix calculations and model tests were performed using Matlab software. For interpolation maps, kriging in ARC GIS 10.2 software was used. Results indicated that the probability of dry days occurring in Khuzestan province increases from the south to the north. The highest probabilities of a two-day dry spell were 15% in the north and 12% in the northeast of the province. The probability of a 3-day dry spell in the north and northeast was 10%. Moving to the south and southwest of the province, the probability decreases, amounting to 6% in the southwest. Results of calculations of return periods of wet and dry days showed the probability of the dry-days return period increases from the north to the south. An investigation of the role of general circulation in the creation of wet and dry periods showed that 4 patterns are effective in their production.

Key-words: Markov chain, probability, dry and wet spells, Khuzestan Province.

1. Introduction

Wet spells and dry spells are two main physical characteristics of rainfall occurrence, and the volume of rainfall in a geographical area depends heavily on the distribution of such spells. It is, therefore, important to investigate the occurrence patterns of wet and dry spells scientifically through model-based analysis, that consists of studying the statistical properties of two common indicators, the spell length and spell frequency. Such studies are essential for agricultural planning, water resource management, and other interests such as fisheries, health, ecology, environment, etc. Several kinds of stochastic models

have been used to describe frequency distributions of spell lengths at spatial and temporal levels. The fitted probability distributions of spell lengths under the models are used to study the persistence properties of wet and dry spells. Since spell lengths govern the persistence properties of the daily precipitation process, it is desirable to use a criterion to select the best model from among a series of competitive models that is fitted successfully to the observed datasets.

In order to put our discussion into the proper perspective, we related our work to the existing literature. The model most frequently used to generate consecutive series of dry and wet days is the first-order, two-state, homogeneous Markov chain that has been applied by and is very popular among various researchers, *Todorovic* and *Woolhiser* (1974), *Berger* and *Goossens* (1983), *El_seed* (1987), *Haggstrom* (2002), *Bekele* (2002), *Anagnostopoulou et al.* (2003), *Alasseur et al.* (2004), *Ana* and *Paulo* (2007), *Asakereh* (2009), *Fischer et al.* (2013)). An essential improvement to the reproduction of short and long spells was made by *Berger* and *Goossens* (1983) and *Nobilis* (1986) using the higher order Markov chain and Eggenberger-Polya distribution. They found that short spells were best fitted by the fourth order Markov chain, whereas the Eggenberger-Polya distribution gave the best fit to the long series. *Deni* and *Jemain* (2008) proposed a model constituting two different geometric distributions. In the referred study, both geometric distributions were separated according to the length of dry spells. Results of the works suggested that mixed distribution, including the geometric one, could be promising in reproducing long dry periods. For wet spells, it was also observed that simple geometric distribution could be promising. Recently, following the idea of *Deca et al.* (2010), a mixture distribution based on a weighted sum of two geometric distributions, as well as that of one geometric and one Poisson distribution, was applied by *Mathugama* and *Peiris* (2011). The first model exhibits a good fit for dry spells, and the latter can be employed for wet periods. More recently, *Ababaei et al.* (2012) found that both the Markov chain of order two and negative binomial distribution can be used to estimate wet spells in Qazvin (Iran).

Khuzestan province is one of the most important agricultural areas in Iran. Due to successive droughts, farmers in this province have endured many losses. In this region, the incidence of consecutive dry days is a main factor in increasing the amount of damage to the agricultural sector (*Nadi et al.*, 2012). For this reason, it is necessary to carefully examine the consecutive dry days in the area. The present study examined in detail the ability of the Markov models to analyze the wet or dry condition of a given day in this area.

2. Data

In this study, daily rainfall data was collected from 11 meteorology stations. The period 1990–2012 was chosen for the evaluation of the model. A wet day

was defined as a 24-hour period with total rainfall exceeding 0.1 mm, and a dry day was defined as one with measurable precipitation <0.1 mm. The pressure data used were the NMC grid data in different windows over Europe and Middle East at the grid resolution 2.5°×2.5°. Several geopotential heights (500 hPa and sea level pressure (SLP)) were used. The selected area experienced a large part of the systems affecting Iran during the years (from 1970 to 2013) involved. This region is located within 20–60° N and 20–80° E. Data used from the NCEP site (www.ncep.noaa.gov) is provided.

3. Method

3.1. Markov chains

A Markov chain can be defined as a type of time-ordered probabilistic process that goes from one state to another according to the probabilistic transition rules that are determined by the current state only (*Haggstrom*, 2002). That is, the probability of a day being in a certain state (either wet or dry) is conditioned on the states of the previous periods, where the number of previous periods is termed as the order of the chain.

In the first-order, two-state Markov model, the current state is dependent solely upon the state of the previous period, while in the second–order, two-state Markov chains, the current state is determined by the states of the two previous periods (*Hakimi-Pour*, 1998).

When recording whether a measurable amount of rain has occurred over time at a particular location (2-state time series), data is in the form of a discrete state series. The most commonly used model for discrete state series is a low-order stationary Markov chain. Such models are used to predict the occurrence of certain sequences.

The states of the system are dry and wet. A wet state is defined as a 24-hour period measured from 8:30 a.m. with total rainfall exceeding some threshold amount (0.1 mm). Otherwise, the state is taken as dry (*Zarei* and *Shahkar*, 2002). The discrete state series of rainfall can be represented as X_1, X_2, X_3 , ... ,X_t for a t length sequence, where:

$$X_t = 0, \text{ if day } t \text{ is dry,}$$

$$X_t = 1, \text{ if day } t \text{ is wet.} \quad (1)$$

3.2. First-order Markov model

The probabilities of a first-order Markov chain are defined as:

$$P\{X_t = j \mid X_{t-1} = i\}\ i,j = 0,1\ . \tag{2}$$

The *transition probability* P_{ij}, (where $i, j = 0, 1$) is the probability that if the system is in state i at any observation, it will be in state j at the next observation. As probabilities, the numbers P_{ij} must all lie in the interval [0, 1]. Transitional probabilities for the first order can be expressed as follows:

$$Pij(t) = P\{X_t = j \mid X_{t-1} = i\}\ i,j = 0,1\ . \tag{3}$$

For any fixed i, $\{i = 0, 1\}$, we must have $P_{i0} + P_{i1} = 1$.

This expresses the fact that if the system is in one of the states at one observation, it will with certainty be in one of the two states at the next observation. With these transition probabilities, a 2×2 matrix $\mathbf{P} = \{P_{ij}\}^{T}$, called the transition matrix of the Markov process, can be formed where the sum of the entries in each column of **P** is one.

$$\mathbf{P} = \begin{pmatrix} p_{00} & p_{10} \\ p_{01} & p_{11} \end{pmatrix}. \tag{4}$$

The probability vectors $\boldsymbol{p}^{(n)}$ for $\boldsymbol{n} = 0, 1, 2, \ldots\ldots$ are said to be the state vectors of a Markov process, where $pi^{(n)}$ is the probability that the system is in the ith state at the nth observation. In particular, the state vector $\boldsymbol{p}^{(0)}$ is called the initial probability or initial state vector of the Markov process. If **P** is the transition matrix and $\boldsymbol{p}^{(n)}$ is the state vector at the nth observation, one can write:

$$\mathbf{P}^{(n+1)} = \boldsymbol{p}^{(n)}\mathbf{P} \tag{5}$$

Where $\boldsymbol{p}^{(n+1)}$ is the state vector at the $n+1$th observation. From this it follows that:

$$\mathbf{P}^{(n)} = \boldsymbol{p}^{(0)}\mathbf{P}^{n} \tag{6}$$

i.e., the initial state vector $\boldsymbol{p}^{(0)}$ and the transition matrix **P** determine the state vector $\boldsymbol{p}^{(n)}$ at the nth day. The nth step transition probabilities are called conditional probabilities and is denoted by $P_{ij}^{(n)}$, (where $i, j = 0, 1$) with $\mathbf{P}_{ij}^{(n)} \geq 0$, for n=0,1,2,3…., and:

$$\sum_{j=0}^{1} p_{ij}^{(n)} = 1 \ . \tag{7}$$

$\mathbf{P}^{(n)} = \boldsymbol{p}^{(0)} \mathbf{P}$ in matrix notation for the 1th order Markov chain can be written as (*Chynlar*, 2002):

$$\left(p_0^{(n)} p_1^{(n)}\right) = \left(p_0^{(0)} p_1^{(0)}\right) \begin{pmatrix} p_{00} & p_{10} \\ p_{01} & p_{11} \end{pmatrix} n \ . \tag{8}$$

Moreover, the calculation for the continuation of wet and dry days uses the following equation (*Berger* and *Goossens,* 1983):

$$P_m = \boldsymbol{p}^{m-1} \boldsymbol{q} \tag{9}$$

Return periods of dry and wet days, with the continuity of m-day, is calculated using the following equation:

$$T_m = \frac{1}{\boldsymbol{p}^{m-1} \boldsymbol{q}} \tag{10}$$

One of the main assumptions in Markov chains is stationarity. That is $P_{ij}(t)=P_{ij}$ for $t_k < t < t_{k+T}$ where T is the time interval taken to calculate the transitional probabilities. This assumes that the chance of rain remains constant within T day periods. The data was grouped into 2-day, 3-day, and 5-day groups and studied separately.

To evaluate the strength of the relationship between the occurrence of circulation patterns and rainfall, an index, called performance index (*PI*), is defined to measure the relative contribution of a particular pattern to the total rainfall amount. Specifically, the mean daily rainfall within cluster i is compared with the climatological mean daily rainfall, that is, (*Zhang*, 1995):

$$PI(i) = \frac{R_i/n_i}{R/n}, \tag{11}$$

where n_i is the number of days with pattern i; R_i is the total rainfall during those days; R is the total rainfall received during the study period, and n is the number of days in the study period. If *PI* is less than 1 in rainy weather, the pattern has no effect, and the placement of the pattern in the atmosphere of an area can be consecutive dry. If *PI* index is more than 1, consecutive wet days in the region will be created.

In order to assess the impact of dry periods on water resources and agricultural yield, linear regression and polynomial regression methods with the following equations were used:

$$\mu_{y|x} = \beta_0 + \beta_1 X \ . \tag{12}$$

$$Y = \beta_0 + \beta_1 X + \beta_2 X^2 + \ldots + \beta_{p-1} X^{p-1} + \varepsilon \ . \tag{13}$$

4. *Study area*

The province of Khuzestan, which occupies an area of 63,213 km^2 in southwestern Iran, is located between 48°E and 49.5°E longitudes and between 31°N and 32°N latitudes (*Fig. 1*). Topographic elevations in the province vary between 0 and 3740 m. The climate of the study area varies from arid to humid. The northern parts of the province experience cold weather, whereas the southern parts experience tropical weather. Summer is from April to September, whereas winter is from October to March. Annual mean of maximum summer temperatures in the province is about 50 °C (in July) and minimum winter temperature is 9 °C (in March). The annual amounts of rainfall are 165–200 mm in the southwest and 433–480 mm in the northeast, and about 70% of annual rainfall events occur from February to April (*Fig. 2*). The annual evaporation is 1500–2800 mm.

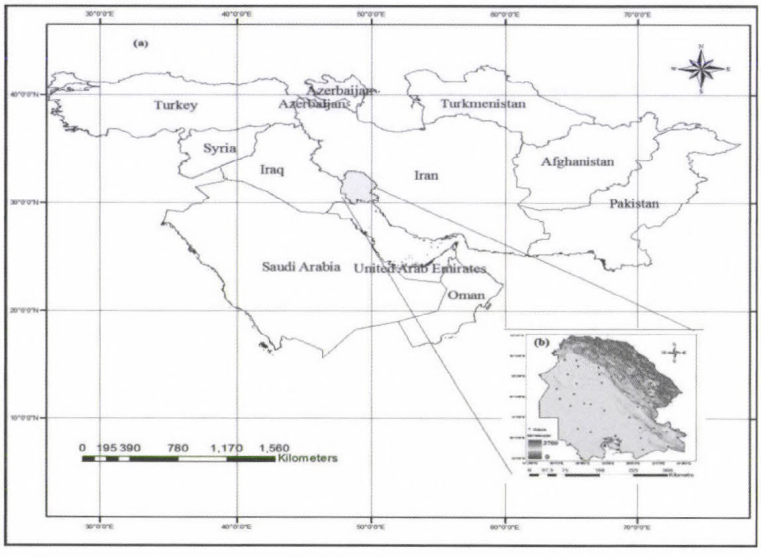

Fig. 1. Khuzestan province: (a) location in Iran; (b) Digital elevation model and locations of the studied stations.

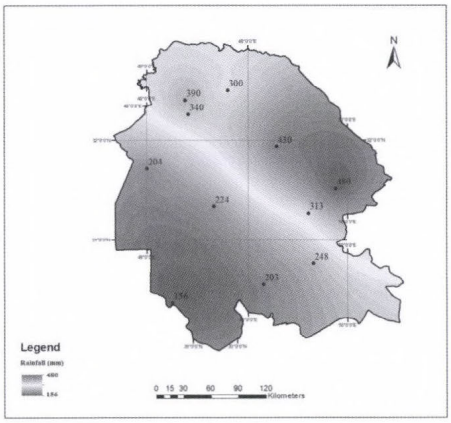

Fig. 2. Average annual rainfall in the Khuzestan Province.

5. *Results*

The calculation results showed that in Khuzestan province from the south to the north, the probability of dry days decreases. Maximum probability of dry days is found in the central and southwestern parts of the province (92%). This means that, on average, in the southwest part of the study area, 336 days per year are dry. The minimum probability of dry days was found in the northern region (74%). This means that in northern Khuzestan, on average, the probable number of dry days per year is 270. Overall, the average probability of dry days in Khuzestan province was 86%(*Fig. 3*).

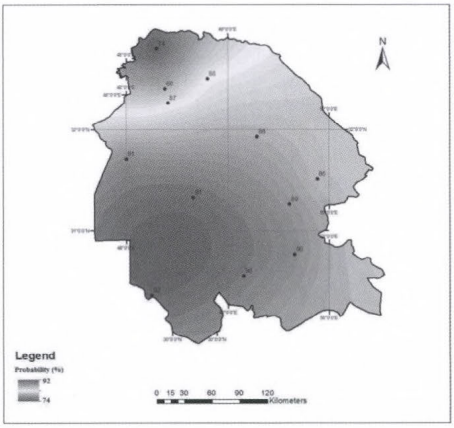

Fig. 3. Map of the dry day's probability (%).

An examination of the probability of a 2-day dry spell showed higher probabilities in the north (15%) and northeast (12%) than elsewhere in the study area. In the south and southwest, the probability of a 2-day dry spell is reduced so that in the southwest of the province, this rate reached the minimum amount of 6% (*Fig. 4*). Assessments showed that the probability for a 3-day dry spell in the north and northeast of the study area is approximately 10% and in the southwest of the province, the probability is equal to 6% (*Fig. 5*). Also, the probability of a dry spell lasting five days is less than that for a 3-day dry spell, so that the maximum value is in the northeast province (7%) and the minimum value is in the southern region at almost 2% (*Fig. 6*).

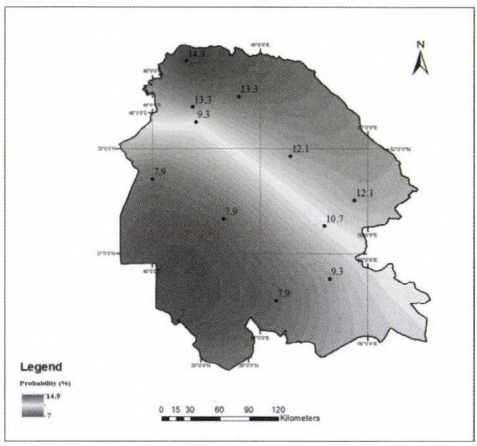

Fig. 4. Map probability of two days dry spell lengths (%).

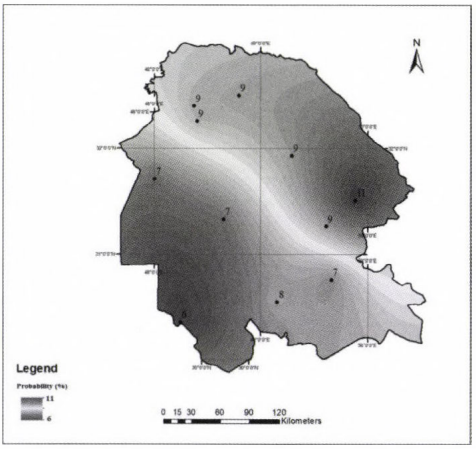

Fig. 5. Map probability of three days dry spell lengths (%).

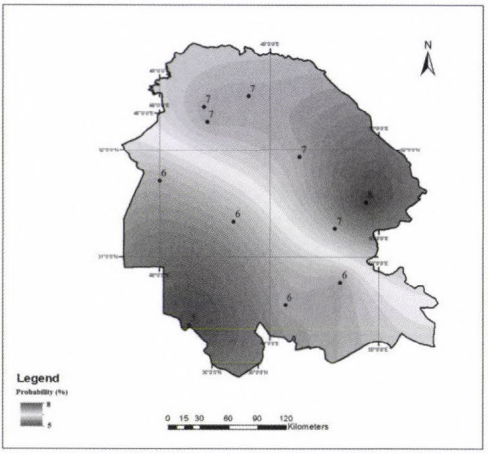

Fig. 6. Map probability of five days dry spell lengths (%).

5.1. Return period of 2-5-day dry spell

Calculating return periods of 2- to 5-day dry spells showed that the minimum length of a dry spell is 2 days, which occurred in the north and northeastern parts of Khuzestan province. This means that the probability of a dry spell lasting two days is higher in the north and northeast than in the south and southwest. Accordingly, the probable return period of a 2-day dry spell in the southwest of the province is, on average, 15 days, while in the north, the return period occurs once every 7 days. Studies have shown that most 2-day dry spells occur in the southwest of the province (*Fig. 7*).

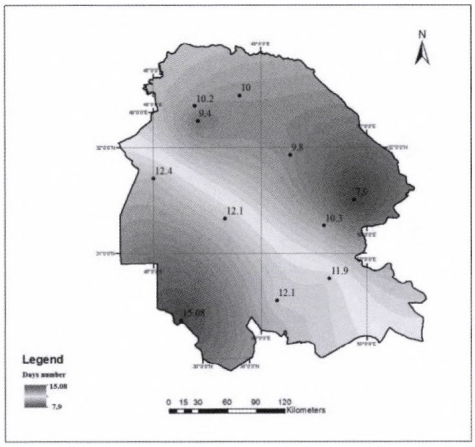

Fig. 7. Map of the persistence of a 2-day dry spell return period.

When the length of a dry spell increases to 3–5 days, the return period also increases; however, this data at the provincial level becomes a little slower. Evaluations showed that in the north and northeast of the province, the potential return period of the 3-day dry spell is once every 10 days, and the probability in the southwest province is once every 16 days (*Fig. 8*). The probability of the return period of a 5-day dry spell is much like that of a 3-day period. Every 17.5 days in the southern part of Khuzestan province and every 12.8 days in the northeast, the return period of a 5-day dry spell occurs (*Fig. 9*).

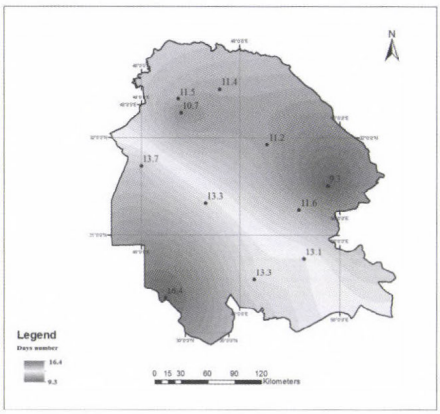

Fig. 8. Map of the persistence of a 3-day dry spell return period.

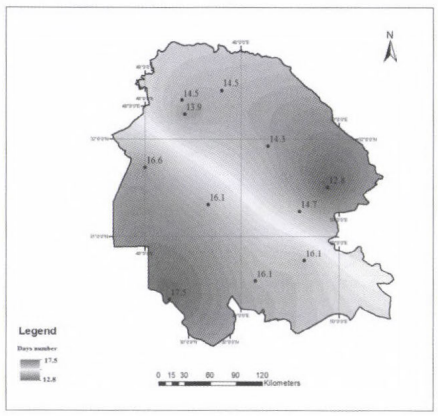

Fig. 9. Map of the persistence of a 5-day dry spell return period.

5.2. *Assessment of the relationship between the height and distribution of dry and wet spell lengths in days*

In order to assess the relationship between the height and distribution of consecutive dry days, simple linear regression was used. For this purpose, the elevation map of Khuzestan province was extracted using a 30-meter resolution satellite image (DEM) (*Fig. 10*). Then, using the Euclidean distance equation, 1200 elevation points were selected in Khuzestan province. Then, using kriging interpolation, the probabilities of lengths of dry spells in days for the 1200 selected points were extracted. The following regression equation was used to calculate the correlation ratio between the elevation and dry spell length in days:

$$y = 1E\text{-}07x^4 - 0.0001x^3 + 0.046x^2 - 7.146x + 377.88(12)\,, \qquad (14)$$

$$R^2 = 0.8394\,.$$

The results of the relation between the height and precipitation showed that, at a 99% confidence level, there is a strong correlation between these parameters. Based on this equation, correlation maps were drawn between elevation and dry spell lengths in days (*Fig. 11*). Exploration of this map indicated that the probability of dry days from the north to the south of the province is reduced. For wet spell lengths this situation is quite the contrary.

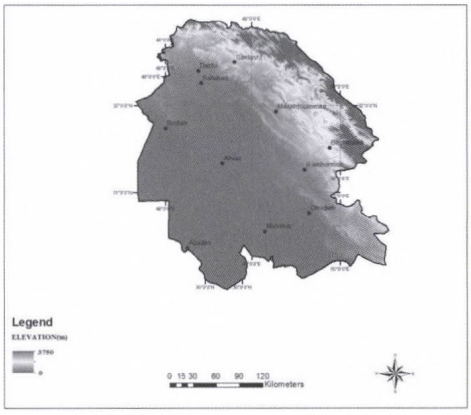

Fig 10. Elevation map of Khuzestan Province.

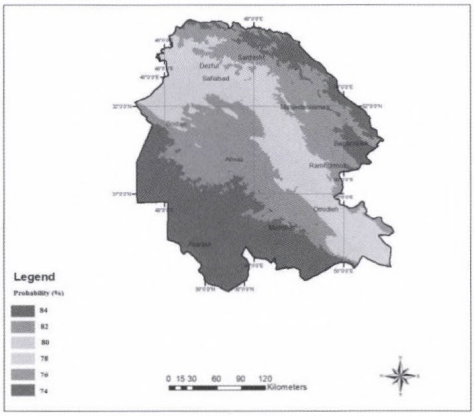

Fig. 11. Map of the relationship between the elevation and the length of dry spell.

5.3. Assessment of the relationship between the atmospheric circulation system and the probability of lengths of dry and wet spells in days

In order to assess the relationship between the atmospheric circulation patterns and the precipitation, the PI index was calculated and analyzed for 11 weather stations in the study area. This index specifies the conditional probability of rainfall in a circulation pattern. Results of PI, the role of each of the atmospheric circulation pattern showed the creation or lack of precipitation.

The results showed significant differences in the arrangement patterns of geopotential height of 500 hPa, sea level pressure, and circulation patterns in Iran. Analysis of atmospheric circulation systems showed three distinct patterns of rainfall in Iran.

5.4. Atmospheric circulation patterns for wet spell lengths

5.4.1. Pattern 1 (p1)

In Pattern 1, the 500 hPa geopotential height maps show a trough from northeastern Europe, to the southwest of Iraq. Because of the trough in the east, there is positive relative vorticity in this situation. Where there is sufficient moisture in the area, there is a chance of rain in this circulation pattern (*Fig. 12*-p1-A).

The map of the mean sea level pressure, the pressure of 1024 hPa, show deployment over Siberia. The pressure tabs stretch from the east-west to northwestern Europe. The low pressure from Saudi Arabia and North Africa in

the mid-latitudes extends to the East Mediterranean region. The results of the PI index indicated that this pattern has the greatest impact on the southwestern and western regions of Iran (Khuzestan province). The present pattern causes precipitation and wet events in much of the country (*Fig. 12*-p1-B and C).

5.4.2. Pattern 2 (p2)

The composite map of 500 hpa geopotential height indicated the presence of a trough over Russia that expands to the Mediterranean along the southwest (*Fig. 12*-p2-A). The trough from the southwest (Khuzestan province) entered Iran and caused a lot of rain in these areas. The PI in Khuzestan is relatively high (PI = 3), which indicates that this pattern causes wet periods (*Fig. 12*-p2-B and C).

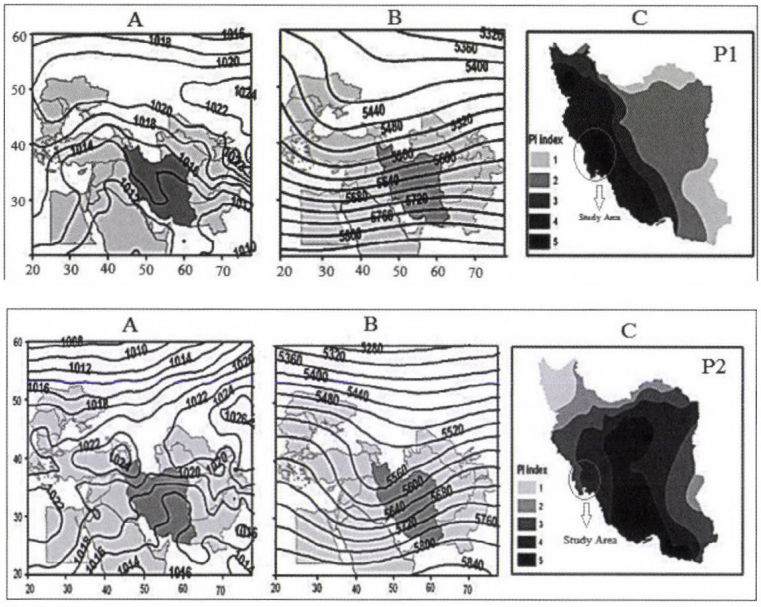

Fig. 12. Patterns of atmospheric circulation in Iran's Khuzestan province. A: 500 hPa mean geopotential height pattern ; B: mean sea level pressure pattern ;C: PI index pattern.

5.5. Atmospheric circulation patterns for dry spell lengths

5.5.1. Pattern 1 (p1)

The map of 500 hPa level showed a trough with a north-south direction expanding from the north of the Black Sea to the Red Sea. The eastern part of

the trough has affected the northern regions of Iran (*Fig. 13*-p1-A). In this pattern, high pressure (with a center of 1026 hPa) was seen over Siberia and Europe, and the 1020 hPa isobaric curves expanded on the Mediterranean, North Africa, and the southeast. Formation of this synoptic pattern caused drought in most parts of Iran (*Fig. 13*-p1-B). The PI Index calculation also shows that with the exception of the northwestern areas, the index rate is less than 1 in other parts of the country. This means that the implementation of this pattern in the study area causes dry conditions (*Fig. 13*-p1-C).

5.5.2. Pattern 2 (p2)

In this pattern, a trough over northwestern Europe and the eastern Mediterranean is located at the 500 hPa level. Most parts of Iran are dominated by high pressure (*Fig. 13*-p2-A), and atmospheric stability conditions prevail (*Fig. 13*-p2-B). The PI index calculation also showed that the index was less than 1 in most parts of the country and the province of Khuzestan, and dry conditions have occurred (*Fig. 13*-p2-c).

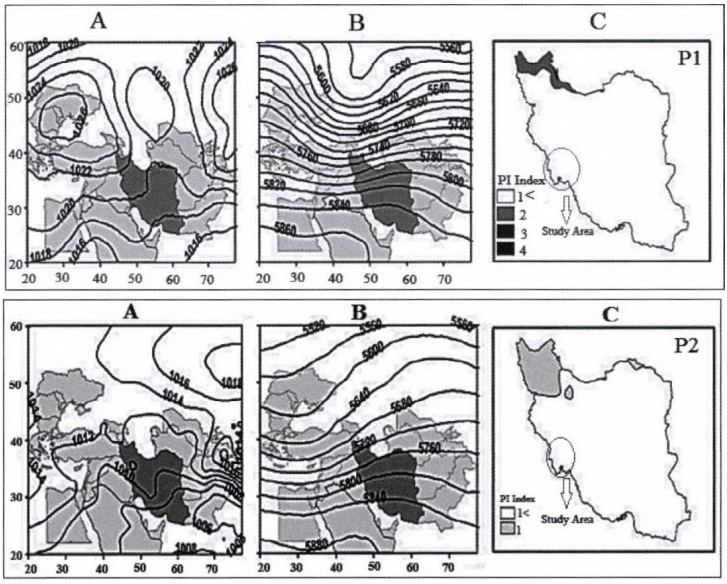

Fig. 13. Patterns of atmospheric circulation in Iran's Khuzestan province. A: 500 hPa mean geopotential height pattern ; B: mean sea level pressure pattern ;C: PI index pattern.

5.6. Evaluation of dry and wet periods

For the impact assessment of dry and wet periods in Khuzestan province, two sets of field data were used:

—data on groundwater levels in different parts of Khuzestan province,

—data on rainfed wheat yield in different parts of Khuzestan Province.

Data on groundwater levels and data relating to rainfed wheat yield were obtained from the Agricultural Research Center of Khuzestan Province. To evaluate the effects of dry days on water resources and agricultural products, 46 stations were selected. In order to evaluate the effect of the dry period, the water level and the correlation between these two parameters were studied, and linear regression and polynomial regression methods were used. The results of the correlation between the levels of the groundwater and the average probability of consecutive dry days in 46 selected stations showed that a significant, strong correlation exists between the mean probability of dry periods and the groundwater level. The degree of correlation is $R^2 = 0.93$ at a 99% confidence level (*Fig. 14*). This result shows that the groundwater is strongly influenced by dry periods.

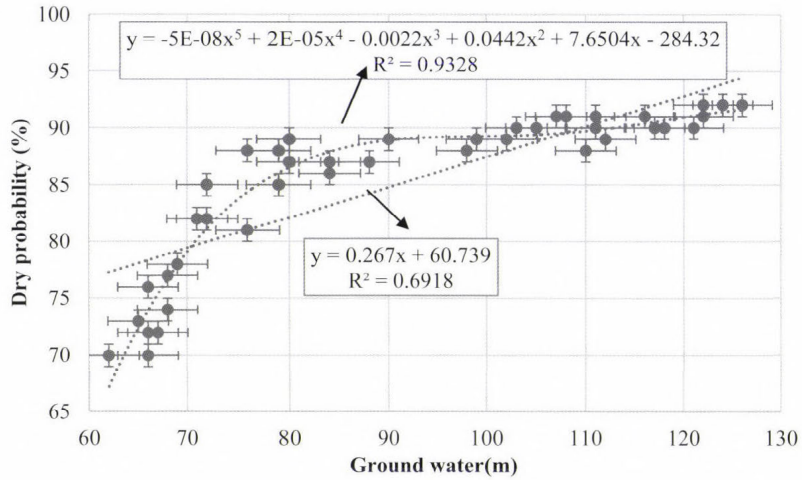

Fig. 14. Graph correlation between the average probability of dry periods and ground water levels.

In order to assess the impact of consecutive dry days on the yield of crops, rainfed wheat was selected, because it is the main crop of Khuzestan province, and its performance is subject to fluctuations in rainfall. The results of the regression relationship to calculate the average probability of dry days with an average annual yield of rainfed wheat in selected stations indicated the existence of a high correlation between these two parameters (at the 99% confidence level, $R^2 = 0.87$). Investigations showed that the yield of rainfed wheat is significantly reduced by increasing the probability of dry periods (*Fig. 15*).

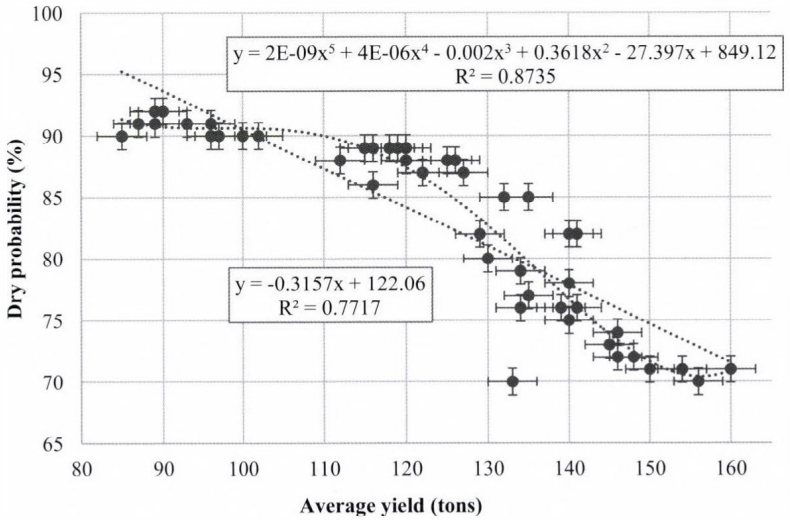

Fig. 15. Graph correlation between the average probability of dry periods and annual dryd wheat yield (tons).

6. Conclusions

The study of extreme precipitation events, such as floods and droughts, requires the analysis of wet and dry day sequences. The empirical frequency distribution does not provide a good insight into the probabilities of very long sequences of dry and wet spells, which are more important for practical purposes than short sequences. Statistical models give more reliable estimates. In this work, dry and wet spells were studied using the first-order Markov chain model. The daily precipitation data at 11 meteorological stations, being representative of different climate regimes in Khuzestan province, were analyzed. Wet or dry days were classified according to daily precipitation amounts of 1.0 mm.

Khuzestan province is one of the most important agricultural sectors with a variety of crops, and it plays an important role in supplying the needs of the country. This province is first in the country in cultivating cereals. Results of the current study showed that the probability of consecutive dry periods is high, in different parts of the province; moreover, water resources and agricultural performance are greatly affected by dry and wet periods, therefore, careful planning must be done in this area.

Results of the current study also indicate thaton the basis the generated sequences of wet and dry periods, the synoptic systems, and local factors (topography), four patterns were identified. Analysis of general circulation models of the atmosphere, and previous studies of this area by other researchers such as *Lashkari* (1996), *Alijani* (2002), *Hojatizadeh* (2002), and *Raziei et al.* (2008) confirm these conclusions. These patterns can predict extreme wet and dry periods.

References

Ababaei, B., Sohrabi, T.M., and *Mirzaei, F.*, 2012: Simulation of Rainfall Occurrence in Qazvin Synoptic Station Using Probability Models. *J. Nat. Geogr. Res. 79*, 111–122.

Alasseur, C., Husson, L., and *Perez-Fontan, F.,* 2004: Simulation of rain events time series with Markov model. Proc. of 15th IEEE International Symposium on Personal, Indoor and Mobile Radio Communications 4, 2801–2805.

Alijani, B., 2002: Variation of 500 hpa Flow Patterns Over Iran and Surrounding Areas and Their Relationship with Climate of Iran. *Theor. Appl. Climatol. 71*, 41–54.

Ana, A. and *Paulo, S.,* 2007: Prediction of SPI Drought class Transitions using Markov chain, *Water Resour. Manage. 21,* 1813–1827.

Anagnosropoulou, Chr., Maheras, P., Karakostas, T., and *Vafadis, M.*, 2003: Spatial and temporal Analysis of Dry Spell in Greece. *Theor. Appl. Climatol. 74*, 77–91.

Asakereh, H., 2009: A Study of the frequency and persistence of the possibility of rainy days in the city of Tabriz, using a Markov chain model. *Water Resour. Res.Iran. 2*, 46–56.

Bekele, E., 2002: Markov chain modeling and Enso influences on the rainfall seasons of Ethiopia. National Meteorological Services of Ethiopia. 25.

Berger, A. and *Goossens, C.*, 1983: Persistence of wet and dry spells at Uccle (Belgium). *J. Climatol. 3*. 21–34.

Chynlar, A., 2002: Introduction to Stochastic Processes, translated by Shahkar,G,H., BozorgNia,A,G., Tehran, Amirkabir University of Technology Institute of Scientific Publications.451.

Deni, S.M. and Jemain, A.A., 2008: Mixed log series geometric distribution for sequences of dry days. Atmos. Res. 92. 236–243.

Deka , S., Borah, M., and *Kakaty, S.C.* , 2010: Statistical modeling of wet and dry spell frequencies over North-East India. *J. Appl. Nat. Sci. 2*, 42–47.

*El Seed, A.G.,*1987: An application of Markov Chain Model for wet and dry spell probabilities at Juba in Southern Sudan.- *Geo J. Lib. 15*.420–424.

Fisher, B.M.C., Mul, M.L., and *Savenije, H.H.G.*, 2013: Determining spatial variability of dry spells: a Markov-based method, applied to the Makanya catchment, Tanzania. *Hydrol. Earth Syst. Sci. 17*, 2161–2170.

Hakimi-Pour, A., 1998: Application of the theory of Markov chain management decisions. Mashhad, Razavi Publications. 431.

Haggstrom, O., 2002: Finite Markov Chains and Algorithmic Applications. Cambridge University Press. 541.

Hojatizadeh, R., 2002: A Synoptic Investigation of Floods in Rivers of Western Zgros (With Emphasis on Karkheh, Karoon and Dez basins). Ph.D. Thesis. Supervisor Mohamad Reza Kaviani and Hassan Ghayour. Department of physical geography,University of Isfahan. Iran. 233.

Lashkari, H., 1996: The Synoptic Pattern of Heavy Precipitation Occurrences in Southwestern Iran. - Ph.D. Thesis, Supervisor Ghaemi,H., Department of physical geography, University of Tarbiat Modares, Iran.221.

Mathugama, S.C. and *Peiris, T.S.G.,* 2011: Critical Evaluation of Dry Spell Research. *Int. J. Basic Appl. Sci.. 11(6).*153–160.

Nadi, M., Jamei, M., Bazrafshan, J., and *Jannat Rostami, S.*, 2012: Evaluation of Different Methods for Interpolation of Mean Monthly and Annual Precipitation Data (Case Study: Khuzestan Province). *Phys. Geogr. Res. Quart. 44(4).* 117-130.

Nobolis, F., 1986: Dry spells in the Alpine country Austria. *J. Hydrol. 8,* 235–251.

Raziei, T., Mofidi, A., and *Zarrin, A.,* 2008:The 500 hPa Centers of Action and Atmospheric Circulation Patterns over Middle East and their Relationship with Precipitation in Iran.- *Iranian J. Earth Space Phys. 35.* 121–141.

Todorovic, P. and *Woolhiser, D,A.,* 1974: A statistic model of n-day Precipitation. *J. Appl. Meteorol. 14.* 17–24.

Zarei, H. and *Sahkar, G.H.,* 2002: Review the possibility of frequency of rainy days and dry areas Khoramdeh - Arak Zeshk. - The third seminar Probability and Stochastic Processes. University of Isfahan, 7 and 8. *134-142.*

Zhang, X., 1995: Regional climatic variability and climate change scenarios" Ph. D. Dissertation university of Lisbon.135.

IDŐJÁRÁS

Quarterly Journal of the Hungarian Meteorological Service
Vol. 119, No. 4, October – December, 2015, pp. 493–514

Mann–Kendall trend analysis of surface air temperatures and rainfall in Iraq

El-Sayed M. Robaa [1*] and **Zhian Al-Barazanji** [2]

[1] *Astronomy, Space Science and Meteorology Department, Faculty of Science, Cairo University, P.O. Box 12613, Giza, Egypt*
E-mail: d_robaa@hotmail.com
[2] *Department of Atmospheric Science, Faculty of Science, Al-Mustansiriyah University, Baghdad, Iraq*
E-mail: zhdilshad@gmail.com

** Corresponding author*

(Manuscript received in final form March 20, 2015)

Abstract—In this study, trends of the seasonal and annual maximum (T_{max}), minimum (T_{min}), and mean (T) air temperatures, as well as rainfall amounts (R_a) time series were investigated for eleven stations in Iraq for the period 1972–2011 (40 years). Four statistical tests including homogeneity, Mann–Kendall (MK), Sen's slope estimator and linear regression were used for the analysis. The results revealed that annual mean of T_{max}, T_{min}, and T time series showed statistically significant increasing trends over 81.8, 100, and 100% of the stations at the 0.001 level and they experienced an increase of 0.50, 0.67, and 0.58 °C/decade, respectively; while the annual rainfall has shown decreasing trends at 90.9% of the stations and it experienced a decrease of –20.50 mm/decade. Seasonally, the highest increase of T_{max}, T_{min}, and T values have been found over the extreme south of the country during summer at the rates of 1.47, 1.06, and 1.16 °C/decade, respectively, while the highest decrease of R_a values has been found in the northern part of the country during winter at the rate of –36.35 mm/decade.

Key-words: climate change, air temperature, rainfall, Mann-Kendall test, trends, Iraq

1. Introduction

The detection and attribution of global climate change resulting from anthropogenic activities are one of the main themes of current climatological research. Several studies of long-term time series of temperatures have been done on global scale (*Jones,* 1994; *Nicholls et al.,* 1996; *Watson et al.*, 1998; Jones *et al.*,1999; *Folland et al.,* 2001; *Eichner et al.,* 2003; *Rybski et al.*, 2006; *Efstathiou et al.,* 2011; *Varotsos et al.*, 2013) and regional scale (*Marco et al.,* 2003; *Arora et al.,* 2005; *Smadi*, 2006; *Chen et al.*, 2007; *Rebetez* and *Reinhard*, 2008; *Busuioc et al.*, 2010; *Tabari* and *Talaee*, 2011a; *Stephenson, et al.*, 2014). The main finding of the results have shown that the Earth's surface air temperature has increased by 0.6 °C – 0.8 °C during the 20th century. The increasing of the air temperature proved to be nonlinear and non-homogenous at global scale (*Croitoru et al.*, 2012). Associated with global warming, there are strong indications that rainfall changes are already taking place on both global (*Diaz et al.*, 1989; *Hulme et al.*, 1998; *Lambert et al.*, 2003; *Dore*, 2005) and regional scales (*Yu* and *Neil*, 1993*; Gemmer et al.*, 2004; *Smadi* and *Zghoul*, 2006; *Kayano* and *Sansıgolo,* 2008; *Busuioc et al.*, 2010; *Tannecia et al.*, 2014). There have not been any internationally published works on surface air temperature and rainfall changes over the past century in Iraq. The detailed analysis and understanding of trends of climate events in Iraq are important to reduce the climate-induced dryness and the impact of temperature extremes on society, agriculture and environment. Therefore, this study was carried out for analysing the seasonal and annual trends in mean maximum, minimum, and mean air temperatures, as well as rainfall amounts. The Mann-Kendall test, the Sen's slope estimator, and the linear regression in Iraq from 1972 to 2011 were used.

2. Study area and data

Iraq is located in southwest Asia between latitudes $29°5' - 37°22'$ N and longitudes $38°45' - 48°45'$ E. The surface of Iraq is 438,317 km^2 (*Fig. 1*). Topographically, Iraq is shaped like a basin, consisting of the Great Mesopotamian alluvial plain of the Tigris and Euphrates rivers. This plain is surrounded by mountains in the north and east, which can reach altitudes of 3611 m above sea level, and by desert areas in the south and west, which account for over 40 percent of the land area. Iraq is characterized by four distinct topographic features:

a. Mesopotamian plain. This alluvial plain occupies a quarter of the area of Iraq.

b. Desert plateau. This area is located in the west of Iraq and occupies about less than half of Iraq.

c. Mountainous region. This region is located in the northern and north-eastern part of Iraq.

d. Hilly region. This is a transition zone between the low-lying Mesopotamian plain in the south and the high mountains in the far north and north-eastern part of Iraq.

Diverse topography of Iraq plays an essential role in its climate. Being situated in the north part of the subtropical region, Iraq is characterized by relatively low winter temperature, dry and hot summer, and two short transitorial seasons (spring and autumn). It seems that the differences in temperature have great impacts on Iraq's extreme climate. Iraq lies within the northern temperate zone, but the climate is continental and subtropical. Winters are usually cool to cold, with an average daily temperature that might reach 16 °C dropping at night to 2 °C. Summers are dry and hot to extremely hot, with a temperature of over 43 °C during July and August, yet dropping at night to 26 °C (*Al-Ansari et al.,* 2013). The rainfall in Iraq is tracking the climate of the Mediterranean Sea. Most amount of rainfall falls during the seasons of winter, spring, and autumn, while summer is rainless. Average annual rainfall is 154 mm, and it ranges from less than 100 mm over 60% of the country in the south up to 1200 mm in the north-east (*Al-Ansari et al.,* 2013; *Al-Ansari* and *Knutsson*, 2011).

Climatic data were available over the 40-year period from 1972 until 2011 at eleven stations. The monthly mean daily values of measured mean minimum air temperature, T_{min} (°C), mean maximum air temperature, T_{max} (°C), mean air temperature T (°C), and total rainfall amount R_a (mm) at the eleven selected stations have been taken from the Iraq Meteorological Authority (IMA). The stations have been chosen based on data availability and to cover the whole area of Iraq. Site of each station has remained the same, with almost negligible change since the beginning of the data records. The selected stations and their geographical coordinates as well as the observation periods of temperature and rainfall are given in *Table 1* and *Fig. 1*. Three statistical techniques were used in this research: a homogeneity test, the widely used non-parametric Mann–Kendall test, and Sen's slope estimator. The homogeneity test of the data series was carried out by applying the Abbe-test (*Schoenwiese*, 1992; *Schaefer*, 1996). All data series were shown to be homogeneous at all stations. To estimate the slope of an existing trend, the Sen's nonparametric method (*Sen*, 1968) was also used. Whether or not a constant increasing or decreasing trend was occurring, the MK (*Kendall*, 1938, *Mann*, 1945, *Kendall*, 1975; *Zhang et al.*, 2001) test for trend was also applied. In this test, the significance levels are 0.001, 0.01, 0.05, and 0.1 (*Salmi et al.*, 2002, *Luo et al.*, 2008), from very high significance to non-significance. SPSS and Excel programs were used to analyze temporal and

spatial temperature and rainfall changes. The Excel template MAKESENS (*Salmi et al.*, 2002) was also used to detect trends by the MK test.

Table 1. List of the eleven meteorological stations in Iraq, their geographical coordinates, as well as the observation periods of the air temperature and rainfall at each station.

Stations	Latitude (N)	Longitude (E)	Elevation (m) above M.S.L	Observation period for air temperatures and rainfall
Mosul	36° 19′	43° 07′	223	1972–2011
Sulaymaniya	35° 32′	45° 26′	884.8	1972–2011
Kirkuk	35° 28′	44° 23′	330.8	1972–2011
Khanaqin	34° 16′	45° 17′	202	1972–2011
Baghdad	33° 19′	44° 25′	31.7	1972–2011
Rutba	33° 02′	40° 17′	630.8	1972–2011
Al-Hai	32° 01′	46° 02′	17	1972–2011
Diwaniya	31° 59′	44° 59′	20	1972–2011
Samawa	31° 19′	45° 17′	6	1972–2011
Nasiriya	31° 03′	46° 14′	5	1972–2011
Basra	30° 30′	47° 50′	2.4	1972–2011

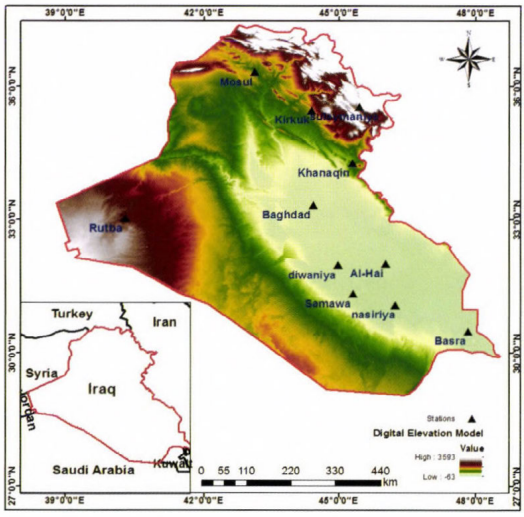

Fig. 1. Map of Iraq including the eleven selected stations.

3. Results and discussion

3.1. Trends of mean maximum temperature

Fig. 2 illustrates the annual anomalies of mean maximum temperature (T_{max}, °C) at the eleven selected stations in Iraq. Statistical properties of the seasonal and annual T_{max} series were tested and presented in *Table 2*. In winter, it can be clearly seen that 63.6, 27.3, and 9.1% of stations have experienced significant positive trend at the 0.01, 0.05, and 0.1 levels, respectively. According to the MK test. The trends range from 0.42 °C/decade at Basra in the south (significant at the 0.05 level) to 0.75 °C/decade at Sulaymaniya in the north (significant at the 0.01 level) (*Figs. 2.* and *6* and *Table 2*).

In spring, significant positive trends are observed for all stations (except Samawa, which has non-significant trend). It was found that 45.4, 27.3, and 18.2% of the stations have experienced significant positive trend at the 0.001, 0.01, and 0.1 levels, respectively, while the trends are not significant at only 9.1% of the stations. Trends ranged between 0.20 °C/decade at Samawa and 0.86 °C/decade at Khanaqin; the trend for Khanaqin is significant at the 0.001 level, while it is not significant for Samawa. During summer, all stations showed strong evidence of significant positive trend (except Kirkuk station which has non-significant trend). It can be seen that 45.4 and 45.5% of the stations have experienced significant positive trend at the 0.001 and 0.01 levels respectively, while the trends are not significant at only 9.1% of the stations. The trends range from 0.15 °C/decade (non-significant trend) at Kirkuk to 1.47 °C/decade (significant at the 0.001 level) at Basra (*Figs. 2* and *6* and *Table 2*).

On the contrary, negative and non-significant positive trend patterns dominated during autumn (*Table 2*). It can be seen that 9.1 and 9.1% of the stations have experienced significant positive trend at the 0.01 and 0.1 levels, respectively, while the trends are not significant at 72.7% of the stations. The trends range from –0.02 °C/decade at Diwaniya (non-significant trend) to 0.5 °C/decade at Basra (significant at the 0.05 level). From the beginning of 1972 until 1995, a cooling pattern was found at all stations, while subsequently warming pattern was identified until the end of the study period, and the change is statistically significant. The annual and seasonal trend analyses reveal that most warming in reference to T_{max} was observed in both winter (0.56 °C/decade) and spring (0.55 °C/decade), while the average trend over the whole country of Iraq was found to be 0.50 °C/decade. Annually, it was found that 81.8, 9.1, and 9.1% of the stations have experienced significant positive trend at the 0.001, 0.01 and 0.05 levels, respectively (*Figs. 2* and *6* and *Table 2*).

Table 2. Trends of maximum (T_{max}), minimum (T_{min}) and mean (T) temperatures (°C/decade), by Mann-Kendall Sen's test

Station	Element	Winter	Spring	Summer	Autumn	Annual
Mosul	T_{max}	0.53^{**}	0.43^{+}	0.33^{**}	0.25^{-}	0.36^{***}
	T_{min}	0.13^{-}	0.29^{+}	0.45^{***}	0.53^{**}	0.37^{***}
	T	0.30^{+}	0.39^{*}	0.38^{***}	0.47^{*}	0.36^{***}
Sulaymaniya	T_{max}	0.75^{**}	0.50^{**}	0.40^{**}	0.18^{-}	0.59^{***}
	T_{min}	0.75^{***}	0.59^{***}	0.64^{***}	0.41^{*}	0.62^{***}
	T	0.71^{***}	0.58^{**}	0.58^{***}	0.36^{*}	0.61^{***}
Kirkuk	T_{max}	0.48^{*}	0.42^{+}	0.15^{-}	0.01^{-}	0.26^{*}
	T_{min}	0.39^{**}	0.55^{***}	0.80^{***}	0.28^{-}	0.56^{***}
	T	0.44^{**}	0.51^{**}	0.56^{***}	0.17^{-}	0.43^{***}
Khanaqin	T_{max}	0.61^{**}	0.86^{***}	0.65^{***}	0.20^{-}	0.68^{***}
	T_{min}	0.39^{*}	0.91^{***}	1.04^{***}	0.83^{***}	0.81^{***}
	T	0.62^{**}	0.88^{***}	0.85^{***}	0.56^{***}	0.74^{***}
Baghdad	T_{max}	0.69^{**}	0.42^{**}	0.36^{**}	0.16^{-}	0.45^{***}
	T_{min}	0.57^{***}	0.78^{***}	1.06^{***}	0.72^{**}	0.79^{***}
	T	0.55^{**}	0.64^{***}	0.74^{***}	0.46^{**}	0.64^{***}
Rutba	T_{max}	0.49^{*}	0.41^{**}	0.48^{***}	0.18^{-}	0.44^{***}
	T_{min}	0.48^{**}	0.79^{***}	0.92^{***}	0.82^{***}	0.77^{***}
	T	0.51^{**}	0.66^{***}	0.69^{***}	0.57^{**}	0.58^{***}
Al - Hai	T_{max}	0.65^{**}	0.68^{***}	0.53^{***}	0.22^{-}	0.55^{***}
	T_{min}	0.67^{***}	1.03^{***}	0.97^{***}	0.65^{***}	0.86^{***}
	T	0.65^{***}	0.95^{***}	0.71^{***}	0.47^{**}	0.73^{***}
Diwaniya	T_{max}	0.57^{**}	0.50^{***}	0.35^{**}	-0.02^{-}	0.41^{***}
	T_{min}	0.63^{***}	0.71^{***}	1.00^{***}	0.87^{***}	0.84^{***}
	T	0.55^{**}	0.66^{***}	0.69^{***}	0.48^{**}	0.61^{***}
Samawa	T_{max}	0.43^{+}	0.20^{-}	0.34^{**}	0.08^{-}	0.30^{**}
	T_{min}	0.14^{-}	0.47^{***}	0.42^{**}	0.44^{*}	0.39^{***}
	T	0.34^{+}	0.35^{**}	0.36^{**}	0.25^{-}	0.31^{***}
Nasiriya	T_{max}	0.54^{**}	0.73^{***}	0.68^{***}	0.33^{+}	0.62^{***}
	T_{min}	0.36^{**}	0.79^{***}	0.82^{***}	0.50^{***}	0.63^{***}
	T	0.46^{**}	0.78^{***}	0.79^{***}	0.46^{**}	0.61^{***}
Basra	T_{max}	0.42^{*}	0.85^{***}	1.47^{***}	0.50^{**}	0.83^{***}
	T_{min}	0.37^{*}	0.85^{***}	0.86^{***}	0.72^{***}	0.71^{***}
	T	0.37^{*}	0.81^{***}	1.16^{***}	0.61^{***}	0.77^{***}
Average	$\boldsymbol{T_{max}}$	**0.56**	**0.55**	**0.52**	**0.19**	**0.50**
	$\boldsymbol{T_{min}}$	**0.44**	**0.71**	**0.82**	**0.62**	**0.67**
	$\boldsymbol{T}$	**0.50**	**0.66**	**0.68**	**0.44**	**0.58**

The significance levels tested are 0.001 (***), 0.01 (**), 0.05 (*), 0.1 (+), and >0.1 (–) (*Salmi et al.*, 2002).

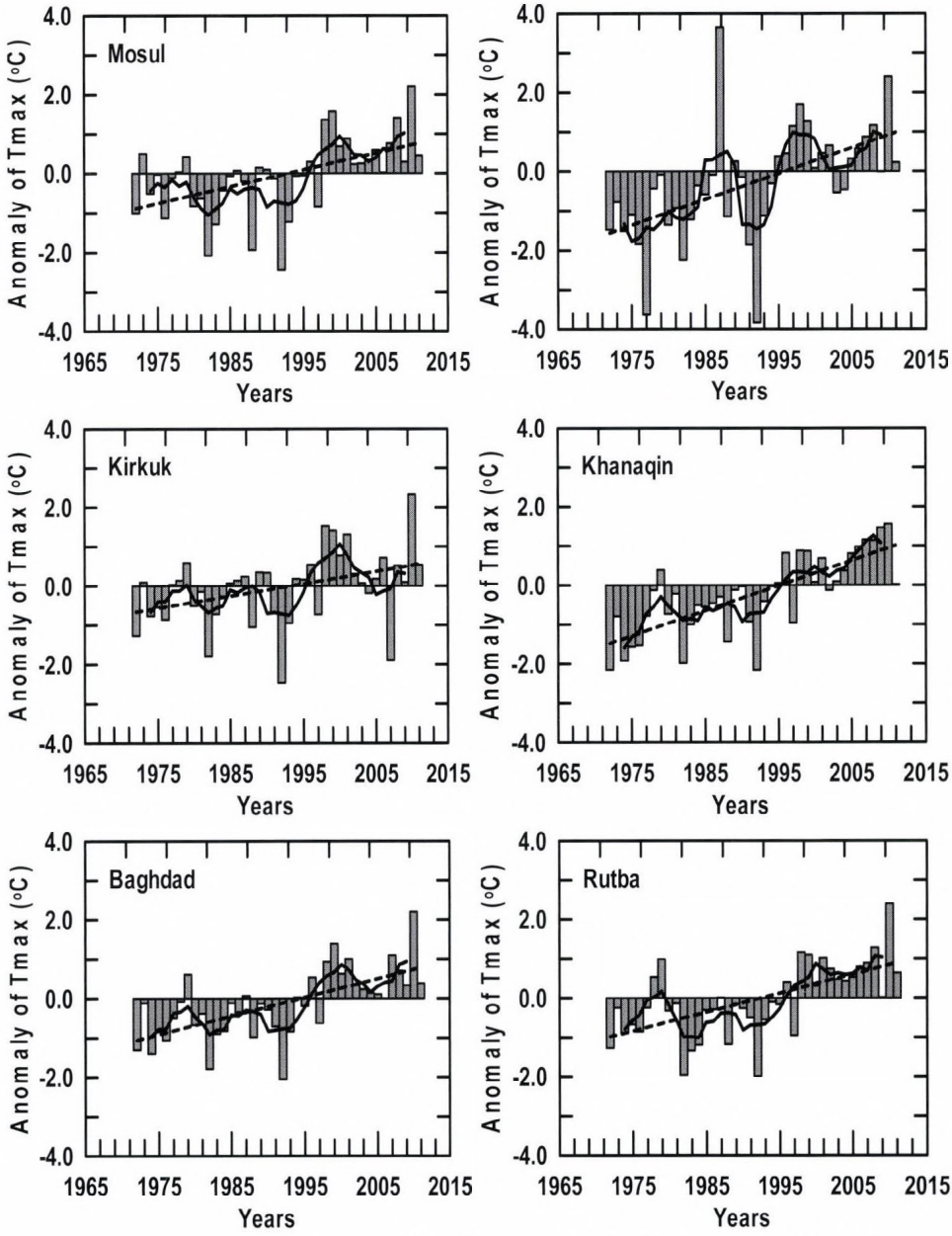

Fig. 2. Anomalies of maximum temperatures (T_{max} °C) for the eleven selected stations during the studied period (1972–2011), for the baseline (1982–2011) average. The bars indicate the anomalies of the years, the zigzag line represents five-year means, and the straight line indicates the long-term linear trends.

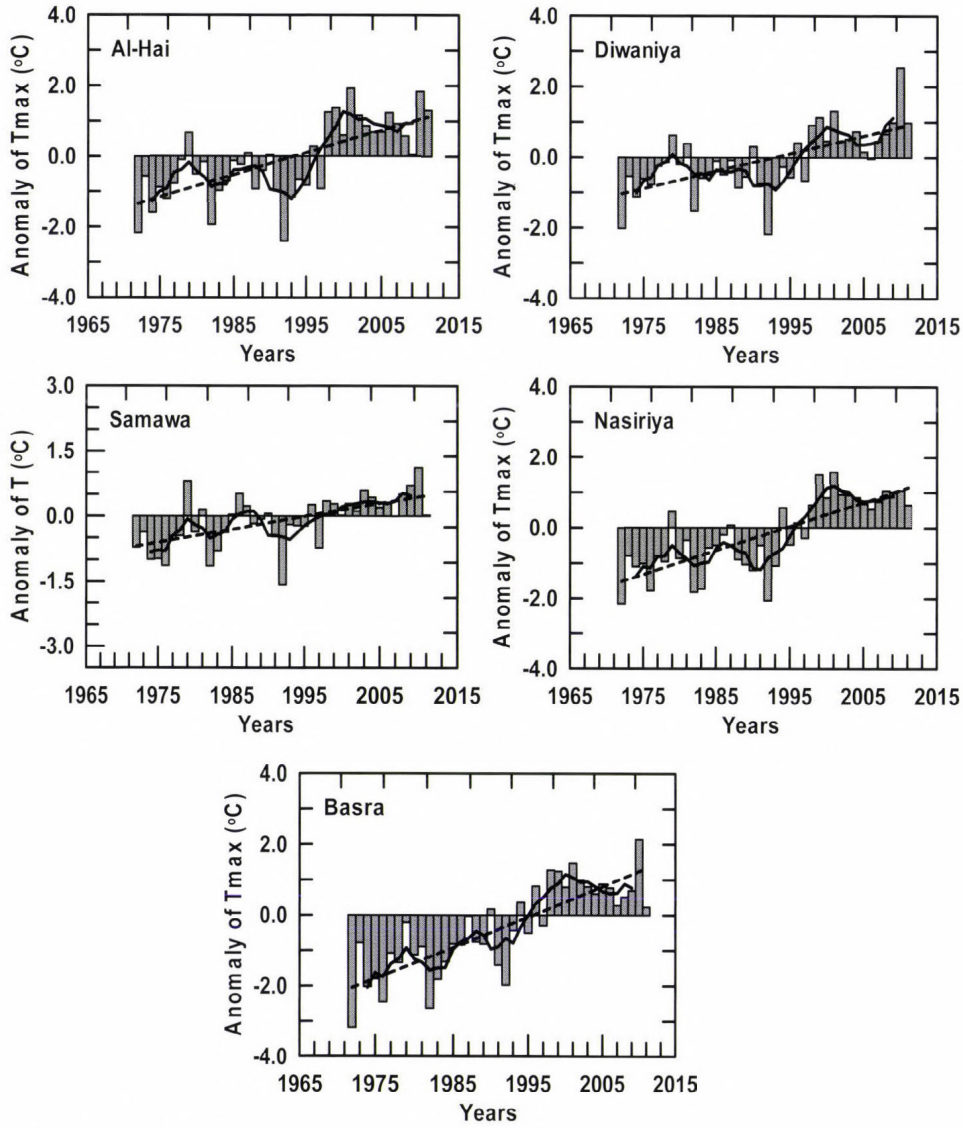

Fig. 2. (Continued).

In spring and summer, the significant positive trends of T_{max} are clearly observed with vider spatial distribution than winter and autumn. The strongest significant positive (1.47 °C/decade) and negative (–0.02 °C/decade) trends occurred in summer and autumn and reported at Basra and Diwaniya, respectively (*Fig. 6* and *Table 2*). It is clear that the long-term changes in

maximum temperature during winter, spring, and summer showed an increasing trend, which is statistically significant for the four last decades, while the autumn showed different pattern.

3.2. Trends of mean minimum temperature

Fig. 3 illustrates the annual anomalies of minimum temperature (T_{min}, °C) at the eleven selected stations in Iraq. Statistical properties of the seasonal and annual T_{min} series were tested using the Mann-Kendall test and presented in *Table 2*. It is clearly seen that all stations have experienced significant positive trend during winter, except for the two stations of Mosul and Samawa. It was found ,that 36.4, 27.3, and 18.2% of the stations have experienced significant positive trend during winter at the 0.001, 0.01, and 0.05 levels, respectively, while the trends are not significant at only 18.2% of the stations. The trends range from 0.13 °C/decade (non-significant trend) at Mosul to 0.75 °C/decade (significant at the 0.001 level) at Sulaymaniya. In spring, all stations have experienced significant positive trend. It was found that 90.9 and 9.1% of the stations had experienced significant positive trend at the 0.001 and 0.1 levels, respectively. Al-Hai, which is located in the southern part of the country, has experienced the highest positive trend (1.03 °C/decade), while Mosul in the northern part has experienced the lowest positive trend (0.29 °C/decade). Negative trends were not observed at the stations during this season. In summer, the trends were positive and significant at the 0.001 and 0.01 levels for 90.9 and 9.1% of the stations, respectively. It was found, that the trend values ranged between the lowest positive trend (0.42 °C/decade) at Kirkuk in the north to the highest positive trend (1.06 °C/decade) at Basra in the extreme south. In autumn, all stations have experienced significant positive trend (except Kirkuk). The trends range from 0.28 °C/decade (non-significant trend) at Kirkuk to 0.87 °C/decade (significant at the 0.001 level) at Diwaniya. It could be noticed, that 54.5, 18.2, and 18.2% of the stations have experienced significant positive trend during autumn at the 0.001, 0.01, and 0.05 levels, respectively, while the trends are not significant at only 9.1% of stations (*Figs. 3* and *6* and *Table 2*).

There is a general tendency for the warming trend during the study period. The annual and seasonal trend analyses reveal that most of the warming in reference to T_{min} was found in spring (0.71 °C/decade) and summer (0.82 °C/decade), respectively, while the average trend over the whole Iraq country is 0.67 °C/decade. Annually, it could be noticed that minimum temperature showed a significant positive trend in 100% of the stations at the 0.001 level, while there is not any stations in the whole Iraq which have significant/non-significant negative trend (*Figs. 3* and *6* and *Table 2*).

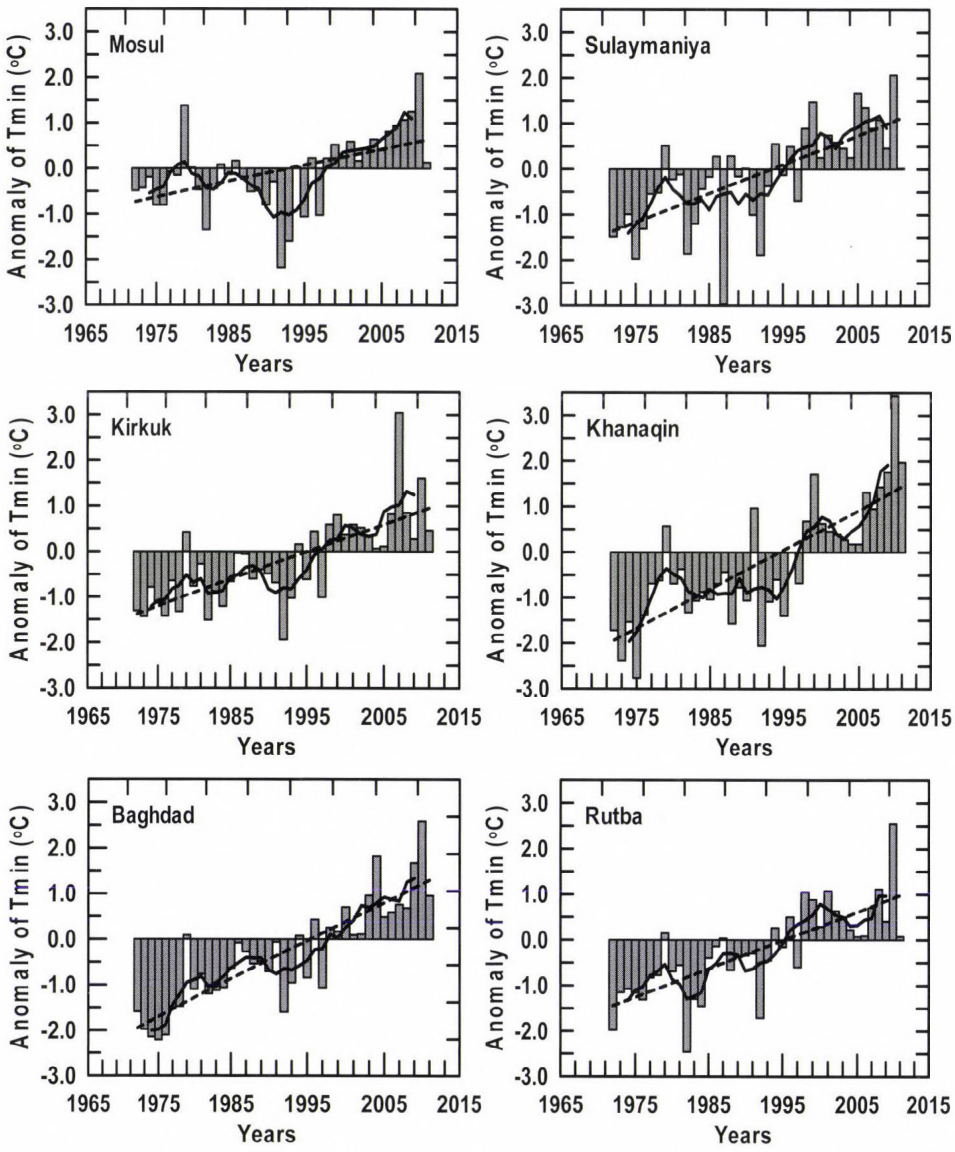

Fig. 3. Anomalies of minimum temperatures (T_{min}, °C) for the eleven selected stations during the studied period (1972–2011), for the baseline (1982–2011) average. The bars indicate the anomalies of the years, the zigzag line represents five-year means, and the straight line indicates the long-term linear trends.

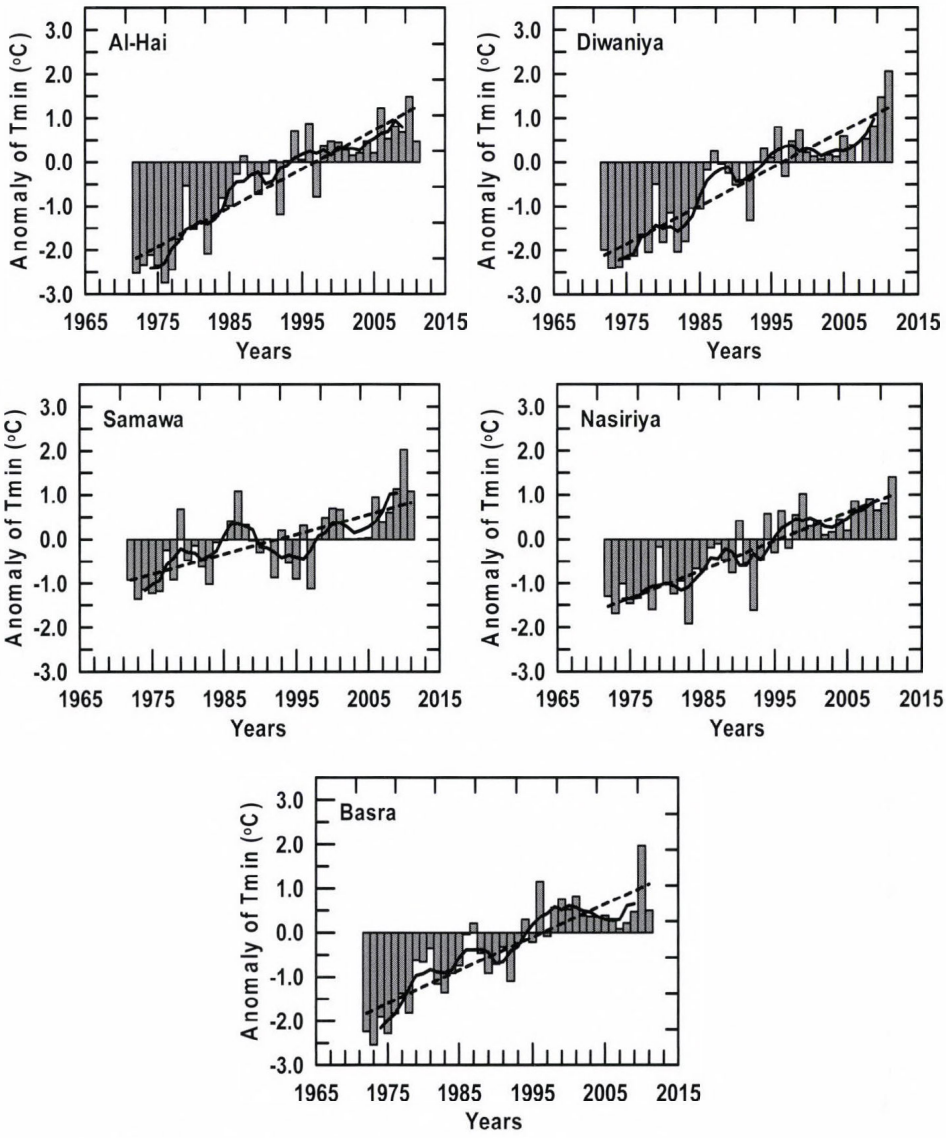

Fig. 3. (Continued).

3.3. Trends of mean temperature

Fig. 4 illustrates the annual anomalies of mean temperature (T, °C) at the eleven selected stations in Iraq. Statistical properties of the seasonal and annual T series were also tested and presented in *Table 2*. It was found, that according to the MK test for trend, all stations have experienced significant positive trends (warming pattern) of the annual mean temperature.

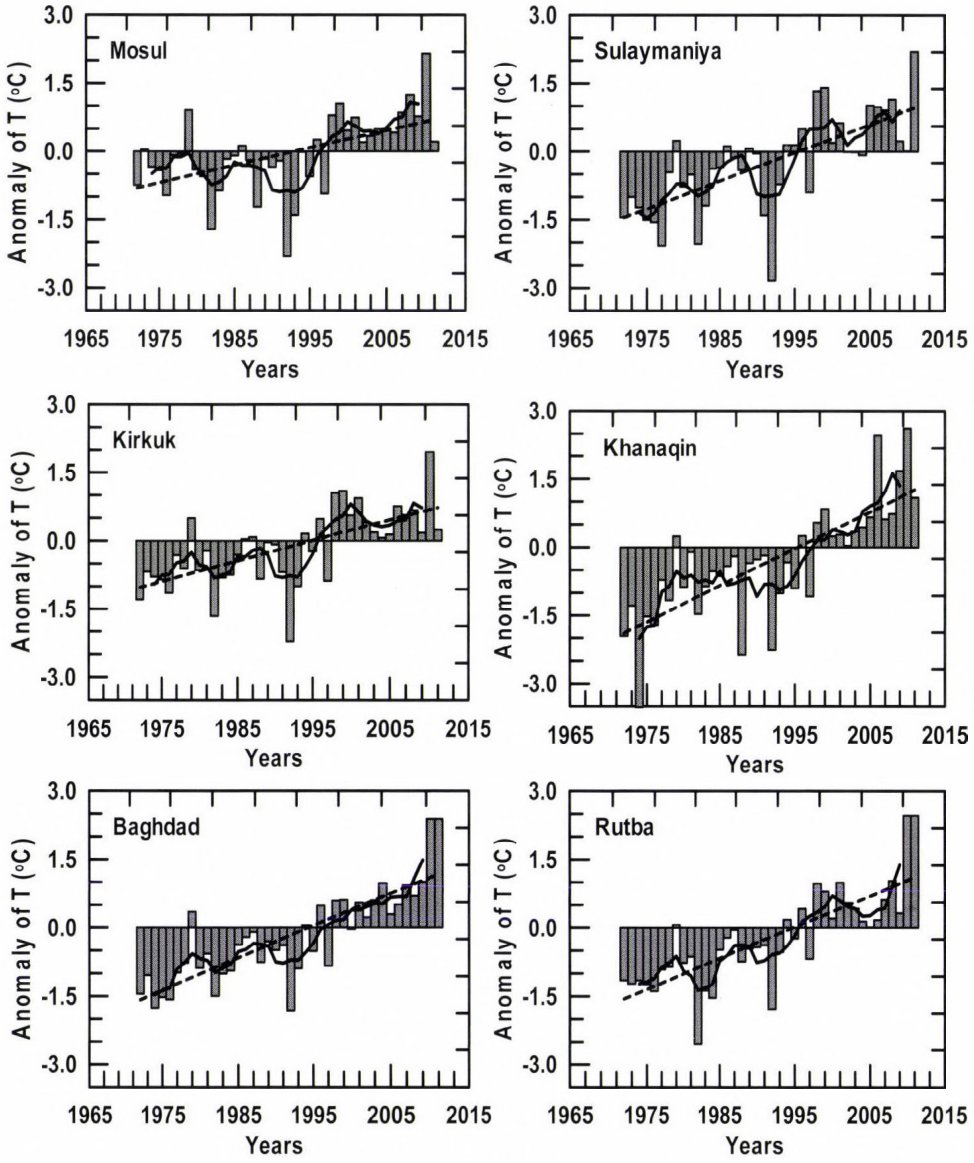

Fig. 4. Anomalies of mean temperatures (T, °C) for the eleven selected stations during the studied period (1972–2011), for the baseline (1982–2011) average. The bars indicate the anomalies of the years, the zigzag line represents five-year means, and the straight line indicates the long-term linear trends.

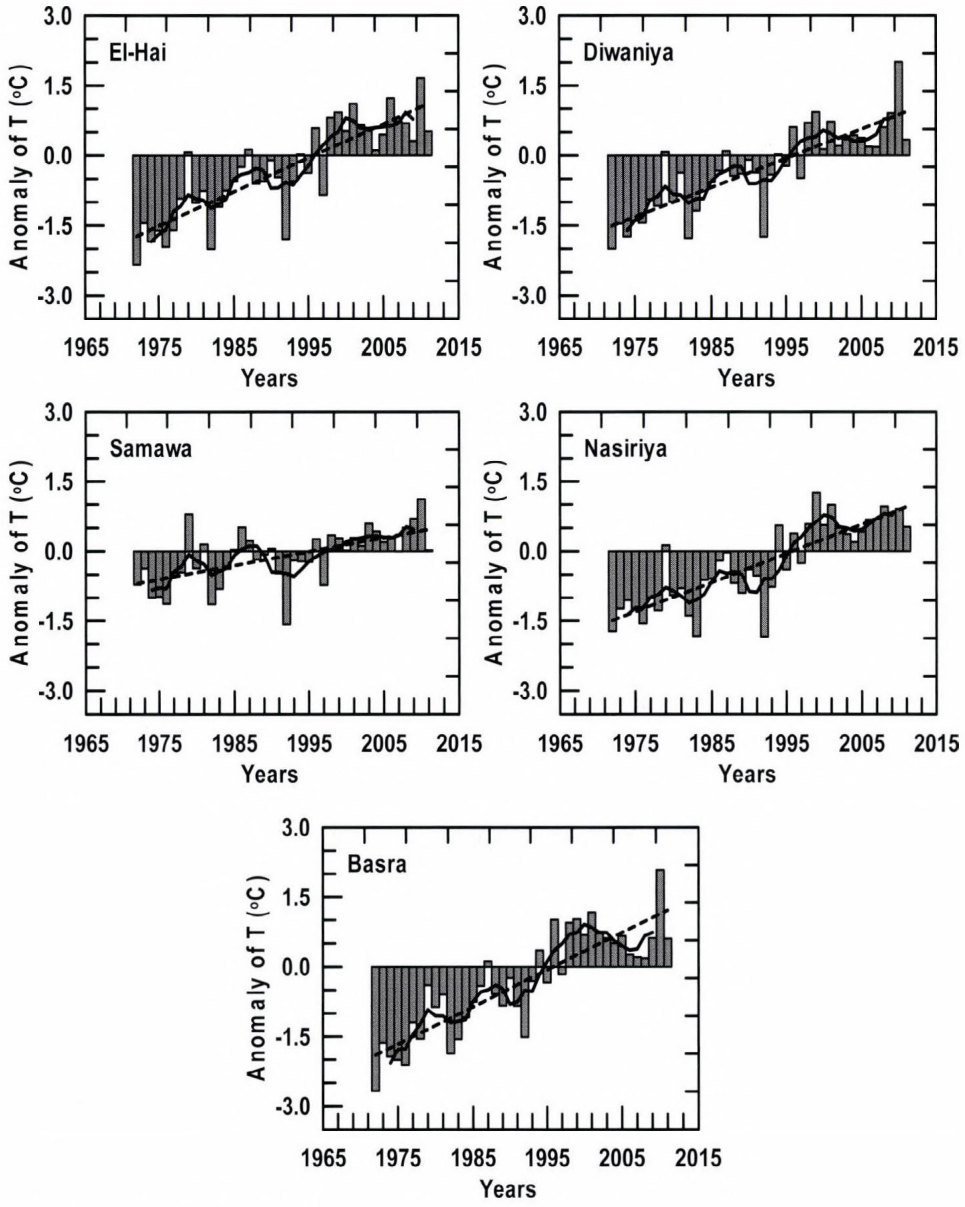

Fig. 4. (Continued).

In winter, all stations have experienced positive trend. It was found that 18.2, 54.5, 9.1, and 18.2% of the stations have experienced positive trend during winter at the 0.001, 0.01, 0.05, and 0.1 levels, respectively. Also, it can be noticed, that Mosul has the lowest and non-significant positive trend

(0.30 °C /decade), while Sulaymaniya has the highest significant positive trend (0.71 °C /decade) at the 0.001 level. During spring, ten stations show strong upward tendency trends, whereas 90.9% of the stations have experienced significant positive trend at the 0.001 level while 9.1% of the stations have positive trend at the 0.1 levels. It could be noticed, that the trends ranged between 0.35 °C/decade at Samawa and 0.95 °C/decade at Al-Hai; the trends for Samawa and Al-Hai are significant at the 0.01 and 0.001 levels, respectively (*Figs. 4* and *6* and *Table 2*).

All eleven stations also showed strong evidence of a significant positive trend during summer, while there is not any station with negative trend during this season. It could be noticed, that 90.9 and 9.1% of the stations have experienced strong significant positive trend at the 0.001 and 0.01 levels, respectively. Trends range between 0.36 °C/decade at Samawa and 1.16 °C/decade at Basra, and they are significant at the 0.01 and 0.001 levels, respectively. In autumn, the significant positive trend could be generally identified at all stations except for Kirkuk (0.17 °C/decade) and Samawa (0.25 °C/decade), which have non-significant trends, while Basra has the highest significant positive trend (0.61 °C/decade) at the significance level of 0.001. It was found that 18.2, 45.5, and 18.2% of the stations have experienced strong significant positive trend at the 0.001, 0.01, and 0.05 levels, respectively, and the trend is not significant at only 18.2% of the stations. Seasonally, there is not any stations in the whole Iraq which have significant/non-significant negative trend (*Figs. 4* and *6* and *Table 2*).

Annually, it is noticed that the mean temperature showed a significant positive trend at the 0.001 level for all stations, while there is not any stations in the whole Iraq which have significant/non-significant negative trend in the whole Iraq. It was also found, that the significant positive trends of T varied between the lowest value (0.31 °C/decade) at Samawa and the highest value (0.77 °C/decade) at Basra; the trends for both Samawa and Basra are significant at the 0.001 level (*Fig. 6* and *Table 2*).

The results are generally in agreement with those in many studies worldwide, which have shown a trend of increasing air temperature (*Jones* and *Moberg,* 2003; *Luterbacher et al.,* 2004; *Rebetez* and *Reinhard,* 2008; European Environment Agency reports (EEA), 2008; *Croitoru et al.*, 2012; *Piticar* and *Ristoiu*, 2012; *Ionita et al.*, 2013; *Croitoru* and *Piticar*, 2013; *Tannecia et al.*, 2014).

3.4. Trends of total rainfall

Total rainfall (R_a, mm), is the other important climate parameter in the present study. Statistical properties of the seasonal and annual R_a series at the eleven selected stations in Iraq were tested using the MK test and presented in *Table 3* and illustrated by *Fig. 5*.

Table 3. Trends of total rainfall amounts, Ra (mm/decade), by Mann- Kendall Sen's test

Station	Winter	Spring	Summer	Autumn	Annual
Mosul	−23.50^{+}	−3.45^{-}	0.00^{-}	−1.53^{-}	−32.25*
Sulaymaniya	−24.00^{-}	−3.50^{-}	0.00^{-}	0.39^{-}	−35.52^{-}
Kirkuk	−20.95^{-}	−7.69^{-}	0.00^{-}	−1.32^{-}	−36.06*
Khanaqin	−36.35**	−4.83^{-}	0.00^{-}	2.31^{-}	−41.96***
Baghdad	−9.85^{+}	0.65^{-}	0.00^{-}	0.51^{-}	−12.10*
Rutba	−11.75**	−2.29^{-}	0.00^{-}	0.47^{-}	−9.38^{-}
Al – Hai	−12.87^{+}	−0.91^{-}	0.00^{-}	−1.41^{-}	−24.72**
Diwaniya	−8.69^{+}	−0.61^{-}	0.00^{-}	1.81^{-}	−10.13^{-}
Samawa	−4.40^{-}	0.68^{-}	0.00^{-}	2.00^{-}	0.26^{-}
Nasiriya	−10.68^{+}	0.52^{-}	0.00^{-}	−0.04^{-}	−7.83^{-}
Basra	−7.27^{-}	0.67^{-}	0.00^{-}	0.29^{-}	−15.77*
Average	**−15.48**	**−1.89**	**0.00**	**0.32**	**−20.50**

The results distinctly revealed that, during winter, all stations have experienced negative trend. It was found that 18.2 and 45.4% of the stations have experienced significant negative trend during winter at the 0.01, 0.1 levels, respectively, while 36.4% of the stations have non-significant negative trend. The highest significant negative trend (–36.35 mm/decade) was found at Khanaqin, while the lowest negative trend (–4.4% mm/decade) was found at Samawa; the trend for Khanaqin is significant at the 0.01 level, while Samawa showed non-significant decreasing trend. During spring, only four stations (36.4% of stations) have experienced non-significant positive trend, while the remaining stations (63.6% of stations) have experienced non-significant negative trend. It could also noticed, that Samawa experienced the highest non-significant positive trend (0.68 mm/decade) while Kirkuk experienced the lowest non-significant negative trend (–7.69 mm/decade), see *Figs. 5* and *6* and *Table 3*.

In summer, the climate of Iraq is rainless and clear skies prevail. Therefore, all stations show no trend during this season. During autumn, only seven stations (63.6% of stations) have experienced non-significant positive trend, while the remaining four stations (36.4% of the stations) have experienced non-significant negative trend. It could be noticed that the highest positive trend during the autumn season (2.31 mm/decade) occurred at Khanaqin station, while the lowest negative trend (–1.53 mm/decade) occurred at Mosul station (*Figs. 5* and *6* and *Table 3*).

Annually, negative trends of total rainfall have been observed at all stations except Samawa, which showed non-significant positive trend (2.31 mm/decade). It was found that 9.1, 9.1, and 36.4% of the stations have experienced significant negative trend at the 0.001, 0.01, and 0.05 levels, respectively, while 36.4 and 9.1%

of the stations showed non-significant negative and positive trends respectively. The trends range from –7.83 mm/decade at Nasiriya to –41.96 mm/decade at Khanaqin; the trend for Khanaqin is significant at the 0.001 level, while Nasiriya showed non-significant negative trend (*Figs. 5* and *6* and *Table 3*).

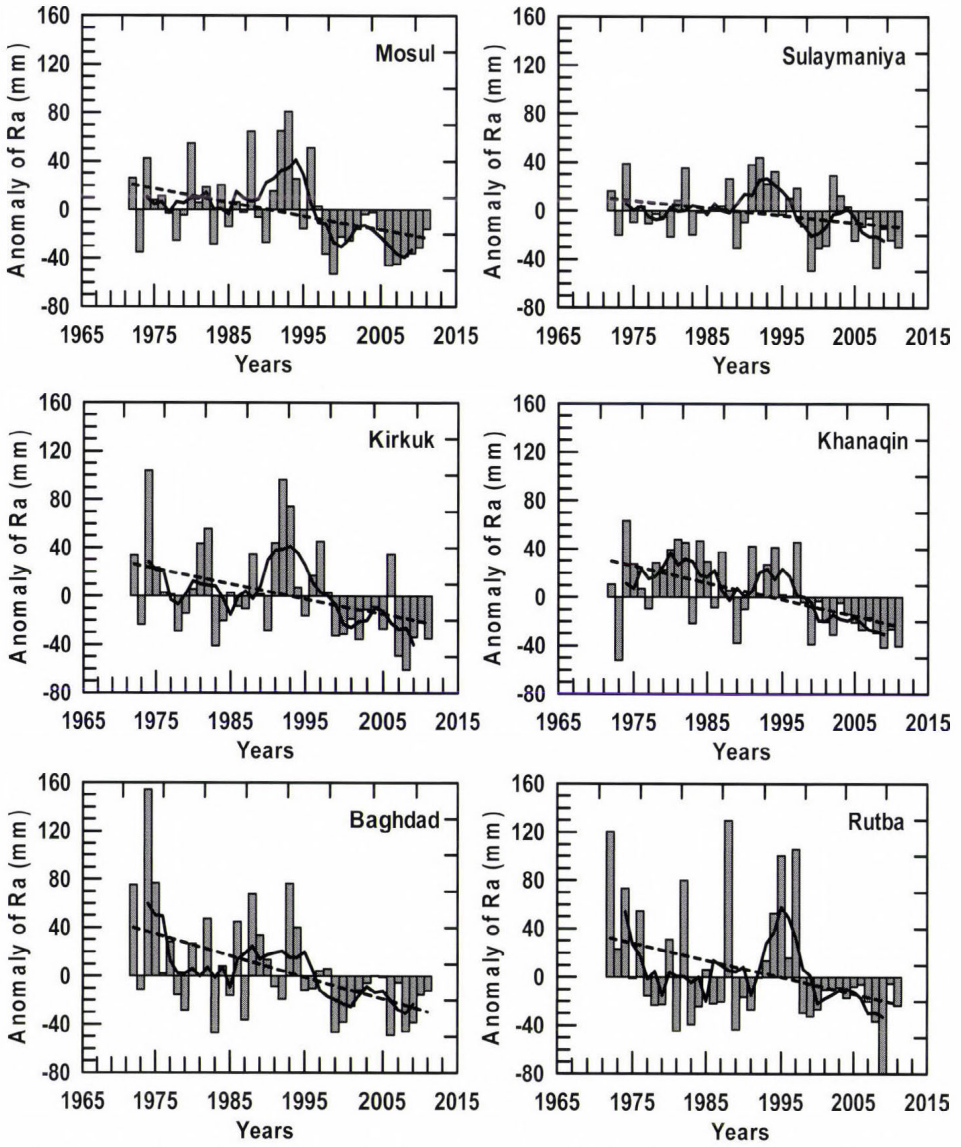

Fig. 5. Anomalies of the rainfall amount (*Ra*, mm) for the eleven selected stations during the studied period (1972–2011), for the baseline (1982–2011) average. The bars indicate the anomalies of the years, the zigzag line represents five-year means, and the straight line indicates the long-term linear trends.

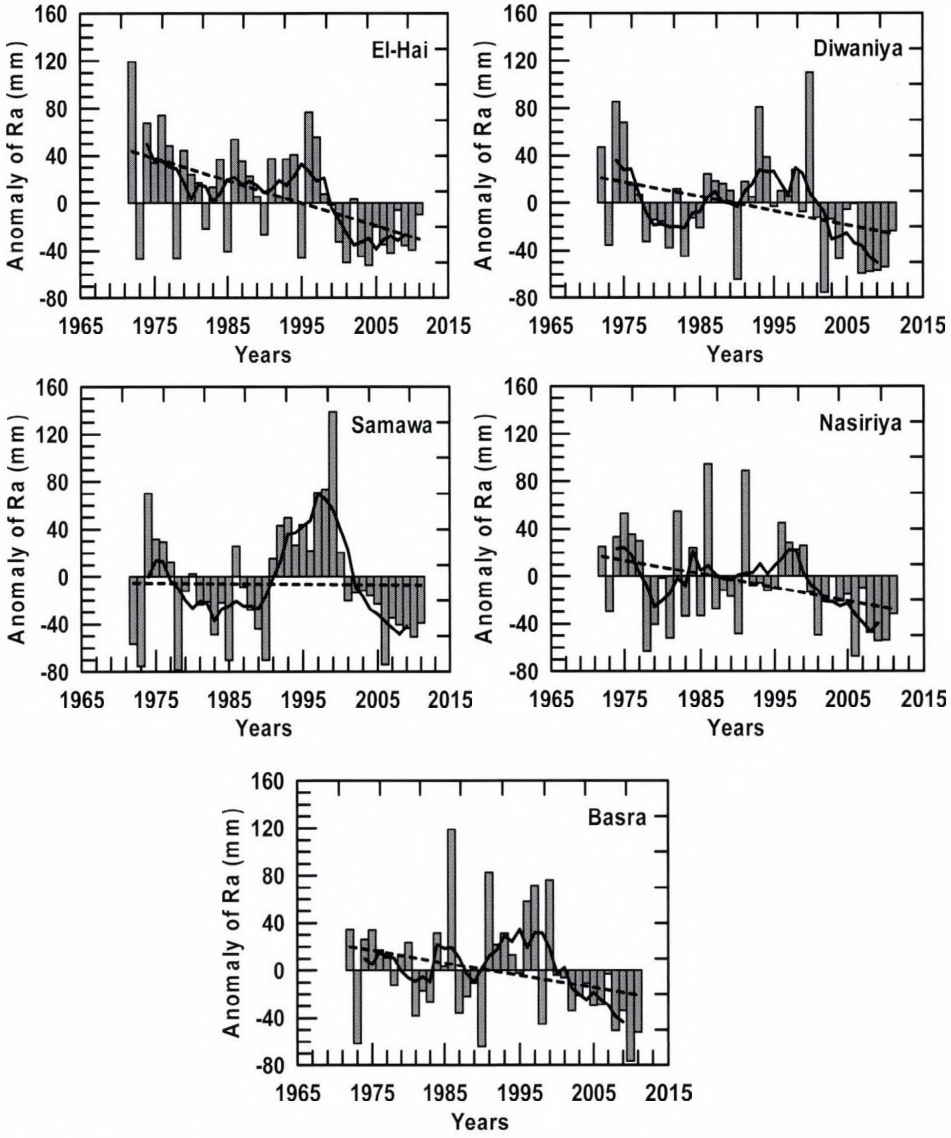

Fig. 5. (Continued).

It could be concluded, that the trends of R_a were negative over the whole country of Iraq except for Samawa, where the observed rainfall has slightly increased. The average rate of R_a decreased over the whole Iraq, and it has been found –15.48 mm/decade, –1.89 mm/decade, –0.32 mm/decade during winter,

spring, and autumn seasons, respectively, and –20.5 mm/decade annually, while no consistent changes were found during the summer season. Majority of the trends indicated reduced precipitation during winter. It is also noticed, that the rainfall showed a negative trend in 90.9% of the stations, but there is 9.1% of the stations with positive trend in the whole Iraq (see *Fig. 6* and *Table 3*). This result agrees with the findings of *Raziei et al.*, (2005) and *Tabari* and *Talaee* (2011b), who found a significant negative trend in the annual precipitation series in Iran.

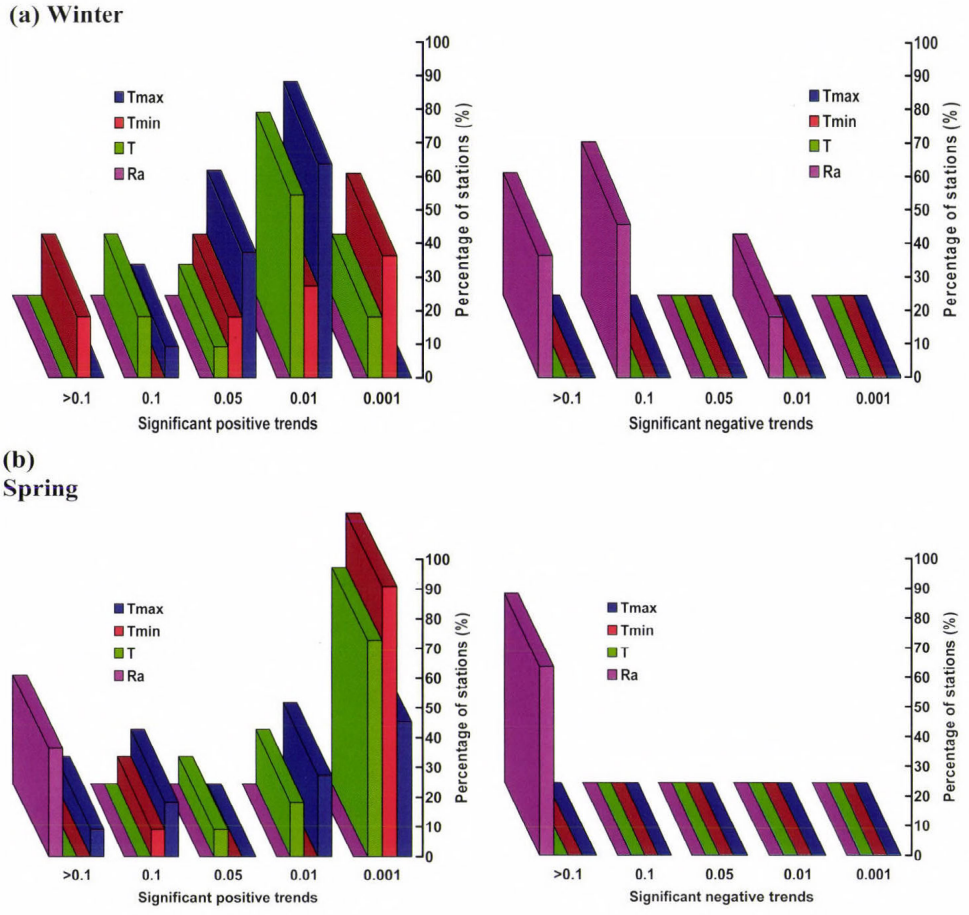

Fig. 6. The percentage of stations with significant positive and negative trends for T_{max}, T_{min}, T, and Ra by the Mann-Kendall test during (a) winter, (b) spring, (c) summer, (d) autumn, and (e) annual.

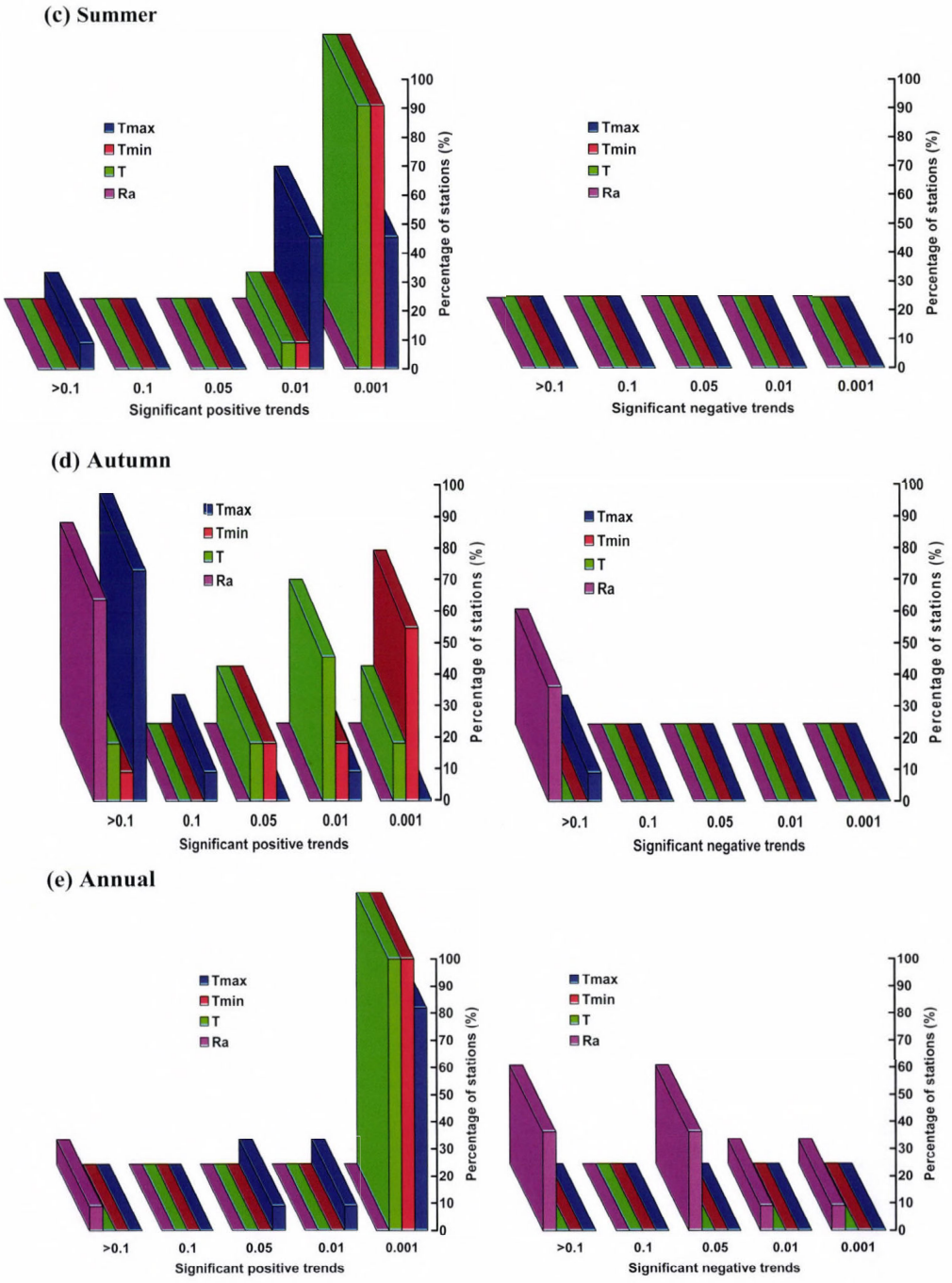

Fig. 6. (Continued).

4. Conclusions

The present study is mainly concerned with the changing trend of air temperatures and rainfall in Iraq. A complete set of measurements for maximum (T_{max}), minimum (T_{min}) and mean air temperatures (T) in addition to rainfall amounts (R_a) for the period 1972–2011 at 11 meteorological stations in Iraq have been used. Statistical tests including the Mann-Kendall test, the Sen's slope estimator, and linear regression were used for the analysis. Final results and conclusions could be summarized in the following points:

1. Annual mean of T_{max}, T_{min}, and T time series showed statistically significant increasing trends over 81.8, 100, and 100% of the stations at the 0.001 level, and they experienced an increase of 0.50, 0.67, and 0.58 °C/decade, respectively.
2. The significant positive trends of T_{max}, T_{min}, and T can be observed clearly during spring and summer than during winter and autumn.
3. There is not any stations which have significant or non-significant negative trend for air temperatures in the whole Iraq except Diwaniya, where the trend of T_{max} was weakly negative during autumn.
4. Annual rainfall has shown decreasing trends at all stations (except Samawa), and it experienced an decrease of –20.50 mm/decade.
5. Seasonally, the highest increase of T_{max}, T_{min}, and T values have been found at the extreme south of the country (Basra) during summer at the rates of 1.47, 1.06, and 1.16 °C/decade, respectively, while the lowest increase of the air temperatures prevail in the northern part of the country, especially at Kirkuk.
6. The highest decrease of R_a values has been found in the northern part of the country (Khanaqin) during winter at the rate of –36.35 mm/decade.
7. The warming pattern occurred shortly after 1995 at all stations.

Changes in air temperature and rainfall amounts will have significant impacts on biodiversity and food security in Iraq. Therefore, substantial reductions of heat-trapping gas emissions and adaptation strategies are crucial in Iraq.

References

Al-Ansari, N. and *Knutsson, S.*, 2011: Toward Prudent management of Water Resources in Iraq. *J.Adv. Sci. Engineer. Res. 1*, 53–67.

Al-Ansari, N., Al-Oun, S., Hadad, W., and Knutsson, S. 2013: Water loss in Mafraq Governorate, Jordan. Natural Sci. 5, 333–340.

Arora, M., Goel, N.K., and *Singh ,R.* 2005: Evaluation of temperature trends over India. *Hydrol. Sci. J. 50.*, 81–93.

Busuioc, A., Caian, M., Cheva, S., Bojariu, R., Boroneant, C., Baciu, M., and Dumitrescu, A., 2010: Climate variability and change in Romania. Ed. Pro Universitaria, Bucharest.

Chen, H., Guo, S., Chong-yu, X., and *Singh, V.P.,* 2007: Historical temporal trends of hydro-climatic variables and runoff response to climate variability and their relevance in water resource management in the Hanjiang basin. *J. Hydrol. 344*,171–184.

Croitoru, A.E., Holobaca, I.H., Lazar, C., Moldovan, F., and *Imbroane, A.,* 2012: Air temperature trend and the impact on winter wheat phenology in Romania. *Climatic Change 111*, 393–410.

Croitoru, A.E. and *Piticar, A.,* 2013: Changes in daily extreme temperatures in the extra-Carpathians regions of Romania. *Int. J. Climatol. 33,* 1987–2001.

Diaz, H.F., Bradley, R.S., and *Eischeid, J.K.,* 1989: Precipitation fluctuations over global land areas since the late 1800s. *J Geophis. Res. 94*, 1195–1210.

Dore, M.H.I., 2005: Climate change and changes in global precipitation patterns: what do we know. *Environ. Int. 31*, 1167–1181.

EEA. 2008: Impacts of Europe's changing climate -2008 indicator-based assessment. *EEA report 4*, 242.

Efstathiou, M.N., Tzanis, C., Cracknell, A., and *Varotsos, C.A.,* 2011: New features of the land and sea surface temperature anomalies. *Int. J. Remote Sens. 32*, 3231–3238.

Eichner, J.F., Koscielny-Bunde, E., Bunde, A., Havlin, S., and *Schellnhuber, .HJ.* (2003) Power-law persistence and trends in the atmosphere: A detailed study of long temperature records. *Phys. Rev. E., 68,* 046133.

Folland, C.K., Rayner, N.A., Brown, S.J., Smith, T.M., Shen, S.S.P., Parker, D.E., Macadam, I., Jones, P.D., Jones, R.N., Nicholls, N., and Sexton, D.M.H. 2001: Global temperature change and its uncertainties since 1861. Geophys. Res. Lett. 28, 2621–2624.

Gemmer, M., Becker, S., and *Jiang, T.* 2004: Observed monthly precipitation trends in China 1951–2002. *Theor. Appl. Climatol. 77*, 39–45.

Hulme, M., Osborn, T.J., and *Johns, T.C.*, 1998: Precipitation sensitivity to global warming: comparison of observations with HADCM2 simulations. *Geophys. Res. Lett. 25*, 3379–3382.

Ionita, M., Rimbu, N., Chelcea, S., and *Patruţ, S.,* 2013: Multidecadal variability of summer temperature over Romania and its relation with Atlantic Multidecadal Oscilation. *Theor. Appl. Climatol. 113*, 305–315.

Jones, P.D., 1994: Hemispheric surface air temperature variations: A reanalysis and an update to 1993. *J. Climate 7,* 1794–1802.

Jones, P.D., New, M., Parker, D.E., Martin, S., and *Rigor, I.G.*, 1999: Surface air temperature and its changes over the past 150 years. *Rev. Geophys. 37*,173–199.

Jones, P.D. and *Moberg, A.* 2003: Hemispheric and Large-Scale Surface Air Temperature Variations: An Extensive Revision and Update to 2001. *J. Climate 16,* 206–223.

Kayano, M.T. and *Sansıgolo, C.,* 2008: Interannual to decadal variations of precipitation and daily maximum and daily minimum temperatures in southern Brazil. *Theor. Appl. Climatol. 97*, 81–90.

Kendall, M.G., 1938: A new measure of rank correlation. *Biometrika 30*, 81–93.

Kendall, M.G., 1975: Rank Correlation Methods. 4th ed. Charles Griffin: London, UK; 272.

Lambert, F., Stott, P., and *Allen, M.,* 2003: Detection and attribution of changes in global terrestrial precipitation. *Geophys. Res. Abst. 5*, 06140.

Luo, Y., Liu, S., Fu, S.F., Liu, J., Wang, G., and *Zhou, G.,* 2008: Trends of precipitation in Beijiang River Basin, Guangdong Province, China. *Hydrological Proc. 22*, 2377–2386.

Luterbacher, J., Dietrich, D., Xoplaki, E., Grosjean, M., and *Wanner, H.,* 2004: European seasonal and annual temperature variability, trends, and extremes since 1500. *Science 303*,1499–1503.

Mann, H.B., 1945: Non-parametric tests against trend. *Econometrica 33*, 245–259.

Marco, G., Stefan, B., and *Tong. J.,* 2003: Detection and Visualization of Climate Trends in China. No. 15, Giessen, Nanjing Institute of Geography and Limnology, Chinese Academy of Science (CAS), 210008 Nanjing, PR China.

Nicholls, N., Gruza, G.V., Jouzel, J., Karl, T.R., Ogallo, L.A., and Parker, D.E., 1996: Observed climate variability and change. In (Eds.: Houghton, J.T., Filho, L.G.M., Callander, B.A., Harris,

N., Kattenberg, A., and Maskell, K.).Climate Change 1995: The Science of Climate Change. Cambridge University Press: Cambridge; 133–192.

Raziei, T., Arasteh, P.D., and *Saghafian, B.,* 2005: Annual rainfall trend in arid and semi-arid regions of Iran. ICID 21st European regional conference, Frankfurt (Oder) and Slubice-Germany and Poland.

Piticar, A. and *Ristoiu, D.* 2012: Analysis of air temperature evolution in Northeastern Romania and evidence of warming trend. *Carpathian J. Earth Environ. Sci. 7,* 97–106.

Rebetez, M. and *Reinhard, M.,* 2008: Monthly air temperature trends in Switzerland 1901–2000 and 1975–2004. *Theor. Appl. Climatol. 91*, 27–34.

Rybski, D., Bunde, A., Havlin, S., and *von Storch, H.,* 2006: Long-term persistence in climate and the detection problem. *Geophys. Re. . Lett. 33*, l06718.

Salmi, T., Maata, A., Antilla, P., Ruoho-Airola, T., and *Amnell, T.,* 2002: Detecting trends of annual values of atmospheric pollutants by the Mann–Kendall test and Sen's slope estimates – the Excel template application MAKESENS. Finnish Meteorological Institute, Helsinki, Finland.

Schaefer, D., 1996: Uni- und multivariate statistische Untersuchungen zu rezenten Klima¨anderungen in Sri Lanka. PhD thesis, Institute of Geography, Mainz University, Germany.

Schoenwiese, C., 1992: Praktische Statistik für Meteorologen und Geowissenschaftler, second ed. Gebrüder Borntraeger, Berlin and Stuttgart.

Sen, P.K., 1968: Estimates of the regression coefficient based on Kendall's tau. *J. Amer. Stat. Assoc. 63*, 1379–1389.

Smadi, M.M., 2006: Observed abrupt changes in minimum and maximum temperatures in Jordan in the 20th century. *Amer. J. Environ. Sci. 2,* 114–120.

Smadi, M.M. and *Zghoul, A.,*2006: A sudden change in rainfall characteristics in Amman, Jordan during the mid 1950s. *Amer. J. Environ. Sci. 2,* 84–91.

Stephenson, T.S., Vincent, L.A., Allen, T., Van Meerbeeck, C.J., McLean, N., Peterson, T.C., Taylor, M.A., Aaron-Morrison, A.P., Auguste, T., Bernard, D., Boekhoudt, J.R.I., Blenman, R.C., Braithwaite, G.C., Brown, G., Butler, M., Cumberbatch, C.J.M., Etienne-Leblanc, S., Lake, D.E., Martin, D.E., McDonald, J.L., Zaruela, M.O., Porter, A.O., Ramirez, M.S., Tamar, G.A., Roberts, B.A., Mitro, S.S., Shaw, A., Spence, J.M., Winter, A., and *Trotman, A.R.,* 2014: Changes in extreme temperature and precipitation in the Caribbean region, 1961–2010. *Int. J. Climatol. 34*. 2957–2971.

Tabari, H. and Talaee, H. P. 2011a: Recent trends of mean maximum and minimum air temperatures in the western half of Iran. *Meteor. Atmos. Phys. 111*, 121–131.

Tabari, H. and *Talaee, H.P.*, 2011b: Temporal variability of precipitation over Iran: 1966–2005. *J. Hydrol 396*, 313–320.

Yu, B. and *Neil, D.T.,* 1993: Long-term variations in regional rainfall in the south-west of Western Australia and the difference between average and high intensity rainfalls. *Int. J. Climatol. 13*, 77–88.

Varotsos, C.A., Efstathiou, M.N., Cracknell, A.P., 2013: On the scaling effect in global surface air temperature anomalies. *Atmos. Chem. Phys. 13*, 5243–5253.

Watson, R.T., Zinyowera, M.C., and *Moss, R.H.,* (eds) 1998: The Regional Impacts of Climate Change: An Assessment of Vulnerability. Cambridge University Press: Cambridge UK.

Zhang, X., Harvey, K.D., Hogg, W.D., and *Yuzyk, T.R.* 2001: Trends in Canadian streamflow. *Water Resour. Res. 37*, 987–998.

IDŐJÁRÁS

Quarterly Journal of the Hungarian Meteorological Service
Vol. 119, No. 4, October – December, 2015, pp. 515–535

Continentality in Europe according to various resolution regional climate models with A1B scenario in the 21st century

Beáta Szabó-Takács[1]*, **Aleš Farda**[1,3], **Pavel Zahradníček**[1,2], and **Petr Štěpánek**[1,2]

[1] *Global Change Research Centre AS CR, v.v.i.*
Bělidla 986/4a, 60300 Brno, Czech Republic

[2] *Czech Hydrometeorological Institute, branch Brno,*
Kroftova 43, 616 00 Brno, Czech Republic

[3] *Czech Hydrometeorological Institute,*
Na Šabatce 17, 143006 Prague, Czech Republic

* *Corresponding authors E-mail: szabo.b@czechglobe.cz*

(Manuscript received in final form January 8, 2015)

Abstract— The purpose of our research is to simulate the influence of the thermal properties of land surface on the Central European climate in the 21st century. The simulation is carried out with calculation of Gorczynsky and Conrad continentality indexes, respectively, as a function of annual temperature range. Seven different ENSEMBLES models (ARPÈGE, CNRM, DMI, ITCP, KNMI, MPI, and SMHI) with various resolutions perform the space difference of continentality between seven European regions with IPCC A1B emission scenario for two time slices: 2021–2050 and 2071–2100. Beside these models, ALADIN-Climate/CZ simulation is implemented in finer resolution and smaller CECILIA domain taking into consideration only the central European area. The bias correction of models is implemented using the European Climate Assessment and Dataset (ECA&D). The largest influence to the spread among the simulation results is due to the chosen global climate models (GCMs). The resolution differences do not play dominant role in the variance of the results against the domain size. There are not significant differences between the Gorczynsky and Conrad index values. The largest change in the climate type tendency is simulated in the Scandinavian region by the Gorczynsky approach. In central Europe, the climate becomes continental only according to CNRM result which correlates with its underestimation of precipitation and overestimation of temperature. The simulated continentality indexes and the predicted changes are presented here.

Key-words: continentality, Gorczynsky index, Conrad index, ENSEMBLES, climate change, E-OBS

1. Introduction

Continentality is a basic indicator of climate change. In the climate of central Europe, oceanic and continental climate effects are combined. The continental climate areas have great annual temperature range and moderate precipitation (*McBoyle* and *Steiner,* 1972), whilst the oceanic climate is more balanced. The reason of this basic difference comes from the different thermal properties of ocean and land surface. The oceans have larger heat capacity, whilst the inland has larger heat conduction, which depends on surface properties (*Nikiforova et al.*, 2013). The combination of heat capacity and thermal conductivity determines three important physical properties underlying climate: (i) the proportion of heat shared by the interface substances; (ii) the depth (soil, water) or height (atmosphere) to which heat flows or transported; (iii) the range of temperatures over diurnal and annual cycles (*Dirscoll* and *Yee Fong,* 1992). This phenomenon has an effect on several climatic elements like distribution of cloudiness, precipitation, etc., which impact the temperature anomaly. Different approaches are used to quantify continentality (*Gorczynsky,* 1922; *Johansson,* 1926; *Conrad* and *Pollak,* 1950; *Currey,* 1974; *Holmlund* and *Schneider,* 1997; *Sládek,* 2005; *Mikolaskova,* 2009).

The purpose of our work is to investigate the formation of the spatial differences of continentality in Central Europe using ENSEMBLES based on A1B SRES scenario in the 21th century. The A1B estimates the future world in perspective of technical change in energy system with the assumption that similar improvement rates apply to all energy supply and end use technologies (*Nakićenovíc,* 2000, *Solomon,* 2007).

The EU 6th Framework Programme project ENSEMBLES applies a probabilistic approach to climate changes at a regional scale (*Hewit* and *Griggs,* 2004) with downscaling global circulation models (GCM) to higher resolution regional climate models (*van der Linden* and *Mitchell,* 2009).

The sources of uncertainties in the ENSEMBLES predictions are the chosen GCM, RCM, downscaling technique, and natural variability. The choice of GCM significantly determines the initial and boundary conditions of RCMs. The source of differences in RCMs comes from the difference of the applied physical parameterizations to represent sub-grid effects. There are two basic downscaling techniques: dynamical and statistical. The dynamical downscaling is not able to improve the simulation skills of large-scale fields over those simulated by the GCM (*Dosio* and *Paruolo,* 2011), while the statistical relationship is developed for present day climate by statistical downscaling is assumed to be valid for future climate under different forcing condition (*Wilby et al.,* 1998). The natural variability, such as seasonal cycle of insolation, non-linear interplay of feedbacks, and random fluctuations in physical or chemical factors also has an effect on the uncertainties. *Déqué et al.* (2012) found that the natural variability produces significantly larger mean interannual spread in a given model than running an ensemble of the same size without considering

perturbing the parameters. According to *Kjellström et al.* (2011), the lower natural variability in ECHAM5 and smaller large-scale circulation changes in HadCM3 (ECHAM5-r2 and HadCM3-low) show larger warming in much of Europe than the larger one (ECHAM5-r3 and HadCM3-high).

2. Data and method

The calculations were implemented in the variable resolution ARPÈGE 4. atmospheric global climate model (AGCM), and in six different 25 km resolution regional climate models (RCMs) for the European area using Gorzynsky and Conrad indexes, respectively. The resolution of ARPÈGE is 50 km over Central Europe and decreases to 300 km at the antipodes. The ENSEMBLES models chosen for our study are shown in *Table 1*. They are representative selection of models with respect to GCMs/RCMs combination. The temperature anomaly and continentality were predicted for 2021–2050 and 2071–2100.

Table 1. The institute, reference, GCM, RCM, and resolution of chosen ENSEMBLES simulations

	INSTITUTE/ REFERENCE	**GCM**	**RCM**	**RESOULTION**
1	ARPÈGE *Gibelin* and *Déqué*, (2003)	ARPÈGE	-	50 km
2	CNRM/ *Déqué* (2007)	ARPÈGE	ALADIN	25 km
3	DMI/ *Christensen et al.* (1996)	ARPÈGE	HIRHAM	25 km
4	KNMI/ *Lenderink et al.* (2003)	ECHAM5-r3	RACMO	25 km
5	SMHI/ *Kjellström et al.* (2005)	ECHAM5-r3	RCA	25 km
6	MPI/ *Jacob* (2001)	ECHAM5-r3	REMO	25 km
7	ICTP/ *Giorgi et al.* (2004)	ECHAM5-r3	RegCM	25 km
8	CHMI/ *Farda et al.* (2007)	ARPÈGE	ALADIN/CZ	10 km

Since the models contain bias, it is necessary to correct their outputs. An important point in the correction is the availability of suitable reference data, e.g., observations or re-analyses. On the European level, the biggest database of daily meteorological station observations is the European Climate Assessment and Dataset (ECA&D). The ECA&D project (*Klein Tank et al.,* 2002) was initiated by the European Climate Support Network of EUMETNET in 2002, and it was coordinated by the Royal Netherlands Meteorological Institute

(KNMI). ECA&D daily database contains more than 31k quality controlled series of 12 climate variables at more than 7000 meteorological stations in 62 countries, from which about half of them are public (*Fig. 1*). Using the ECA&D blended daily station data, the E-OBS daily high-resolution gridded observational dataset was produced. The E-OBS (*Haylock et. al.,* 2008) is currently perhaps the best pan-European gridded dataset with the spatial resolution of 0.25° in longitude and latitude (or 0.22° on the rotated pole grid typical for many RCMs) covering the period from 1950.

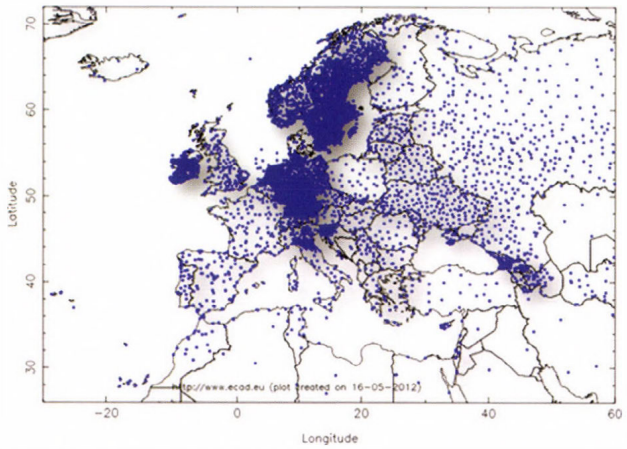

Fig. 1. Meteorological stations of ECA&D database.

The RCMs were corrected on the monthly scale. In the first step for each RCM grid point, the nearest E-OBS grid points were found. The differences of control run of RCM models and E-OBS database (applying reference period 1961–2000) were calculated for each month individually. Found differences were used for correcting the RCM outputs. It has been calculated for more than 14,000 grid points.

Considering the Central European area (Czech Republic (CR), Slovakia (SK), North-East Austria (AT)), the calculations were carried out with the 10 km resolution ALADIN/CZ RCM (*Fig. 2*). The regional climate model ALADIN - Climate/CZ is an adaptation of ALADIN numerical weather prediction model, version CY28T3. Within the EU FP6 project CECILIA, it was coupled with the GCM ARPEGE to provide a projection of future climate in two time slices, 2021–2050 and 2071–2100, according to the IPCC A1B emission scenario. Its description can be found, e.g., in *Farda et al.* (2007) or *Farda et al.* (2010). Before the analysis of the future climate, the model data were corrected, in daily

step, according to validation results carried out for the period 1961-2000. For this purpose (comparison with "truth"), the so-called technical series were recalculated from station data in the positions of grid points of the model (ALADIN-Climate/CZ grid at 10 km horizontal resolution, for the details about the method see, e.g., *Štěpánek et al.,* 2011a). All input station observations were quality controlled, homogenized in daily scale, and gaps in data were filled (for more information about the preprocessing of station data please refer to *Štěpánek et al.,* 2011b, 2013). According to the relationship between the RCM outputs and the recalculated station data (technical series for the grid points), outputs of A1B scenario integrations of the future climate were corrected applying an approach of *Déqué et al.* (2007) that is based on a variable correction using individual percentiles. The model outputs are fully compatible with the station (measured) data. As mentioned above, these data were processed at daily scale, from which final monthly values were then calculated. All data processing was performed by ProClimDB database software for processing of climatology datasets (free download is possible from www.climahom.eu).

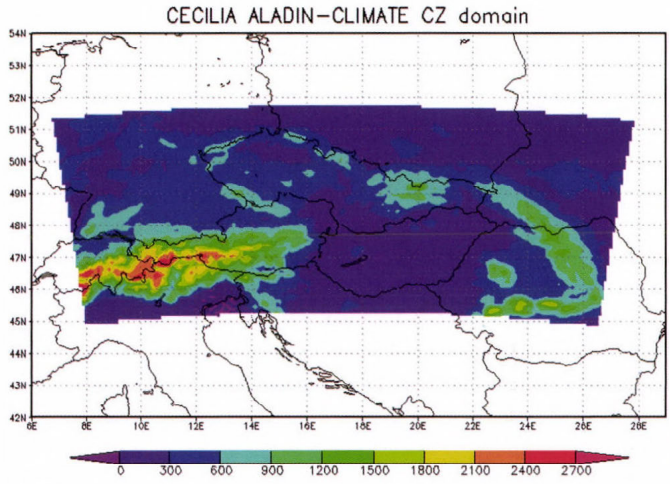

Fig. 2. Integration area with orography and used grid points details of model ALADIN-Climate/CZ as used in EC FP6 CECILIA project.

Owing to the higher density station network used for the correction, this dataset is expected to be subject of smaller interpolation error than E-OBS (*Hofstra et al.,* 2010).

The continentality index is calculated as a function of annual temperature anomaly divided by the sine of latitude to compensate for seasonal differences in radiation. The Gorzynsky index is most commonly used in Europe. It is computed by the equation:

$$k = \frac{1.7(A - 12\sin\theta)}{\sin\theta} = \frac{1.7A}{\sin\theta} - 20.4, \quad (1)$$

where A is the mean annual anomaly of temperature in °C, and θ is the latitude in degree. According to *Gorczynsky* (1922), the expression of $A=12\sin\theta$ corresponds well with observation over the ocean. The 1.7 constant is calculated from the assumption that Verchojansk, in eastern Siberia, is representative of 100% continentality (*Mikolaskova,* 2009). Based on the equation, the continentality can be divided into three categories: transitional maritime (k=0 to 33%), continental (k=33 to 66%), and extreme continental (k=67 to 100%) *Gorczynsky* (1922).

Conrad and *Pollak* (1950) found that the Gorczynsky approach gives negative values, which does not have physical meaning in some particular locations (e.g., Thorshvan at Faeroe Islands), hence they modified the equation with taking into account boundary conditions. The Conrad continentality index can be calculated by the equation:

$$k = \frac{1.7A}{\sin(\theta + 10)} - 14. \quad (2)$$

If the index value is 0, the climate is no longer influenced by continental surface, and if the value is 100, the climate is no longer influenced by maritime air masses (*Mikolaskova,* 2009). This index reaches better results in lower latitudes (e.g., 0), but its results are invalid in latitudes higher than 80.

The Pan-European domain originally designed for the ENSEMBLES project (*van der Linden* and *Mitchell,* 2009) is divided into seven regions for investigating the spatial differences of ENSEMBLES predicted annual temperature anomaly and continentality. The chosen regions are Southern Europe (1), Western Europe (2), Great Britain (3), Scandinavia (4), Central Europe (5), South-Eastern Europe (6), and Eastern Europe (7) represented in *Fig. 3*.

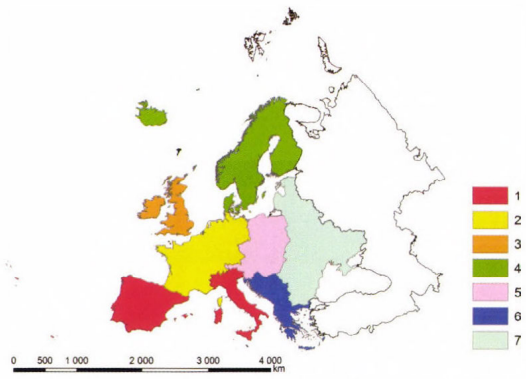

Fig. 3. Regions of ENSEMBLES domain: 1. South Europe, 2. Western Europe, 3. Great Britain, 4. Scandinavia, 5. Central Europe, 6. South-East Europe, and 7. East-Europe.

3. Results

3.1. Temperature anomaly

Table 2 shows the predicted mean annual temperature anomaly in the different regions in the 2021–2050 and 2071–2100 periods. The mean values denote that the temperature range increases eastward and toward the center of South Europe in both time periods. Increasing the distance from the Atlantic Ocean increases the temperature anomaly toward the east direction. The larger anomaly in South Europe can be explained with the topography, which modifies the intensity and depth of penetration of maritime influences. This block of wet maritime airmass is combined with rise of aridity which increases the temperature anomaly (*Dirscoll* and *Yee Fong*, 1992).

Table 2. Predicted mean annual temperature amplitudes T_{mean} in 2021–2050 (top) and 2071–2100 (bottom) for the defined regions: South Europe (1), Western Europe (2), Great Britain (3), Scandinavia (4), Central Europe (5), South-East Europe (6), East-Europe (7)

	Temperature amplitude in 2021–2050						
Region	**ARPÈGE** T_{mean}	**CNRM** T_{mean}	**DMI** T_{mean}	**ICTP** T_{mean}	**KNMI** T_{mean}	**MPI** T_{mean}	**SMHCI** T_{mean}
1	18.8	18.8	18.3	19.0	19.0	19.1	19.4
2	18.3	18.5	18.0	17.9	18.0	18.0	17.8
3	13.0	13.2	12.7	13.0	12.9	12.8	12.6
4	22.6	22.9	22.7	23.1	23.1	22.6	22.7
5	22.0	21.9	21.8	21.3	21.4	21.2	21.0
6	22.7	22.6	21.5	21.4	21.4	21.4	21.3
7	26.4	26.2	25.5	24.7	24.9	24.5	24.4
	Temperature amplitude in 2071–2100						
Region	**ARPÈGE** T_{mean}	**CNRM** T_{mean}	**DMI** T_{mean}	**ICTP** T_{mean}	**KNMI** T_{mean}	**MPI** T_{mean}	**SMHCI** T_{mean}
1	20.4	20.5	20.0	20.7	20.8	21.0	21.1
2	20.0	20.9	19.4	18.3	18.7	18.1	18.1
3	13.1	13.8	13.0	12.9	12.9	12.6	12.4
4	21.2	21.7	21.2	21.5	21.5	21.2	20.5
5	23.3	24.6	22.6	21.0	21.6	20.6	20.7
6	24.7	24.9	23.1	22.2	22.5	22.4	22.5
7	27.4	27.7	25.8	24.7	25.1	24.1	24.2

In 2021–2050, the spread among the predicted mean annual temperature anomalies are smaller than 0.3 in the Western Europe, Great-Britain, and Scandinavia regions (*Table 3a*). In the other regions, differences appear between ARPÈGE and ECHAM5-r3 driven RCMs results, respectively. The temperature range values are higher for RCMs forced by ARPÈGE except in South Europe. The ECHAM5 driver is coupled ocean-atmosphere GCM, while ARPÈGE is forced by the SST and sea-ice conditions of ERA40 (*Déqué* personal discussion) with added delta monthly anomaly from HadCM3 GCM (*Déqué,* 2007). The sea-ice extension is overestimated by HadCM3_ref, while it is underestimated by ECHAM5. Large-scale circulation in ECHAM5 is too zonal which transports the cool and moist air from the North Atlantic in summer (*Kjellström et al.,* 2011), and warm air is advected from the North Atlantic into the Baltic Sea region in winter combined with reduction of sea-ice albedo (*Meier et al.,* 2011). This too strong influence of the Atlantic Ocean on the surface temperature also contributes to the climate of the Central European regions, where it reduces the continental influences (*Plavcová* and *Kyselý*, 2011). The variability of the models is the largest in Scandinavia, which can also contribute to the SST and sea-ice condition caused natural variability.

The predicted change values are calculated by differences between the model predicted future (T_M) and E-OBS measured present (T_E) mean temperature anomalies. These values are negative in both RCMs in Scandinavia and in the ECHAM5 driven RCMs in Central and East Europe too, respectively. These negative values mean that the climate will be more balanced in the future than in the present. ARPÈGE has the largest positive differences in South-East Europe due to the increasing drought resulted from underestimating the precipitation in summer (*Gibelin* and *Déqué,* 2003; *Déqué,* 2007).

Compared with the 2021–2050 term, the mean annual temperature spread among the models increases in each regions in the 2071–2100 time period. Its largest value is 1.5 in Central Europe and the smallest is in Scandinavia region (*Table 3b*). In Central Europe, the mean annual temperature range increases in ARPÈGE driven RCMs and diminishes in ECHAM5 forced ones except KNMI compared with the 2021–2050 period. Moreover, the boundaries of the anomaly become slantwise to south-west north-east direction (not shown).

The mean annual temperature anomalies are also larger in RCMs forced with ARPÈGE except in South Europe. CNRM has the largest mean annual temperature anomalies and the highest predicted change in Central, South-East, and East Europe. SMHCI results the smallest mean annual temperature anomaly except in South Europe and Scandinavia. The variability of the models increases in each region in time with exception of Scandinavia area (not shown). Its value is higher in both time period due to the higher natural variability of the ECHAM5 forced RCMs (denoted by -r3). Because SSTs and sea-ice conditions are significant 'red noise' components (*Hasselmann,* 1976*; Rowell* and *Zwiers,* 1999),

the reduction of model variability in time refers to the fact that the signal (global warming) to noise (natural variability) is greater than in the former period.

In the most regions, the predicted change values increase with time (not shown). CNRM has the largest change values except in the Scandinavia area.

Table 3a. The spread of the simulated temperature amplitude of the models in 2021–2050 for the regions defined in *Table 2*

Spread of simulated temperature amplitude 2025-2050							
	1	**2**	**3**	**4**	**5**	**6**	**7**
ARPÈGE	18.8	18.3	13	22.6	22	22.7	26.4
CNRM	18.8	18.5	13.2	22.9	21.9	22.6	26.2
DMI	18.3	18	12.7	22.7	21.8	21.5	25.5
ICTP	19	17.9	13	23.1	21.3	21.4	24.7
KNMI	19	18	12.9	23.1	21.4	21.4	24.9
MPI	19.1	18	12.8	22.6	21.2	21.4	24.5
SMHCI	19.4	17.8	12.6	22.7	21	21.3	24.4
mean	**18.91**	**18.07**	**12.88**	**22.81**	**21.51**	**21.75**	**25.22**
spread	**0.33**	**0.24**	**0.20**	**0.21**	**0.38**	**0.61**	**0.81**

Table 3b. The spread of the simulated temperature amplitude of the models in 2071–2100 for the regions defined in *Table 2*

Spread of simulated temperature amplitude 2070–2100							
	1	**2**	**3**	**4**	**5**	**6**	**7**
ARPÈGE	20.4	20	13.1	21.2	23.3	24.7	27.4
CNRM	20.5	20.9	13.8	21.7	24.6	24.9	27.7
DMI	20	19.4	13	21.2	22.6	23.1	25.8
ICTP	20.7	18.3	12.9	21.5	21	22.2	24.7
KNMI	20.8	18.7	12.9	21.5	21.6	22.5	25.1
MPI	21	18.1	12.6	21.2	20.6	22.4	24.1
SMHCI	21.1	18.1	12.4	20.5	20.7	22.5	24.2
mean	**20.64**	**19.07**	**12.95**	**21.25**	**22.05**	**23.18**	**25.57**
spread	**0.37**	**1.07**	**0.44**	**0.38**	**1.50**	**1.13**	**1.46**

3.2. Gorczynsky index

The predicted mean Gorczynsky continentality indexes (Eq. (1)) in the 2021–2051 and 2071–2100 time slices are demonstrated in *Table 4*. According to the Gorczynsky index, the boundary of transitional maritime and continental climate is 33%. This boundary is near meridional in East Europe and against with *Mikolaskova,* 2009 results. Its direction is eastward in South-East and South Europe, respectively, in the 2021–2050 time slice (*Fig. 4*). The differences between the ARPÈGE and ECHAM5 driven model predicted indexes are analogous with the temperature amplitude ones.

In the 2021–2050 period, the climate is continental in South East and East Europe according to each model. The spread among the model results is smaller than 0.5 in Great Britain and Scandinavia, while it is greater than 1.0 in South East and East Europe (*Table 5a*).

The predicted change values are also negative in Scandinavia in case of each model and in Central and East Europe, respectively, in case of ECHAM5 forced RCMs (*Fig. 4*). The SMCHI has negative difference value in each region except for South- and South-East Europe, respectively, which relates with its smallest temperature anomaly values.

Correlating with temperature anomaly change, the Gorczynsky index depicts a sharp changing in the 2071–2100 period, where the continental climate slopes toward the north-east south-west direction. The continental climate recedes toward the southern direction in Scandinavia area, but increases in South and South-East Europe in both model cases. With exception of the Scandinavia area, index value increases in RCMs which are forced with ARPÈGE compared to the former period. In case of ECHAM5 driven RCMs, it decreases in more regions. The continentality rises in Central Europe only according to KNMI among ECHAM5 driven RCMs. In Central Europe, the continental climate predominates according to CNRM only where the index mean value is 34.5. CNRM has the largest mean annual temperature anomaly and the largest predicted change value in Central Europe in this period. *Christensen et al,* (2008) found that CNRM ALADIN has the largest positive temperature and negative precipitation biases from E-OBS observed data in Central European region compared with DMI, ICTP, KNMI, MPI, and SMHCI, when the RCMs were forced with ERA40. The spread among the model results is also the smallest in Scandinavia and Great Britain and the largest in South East and East Europe (*Table 5b*). The predicted change tendency is also analogous with the change of temperature range.

Table 4. Space differences of the predicted mean Gorczynsky index G_{mean} in 2021–2050 (top) and 2071–2100 (bottom) for the regions defined in *Table 2*

Gorczynsky index in 2021–2050							
Region	**ARPÈGE** G_{mean}	**CNRM** G_{mean}	**DMI** G_{mean}	**ICTP** G_{mean}	**KNMI** G_{mean}	**MPI** G_{mean}	**SMHCI** G_{mean}
1	28.4	28.5	27.1	29.1	29.1	29.2	29.9
2	21.5	21.8	20.8	20.6	20.6	20.6	20.2
3	7.1	7.5	6.6	7.0	7.0	6.7	6.4
4	22.8	23.2	22.9	23.6	23.7	22.8	22.8
5	28.7	28.4	28.1	27.2	27.2	26.9	26.3
6	37.2	36.7	34.0	33.8	33.8	33.7	33.6
7	39.2	38.8	37.2	35.3	35.7	34.9	34.6
Gorczynsky index in 2071–2100							
Region	**ARPÈGE** G_{mean}	**CNRM** G_{mean}	**DMI** G_{mean}	**ICTP** G_{mean}	**KNMI** G_{mean}	**MPI** G_{mean}	**SMHCI** G_{mean}
1	32.6	32.7	31.6	33.3	33.8	34.1	34.6
2	25.5	27.3	24.0	21.3	22.3	21.1	21.0
3	7.5	8.9	7.1	6.8	6.8	6.3	5.9
4	20.1	21.0	20.0	20.4	20.6	20.0	18.7
5	31.5	34.5	30.1	26.2	27.8	25.5	25.7
6	42.0	42.5	38.1	35.8	36.5	36.3	36.7
7	41.6	42.2	38.0	35.3	36.3	34.0	34.3

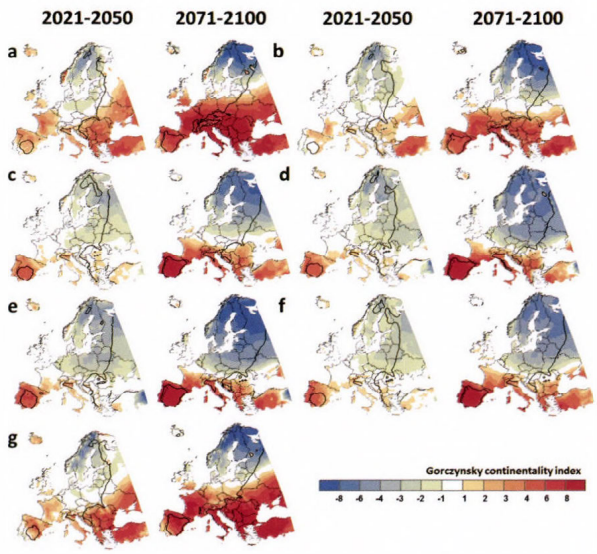

Fig. 4. Predicted changes of Gorczynsky indexes (a) CNRM, (b) DMI, (c) KNMI, (d) MPI, (e) SMHIRCA, (f) ICTP, and (g) ARPÈGE.

Table 5a. The spread of the simulated Gorczynsky index of the models in 2021–2050 for the regions defined in *Table 2*

Spread of simulated Gorczynsky index 2025-2050							
	1	**2**	**3**	**4**	**5**	**6**	**7**
ARPÈGE	28.4	21.5	7.1	22.8	28.7	37.2	39.2
CNRM	28.5	21.8	7.5	23.2	28.4	36.7	38.8
DMI	27.1	20.8	6.6	22.9	28.1	34	37.2
ICTP	29.1	20.6	7	23.6	27.2	33.8	35.3
KNMI	29.1	20.6	7	23.7	27.2	33.8	35.7
MPI	29.2	20.6	6.7	22.8	26.9	33.7	34.9
SMHCI	29.9	20.2	6.4	22.8	26.3	33.6	34.6
mean	**28.75**	**20.87**	**6.9**	**23.11**	**27.54**	**34.68**	**36.52**
spread	**0.88**	**0.56**	**0.36**	**0.39**	**0.87**	**1.55**	**1.88**

Table 5b. The spread of the simulated Gorczynsky index of the models in 2071–2100 for the regions defined in *Table 2*

Spread of simulated Gorczynsky index 2070-2100							
	1	**2**	**3**	**4**	**5**	**6**	**7**
ARPÈGE	32.6	25.5	7.5	20.1	31.5	42	41.6
CNRM	32.7	27.3	8.9	21	34.5	42.5	42.2
DMI	31.6	24	7.1	20	30.1	38.1	38
ICTP	33.3	21.3	6.8	20.4	26.2	35.8	35.3
KNMI	33.8	22.3	6.8	20.6	27.8	36.5	36.3
MPI	34.1	21.1	6.3	20	25.5	36.3	34
SMHCI	34.6	21	5.9	18.7	25.7	36.7	34.3
mean	**33.24**	**23.21**	**7.04**	**20.11**	**28.75**	**38.27**	**37.38**
spread	**1.02**	**2.46**	**0.96**	**0.72**	**3.04**	**2.81**	**3.36**

3.3. Conrad index

The mean Conrad index value is smaller than the Gorczynsky one in South, South-East, and East-Europe, respectively, according to each model (*Table 6*). The difference between the two indexes is the largest in Great-Britain due to the denominator and the smallest in East-Europe in the 2021–2050 period. In the 2071–2100 period, larger continental influence is predicted by the Conrad index than by the Gorczynsky in Scandinavia area, while the difference between the

two index is the smallest in Central Europe according to ARPÈGE driven and in East-Europe according to ECHAM5 driven RCMs, respectively. The predicted change of the Gorczynsky index is larger than the predicted change of the Conrad index in almost each region in both time periods (*Fig. 5*).

The distinction among the different GCM driven model results is analogous with the differences in the case of the temperature anomaly. The change of the Conrad index value in time is the same than in the case of the Gorczynsky index. Similarly to the Gorczynsky index, the largest Conrad index values are predicted by CNRM in Central, South-East and East Europe, respectively, in 2071–2100. The change of the modeled and measured difference values in time and the spread of the model results (*Table 7*) are also analogous with the Gorczynsky index ones.

Table 6. Space differences of the predicted mean Conrad index C_{mean} in 2021–2050 (top) and 2071–2100 (bottom) for the regions defined in *Table 2*

Conrad index in 2021–2050							
Region	**ARPÈGE** C_{mean}	**CNRM** C_{mean}	**DMI** C_{mean}	**ICTP** C_{mean}	**KNMI** C_{mean}	**MPI** C_{mean}	**SMHCI** C_{mean}
1	27.2	27.2	26.1	27.7	27.8	27.8	28.4
2	22.7	23.0	22.1	21.9	22.0	22.0	21.6
3	10.7	11.0	10.2	10.6	10.6	10.3	10.0
4	**26.3**	26.7	26.4	27.1	27.1	26.3	26.3
5	29.4	29.1	28.9	28.0	28.1	27.8	27.3
6	34.9	34.6	32.3	32.1	32.1	32.0	31.9
7	38.4	38.1	36.7	35.0	35.4	34.7	34.4
Conrad index in 2071–2100							
Region	**ARPÈGE** C_{mean}	**CNRM** C_{mean}	**DMI** C_{mean}	**ICTP** C_{mean}	**KNMI** C_{mean}	**MPI** C_{mean}	**SMHCI** C_{mean}
1	30.7	30.8	29.8	31.3	31.7	32.0	32.3
2	26.2	27.9	24.9	22.5	23.5	22.4	22.3
3	11.0	12.3	10.7	10.4	10.5	9.9	9.6
4	23.8	24.6	23.7	24.0	24.2	23.7	22.4
5	31.9	34.5	30.6	27.2	28.6	26.5	26.7
6	39.1	39.5	35.7	33.7	34.4	34.2	34.5
7	40.6	41.1	37.4	35.0	35.9	33.8	34.14

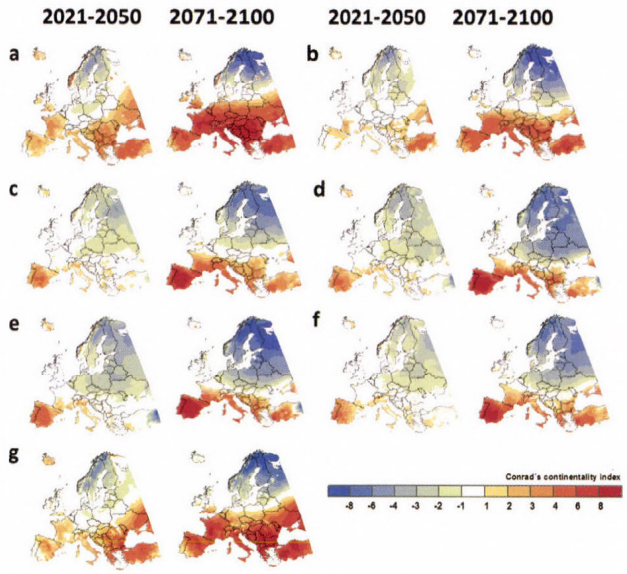

Fig. 5. Predicted changes of the Conrad indexes (a) CNRM, (b) DMI, (c) KNMI, (d) MPI, (e) SMHIRCA, (f) ICTP, and (g) ARPÈGE.

3.4. Central Europe

The continentality in Central Europe is detailed by the ALADIN-Climate/CZ (hereinafter referred to as CHMI) model with higher (10 km) horizontal resolution. The model has same dynamical core as CNRM, but they differ significantly in their physical package (*Skalak et al.,* 2008). Its physical package is detailed in *Farda et al.* (2010). CHMI is run in CECILIA domain which focuses on the Czech Republic and its vicinity. The results of simulated and observed Gorczynsky and Conrad indexes are presented in *Figs. 6* and *7*, respectively. *Table 8* shows the mean value and predicted change value of temperature amplitude, Gorczynsky index, and Conrad index, respectively in the 2021–2050 and 2071–2100 periods.

Table 7. The spread of the simulated Conrad index of the models in 2021–2050 (top) and in 2071–2100 (bottom) for the regions defined in *Table 2*

Spread of simulated Conrad index 2025–2050							
	1	**2**	**3**	**4**	**5**	**6**	**7**
ARPÈGE	27.2	22.7	10.7	26.3	29.4	34.9	38.4
CNRM	27.2	23	11	26.7	29.1	34.6	38.1
DMI	26.1	22.1	10.2	26.4	28.9	32.3	36.7
ICTP	27.7	21.9	10.6	27.1	28	32.1	35
KNMI	27.8	22	10.6	27.1	28.1	32.1	35.4
MPI	27.8	22	10.3	26.3	27.8	32	34.7
SMHCI	28.4	21.6	10	26.3	27.3	31.9	34.4
mean	**27.45**	**22.18**	**10.48**	**26.6**	**28.37**	**32.84**	**36.1**
spread	**0.72**	**0.48**	**0.33**	**0.36**	**0.76**	**1.31**	**1.64**
Spread of simulated Conrad index 2070–2100							
	1	**2**	**3**	**4**	**5**	**6**	**7**
ARPÈGE	30.7	26.2	11	23.8	31.9	39.1	40.6
CNRM	30.8	27.9	12.3	24.6	34.5	39.5	41.1
DMI	29.8	24.9	10.7	23.7	30.6	35.7	37.4
ICTP	31.3	22.5	10.4	24	27.2	33.7	35
KNMI	31.7	23.5	10.5	24.2	28.6	34.4	35.9
MPI	32	22.4	9.9	23.7	26.5	34.2	33.8
SMHCI	32.3	22.3	9.6	22.4	26.7	34.5	34.14
mean	**31.22**	**24.24**	**10.62**	**23.77**	**29.42**	**35.87**	**36.84**
spread	**0.86**	**2.17**	**0.87**	**0.68**	**3.02**	**2.42**	**2.98**

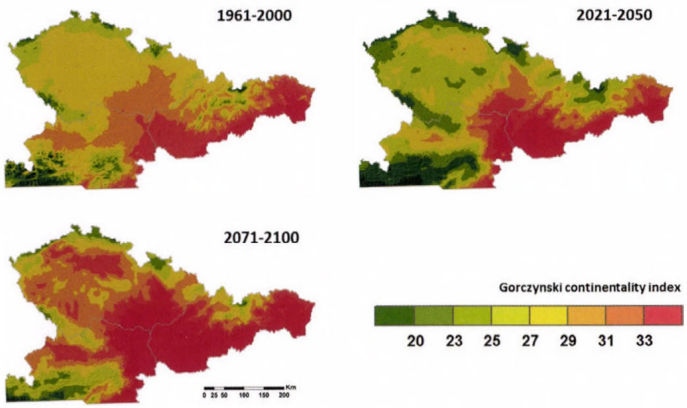

Fig. 6. ALADIN/CZ simulated and higher resolution observed Gorczynsky index in CECILIA domain.

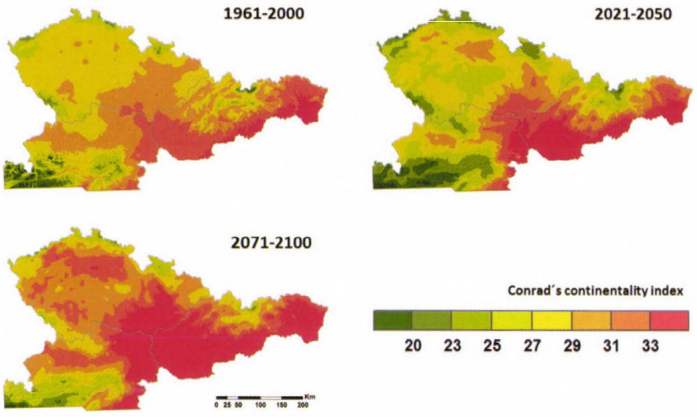

Fig. 7. ALADIN/CZ simulated and higher resolution observed Conrad index in CECILIA domain.

Table 8. The mean value and predicted changes of annual temperature amplitude, Gorczynsky and Conrad continentality indexes, respectively, predicted by the ALADIN-Climate/CZ model for the near and far future time slices, respectively

	ALADIN-CLIMATE/CZ			
	2021–2050		2071–2100	
	T_{MEAN}	T_M–T_E	T_{MEAN}	T_M–T_E
Temperature amplitude	21.3	–0.3	22.8	1.2
Gorczynsky index	27.6	–0.7	31.1	2.7
Conrad index	28.3	–0.6	31.4	2.4

Comparing the CHMI and ENSEMBLES model results, the differences are the smallest between CHMI and ICTP or KNMI values in 2021–2050, while in the further period the distinction is the smallest between the ARPÈGE and CHMI predicted continentality indexes. The predicted change value is negative in the near and positive in the far future, respectively, like in the DMI case. Based on the mean Gorczynsky index, the climate will be transitional maritime according to CHMI in Central Europe, which agrees with the other ENSEMBLES model results with the exception of the CNRM prediction to the 2071–2100 time slice.

The differences between the CNRM and CHMI predicted mean continentality values is 0.8 in the case of both indexes in the near future time slice, while the differences between the Gorczynsky and Conrad indexes are 3.4 and 3.1, respectively, in the far future period. Some factors which could be responsible for these differences are the large/small integrated area, higher/lower resolution, and the differences between the models. CHMI results positive precipitation bias due to high accumulation of snow in Central Europe during late winter and early spring in both of the 50 km and 10 km resolution cases (*Farda et al.,* 2007; *Skalak et al.,* 2008). This wetter feature of precipitation field corresponds well to the negative bias in winter and spring mean temperature. Furthermore, *Farda et al.* (2007) found that the smaller domain size enhances the precipitation due to the unrealistic generation of vertical velocity in the coupling zone of the model which affects directly even the interior of the rather limited domain.

4. Discussion

4.1. Effect of drivers

We found that the drivers have a significant effect on the spread of results. According to the ECHAM5 driven RCMs, the Atlantic Ocean has a strong influence on the surface temperature due to the too zonal large-scale circulation and underestimated sea-ice condition of the ECHAM5-r3 GCM. Thanks to this phenomenon, smaller continentality indexes were predicted by the ECHAM5 driven RCMs than the ARPÈGE forced ones in each regions except in South-Europe in both time periods.

4.2. Effect of model resolution

The higher resolution model provided finer details of the simulated field, but the resolution differences did not play dominant role in the difference from other RCM results. Small differences were found between the results of ARPÈGE 50 km and CNRM 25 km resolution models. The finer resolution ALADIN-Climate/CZ resulted similar results like ITCP or KNMI in the nearer future, while its results were closer to the ARPÈGE simulation in the far future case. The CHMI simulated mean continentality indexes decreased compared to the observed values in the 2021–2050 time period, while increased in the far future slice. The differences between the CNRM and CHMI results probably come from the positive wet bias of CHMI, which is persistent when smaller domain is used.

4.3. Impacts on continentality

Two different continentality indexes (Gorczynsky and Conrad, respectively) were calculated in function of annual temperature anomaly and sinus function of latitude. The mean annual temperature range rises with increasing distance from the ocean and with increasing aridity. Both continentality indexes strongly depend on the annual temperature range, and their spatial differences are well correlated with the space differences of temperature anomaly. The largest continental effect in South-Europe came from the block of maritime airmass caused by the Pyrenees. The continentality indexes decreased with time only in Scandinavia region. This phenomenon can be explained with the assumption of the melting of sea-ice which causes larger SST. Despite the fact that the maximum internal variability of RCMs is in the South-East European region (*Sanchez-Gomez, E. et al.,* 2009), the largest model variability was in the Scandinavia region in each model case. This maximum variability affected by the natural variability is caused by SST and sea-ice condition.

5. Conclusion

The future continental climate is simulated by applying two different continentality indexes: the Gorczynsky and Conrad, respectively. Both of them indicate the continentality as a function of the annual mean temperature anomaly and a sinus function of the latitude angle. The largest difference between their index values is caused by the boundary condition which is applied in the Conrad approach to avoid the insensible negative continentality values in lower latitudes. In our simulation, the isoline flows near meridionally only in East-Europe, and it flows to eastward direction in South-East and South Europe, respectively. The greatest change with time slice in isoline direction is in Scandinavia, where the climate becomes more balanced maritime despite the resulted larger model variability.

The core message of our research is whether Central Europe becomes more continental or maritime according to the A1B RCM scenarios in the 21st century?

The climate of Central Europe is predicted to be transitional maritime according to the mean Gorczynsky index of RCMs with exception of CNRM in the further time slice. This result might be explained by the experience that CNRM overestimates the monthly maximum temperature and underestimates the precipitation in Central Europe. The simulated continental influence will diminish compared to the observed state according to the ECHAM5 driven RCMs in Central Europe in both time slices. Although the boundary of maritime and continental climate run along east Austria, south-east Czech Republic, and mid-Slovakia according to the CHMI detailed Gorczynsky index, its mean value is below the continental boundary.

Acknowledgements: This research was supported by the Czech Grant Agency in the frame of the project: Global and regional climate model simulations in Central Europe in the 18th-20th centuries in comparison with observed and reconstructed climate, GACR P209/11/0956. Pavel Zahradníček was supported by project InterSucho (no. CZ.1.07/2.3.00/20.0248). We are thankful for the E-OBS data set from the EU-FP6 project ENSEMBLES (http://www.ensembles-eu.org) and the data provided by the ECA&D project (http://www.eca.knmi.nl). Data for Central Europe was performed within the CECILIA project, funded by the European Commission's 6th Framework Programme under contract number 037013.
We also would like to thank to the anonymous reviewers for their comments and suggestions.

References

Conrad, V. and *Pollak, L.W.*, 1950: Methods in climatology. 2nd edition. Harvard university press, Cambridge, Massachusetts.

Christensen, J.H., Christensen, O.B., Lopez, P., Van Meijgaard, E., and *Botzet, M.,* 1996: The HIRHAM4 regional atmospheric model. Scientific Report 96-4, The Danish Meteorological Institute, Copenhagen, Denmark.

Christensen, J.H., Boberg, F., Christensen, O.B., and *Lucas-Picher, P.,* 2008: On the need for bias correction of regional climate change projections of temperature and precipitation. *Geophys. Res. Lett. 35*, L20709.

Currey, D.R., 1974: Continentality of Extratropical Climates. *Ann. Ass. Amer. Geograph. 64,* 268–280.

Déqué, M., Rowell, D. P., Lüthi, D., Giorgi, F., Christensen, J.H., Rockel, B., Jacob, D., Kjellström, E., de Castro M., and *van den Hurk, B.,* 2007: An intercomparison of regional climate simulations for Europe: assessing uncertainties in model projections. *Climate Change* 81 (Suppl. 1), 53–70.

Déqué, M., Somot, S., Sanchez-Gomez, E., Goodess, C.M., Jacob, D., Lenderink G., and *Christensen, O.B.*, 2012: The spread amongst ENSEMBLES regional scenarios: regiona climate models, driving general circulation models and interannual variability. *Clim. Dynam. 38*, 951–964.

Dirscoll, D.M. and *Yee Fong, J.M.,* 1992: Continentality: A basic climatic parameter re-examined. *Int. J. Climat. 12*, 185–192.

Dosio, A. and *Paruolo, P.*, 2011: Bias correction of ENSEMBLES high-resolution climate change projections for use by impact models: Evaluation on the present climate. *J. Geophys. Res. 116*, D16106.

Farda, A. Štěpánek, P., Halenka, T., Skalák, P., and *Beld, M.,* 2007: Model ALADIN in climate mode forced with ERA40 reanalysis (course resolution experiment). *Meterologický časopis 10*, 123–130.

Farda, A., M. Dequé, S. Somot, A. Horányi, V. Spiridonov and *H. Tóth*, 2010: Model ALADIN as regional climate model for central and eastern Europe. *Stud. Geophys. Geod. 54*, 313–332.

Gibelin, A.-L., and *Déqué, M.*, 2003: Anthropogenic climate change over the Mediterranean region simulated by a global variable resolution model. *Clim. Dynam. 20*, 327–339.

Giorgi, F. Bi, X., and *Pal, J.S.,* 2004: Mean, interannual variability and trends in regional climate change experiment over Europe. I. Present-day climate (1961-1990). *Clim. Dyn*am. *22*, 733–756.

Gorczynsky, L., 1922: The calculation of the degree of continentality. *Mon. Weather Rev. 50*, 370.

Hasselmann, K., 1976: Stochastic climate models. Part I: Theory. *Tellus 28*, 473–485.

Haylock M.R., Hofstra, N., Klein Tank, A.M.G., Klok, E.J., Jones P.D., and *New, M.,* 2008: A European daily high-resolution gridded data set of surface temperature and precipitation for 1950–2006, *J. Geophys. Res. 113*, D20119.

Hewitt, C.D. and *Griggs, D.J.*, 2004: Ensembles-based predictions of climate changes and their impacts. *Eos Trans. AGU* 85, 566.

Hofstra, N., M. New, C. McSweeney, 2010: The infulence of interpolation and station network density on the distributions and trends of climate variables in gridded daily data. *Climate Dynam. 35*, 841–858.

Holmlund, P. and *Schneider, T.*, 1997: The effect of continentality on glacier response and mass balance. *Ann. Glaciology 24*, 272–276.

Jacob, D., 2001: A note to the simulation of the annual and inter-annual variability of the water budget over Baltic Sea drainage basin. *Meteorol. Atmos. Phys. 77*, 61–73.

Johansson, O.V., 1926: Uber die asymmetrie der meteorologischen Schwankungen. In.: Soc. Sci. Fennica, Commentationes Phys. Math., 3, 1ff

Kjellström, E., L. Bärring, S. Gollvik, U. Hansson, C. Jones, P. Samuelsson, M. Rummukainen, A. Ullerstig, U. Willén and *K. Wys*, 2005: A 140-year simulation of European climate with the new version of Rossby Central regional atmospheric climate model (RCA3). *SMHI Reports Meteorology and Climatology 108*, SMHI, SE-60176. Norrköping, Sweden.

Kjellström, E., G. Nikulin, U. Hansson, G. Strandberg and *A. Ullersting*, 2011: 21st century changes in the European climate: uncertainties derived from an ensemble of regional climate model simulations. *Tellus 63A*, 24–40.

Klein Tank, A.M.G., J. B. Wijngaard1, G. P. Können, R. Böhm, G. Demarée, A. Gocheva, M.Mileta, S. Pashiardis, L. Hejkrlik, C. Kern-Hansen, R. Heino, P. Bessemoulin, G. Müller-Westermeier, M. Tzanakou, S. Szalai, T. Pálsdóttir, D. Fitzgerald, S. Rubin, M. Capaldo, M. Maugeri, A. Leitass, A.Bukantis, R. Aberfeld, A. F. V. van Engelen, E. Forland, M. Mietus, F. Coelho, C. Mares, V.Razuvaev, E. Nieplova, T. Cegnar, J. Antonio López, B. Dahlström, A. Moberg, W. Kirchhofer, A. Ceylan, O. Pachaliuk, L. V. Alexander and P. Petrovic' 2002: Daily dataset of 20th century surface air temperature and precipitation series for the European climate asseessment. *Int. J. Climatol. 22*, 1441–1453.

Lenderink, G., B. van den Hurk, E. van Meijgaard, A. van Ulden and *H. Cuijpers*, 2003: Simulation of present-day climate in RACMO2: first results and model developments. *Technical Report TR-252*, Royal Netherlands Meteorological Institute.

van der Linden, P. and *Mitchell, J.F.B.* (eds.) 2009: ENSEMBLES: Climate Change and its Impacts: Summary of research and results from the ENSEMBLES project. Met Office Hadley Centre, FitzRoy Road, Exeter EX1 3PB, UK.

McBoyle, G.R., and *Steiner, D.*, 1972: A factor-analytic approach to the problem of continentally. *Geografiska Annaler Series* A, *Physical Geography, 54*, 12–27.

Meier, H.E.M., Höglund, A., Döscher, R., Andersson, H., Löptien, U., and *Kjellström, E.*,2011: Quality assessment of atmospheric surface fields over the Baltic Sea from an ensemble of regional climate model simulations with respect to ocean dynamics. *Oceanologia 53*, 193–227.

Mikolaskova, K., 2009: A regression evaluation of thermal continentality. *Geografie 4*, 350–361.

Nakicenovic, N. and *Swart, R.*, 2000: Special Report on Emissions Scenarios: A Special Report of Working Group III of the Intergovernmental Panel on Climate Change, Cambridge UK: Cambridge University Press.

Nikiforova, T., Savytskyi, M., Limam, K., Bosschaerts, W., and *Belarbi, R.*, 2013: Methods and results of experimental researches of thermal conductivity of soils. *Energy Procedia 42*, 775 – 783.

Placová, E. and *Kyselý, J.*, 2010: Evaluation of daily temperatures in Central Europe and their links to large-scale circulation in an ensemble of regional climate models. *Tellus 63A*, 763–781.

Rowell, D.P. and *Zwiers, F.W.*, 1999: The global distribution of sources of atmospheric decadal variability and mechanisms over the tropical Pacific and southern North America. *Clim. Dynam. 15*, 751–772.

Sanchez-Gomez, E., Somot, S., and *Déqué, M.*, 2009: Ability of an ensemble of regional climate models to reproduce weather regimes over Europe-Atlantic during the period 1961-2000. *Clim. Dynam. 33*, 723–736.

Skalak, P., Štěpánek, P., and *Farda, A.*, 2008: Validation of ALADIN-Climate/CZ for present climate (1961-1990) over the Czech Republic. *Idojaras 112*, 191–201.

Sládek, I., 2005: Návrh nové míry kontinentality klimatu. *Fyzickogeografický sborník, 3*,. 144–147. (In Slovak)

Solomon, S., Qin, D., Manning, M., 2007: Technical Summary. In: (Eds.: *S. Solomon, D. Qin, M. Manning, Z. Chen, M. Marquis, K. B. Averyt, M. Tignor* and *H. L. Miller.*) Climate Change 2007: The Physical Science Basis. Contribution of Working Group I to the Fourth Assessment Report of the Intergovernmental Panel on Climate Change. Cambridge University Press, Cambridge, United Kingdom and New York, NY, USA.

Štěpánek, P., Zahradníček, P., Brázdil, R., and *Tolasz, R.*. 2011a: Metodologie kontroly a homogenizace časových řad v klimatologii Český hydrometeorologický ústav: Praha. (in Czech).

Štěpánek, P., Zahradníček, P., and *Huth, R.,* 2011b: Interpolation techniques used for data quality control and calculation of technical series: an example of a Central European daily time series. *Időjárás 115*, 87–98.

Štěpánek, P., Zahradníček, P., and *Farda, A.,* 2013: Experiences with data quality control and homogenization of daily records of various meteorological elements in the Czech Republic in the period 1961–2010. *Időjárás 117*, 123–141.

Wilby R.L., Wigley, T.M.L., Conway, D., Jones, P.D., Hewitson, B.C., Main, J., and *Wilks, D.S.,* 1998: Statistical downscaling of general circulation model output, a comparison of Methods. *Water Resour. Res. 34*, 2995–3008.

IDŐJÁRÁS

Quarterly Journal of the Hungarian Meteorological Service
Vol. 119, No. 4, October – December, 2015, pp. 537–555

Estimation of solar and wind energy potential in the Hernád Valley

Károly Tar[1,2*], **Andrea Kircsi Bíróné**[1], **Blanka Bartók**[3], **Sándor Szegedi**[1], **István Lázár**[1], **Róbert Vass**[2], **Attila Bai**[4], and **Tamás Tóth**[1]

[1]*Department of Meteorology, University of Debrecen, Egyetem tér 1, H-4010 Debrecen, Hungary*

[2]*Institute of Tourism and Geography, College of Nyíregyháza, Sóstói út 31/b, H-4400 Nyíregyháza, Hungary*

[3]*Department of Geography in Hungarian, Babes-Bolyai University, Clinicilor 5-7, 400006 Cluj-Napoca, Romania*

[4]*Faculty of Applied Economics and Rural Development, University of Debrecen, Böszörményi u. 138, H-4032 Debrecen, Hungary*

** Corresponding authors E-mail: tarko47@gmail.com*

(Manuscript received in final form October 3, 2014)

Abstract—This paper focuses on the climatic conditions of the Hernád Valley with the purpose of exploring on what level the utilization of wind and solar energy is advanced or detained in the micro-region. For determination of wind and solar energy potential, an automatic weather station was mounted in the Hungarian section of the Hernád Valley located on a small hill 500 meters west from the settlement of Hidasnémeti.

Available long-term surface global radiation data do not represent our study area on regional scale. For this reason, daily global radiation datasets of the nearest weather station, the airport of Kosice has been used for the analyses. Diurnal and annual variation and spatial pattern of global radiation have been examined by combination of statistical analyses and geo-information/GIS methods.

Other important aim of the research is to describe the spatial characteristics of the wind energy potential related to orography in the Hernád Valley. Diurnal courses of different statistical parameters and the spatial pattern of wind speeds has been investigated on the base of our measured data. Since these data are not continuous, relationships between the diurnal average wind speeds of Kosice and Hidasnémeti were examined also. An attempt has been made to complete our diurnal average wind speed database by linear regression.

Finally, the social and economic conditions regarding solar and wind energy utilization are mentioned shortly in the paper.

Key-words: Hernád Valley, solar energy potential, wind profile, wind energy potential

1. Introduction

The Department of Meteorology, University of Debrecen carried out the research of the climatic and social-economic conditions of Hernád Valley in the frame of a scientific project between 2009 and 2012. The aim was to find optimal area for wind and solar energy, as well as biomass utilization. Our purpose is to work out a model wherein the complex evaluation of natural and social-economic conditions and effects can result in a sustainable and out-of-conflict land use, after all. The results of the research will be useful to work out a regional improvement strategy based on the use of renewable energy sources to help local decision process. Most important results of investigations on wind and solar climate and energy are summarized in this paper. Local conditions can serve as a good base for further development of solar energy utilization in the region. Solar energy can be introduced in some new fields like ecologic and silvicultural applications. Our examinations have showed also that in spite of temporal fluctuations, utilization of wind energy in the study area can be expedient and effective, especially in the case of application of low starting speed wind turbines. Citizens' opinion about instruments of utilization of solar and wind energy is positive, and they are open for such initiatives. Well prepared projects can be successful and can contribute to the development of the economy of the region.

This research intends to focus on the climatological conditions of the Hernád Valley micro-region with the purpose of exploring on what level they advance or detain the utilization of solar and wind energy.

As a first step, the exploration of the climatological endowments of the selected area based on climatological observations was carried out. It made possible the calculation of indexes, which describe the connections between weather types and the amount of utilizable wind and solar energy on one hand, the elaboration of a model, that helps the allocation of wind turbines and refining of relations, as well as describes the variations of wind speeds with height; and selection of plants optimal for biomass production in a given micro-region on the other hand. Social-economic studies focused on financial benefits and cost-efficiency indexes have been revealed, as well as social acceptance of renewable energy sources have been surveyed.

For determination of wind and solar energy potential, an automatic weather station was established in the Hungarian section of Hernád Valley on a small hill 500 meters west from the settlement of Hidasnémeti at N 48°30' and E 21°13' at a height of 175 meters above sea level (*Fig. 1*). The automatic weather station was mounted on a 20-meter high measurement mast which was equipped with a wind direction sensor at a height of 10 meters and two anemometers at heights of 10 and 20 meters among other instruments.

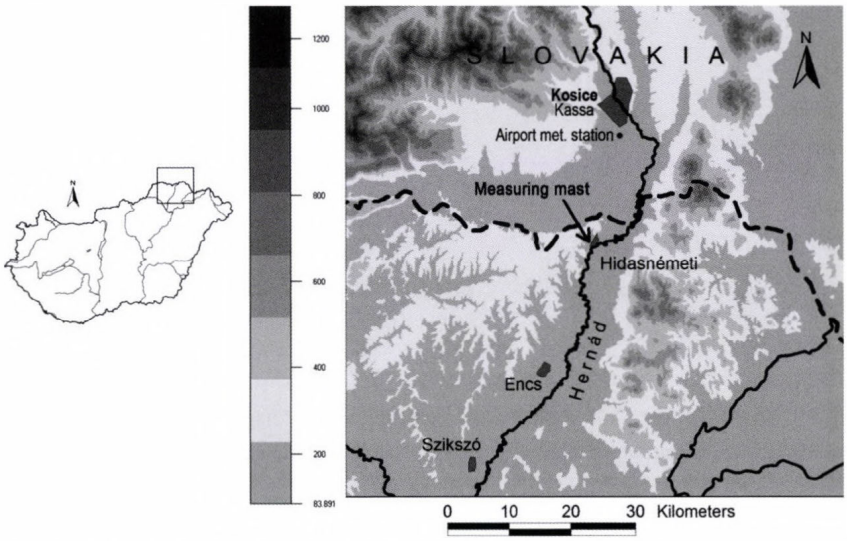

Fig. 1. Geographical situation of the meteorological measurements.

To survey the solar energy potential of the Hernád Valley, it is important to know the temporal and spatial pattern of global radiation of its region. It is determined by the Sun and the geometry of the relief; however, actual atmospheric conditions have an important effect on the amount of incoming solar radiation as well. Available surface global radiation data do not represents our study area on regional scale. For this reason, daily global radiation datasets of the nearest weather station, the airport of Kosice (48.667°N, 21.217°E, 231 m a.s.l.) have been used for the analyses.

Datasets have gone under statistic-climatological analyses, main statistic parameters have been determined, wind speed and direction frequency distributions have been prepared for both heights; hourly and diurnal average values of the parameter in the Hellman wind profile equation have been determined in the first stage of our wind climatological research. On this base, average diurnal courses and diurnal average wind speeds for levels higher than the measurements levels have been calculated, what is decisive from the aspect of the amount of potential wind energy. A statistic definition has been worked out for diurnal average specific wind power of a day of any period of time. Its comparative examination has been carried out as well.

However, the survey of wind potential of the Hernád Valley requires spatial extrapolation as well. The model used for this purpose is not our development, but there are not any examples for Hungarian adaptations of the WindSim 5.1 EV model yet. The model has a modular structure, and it generates the spatial distribution of average wind speeds influenced by orography in successive steps, what determines the prospective energy production of the chosen wind energy utilizing instrument practically. Turbulence parameters

influenced by orography and spatial patterns of wind speeds weighted on the base of average wind direction distribution have been determined for the Hernád Valley using both the results of our measurements and the one-year-long dataset from the airport of Kosice, eventually. Wind potential maps can be generated for any heights up to 200 meters. They can help the selection of optimal sites for wind energy utilization.

2. Examination of solar energy potential in the Hernád Valley

To determine the solar energy potential of the Hernád Valley the first step is to gain information on temporal and spatial pattern of global radiation of that region. Since there is not any Hungarian long-term surface radiation measurement stations in the environment of our study area, diurnal global radiation datasets of the nearest weather station, the airport of Kosice (Slovakia) have been used for the analyses.

Besides the pointwise measurements, ArcGIS geoinformation software has been used in order to analyze the spatial distribution of solar radiation in the Hernád Valley. In this case, the required input parameters have been determined using data measured there.

Changes in the global radiation are determined mainly by the geographical latitude. The other affecting factor is the air circulation having impact via cloudiness, amount of sunny hours and last but not least via transparency of the atmosphere (different air masses). Orography can also strongly modify the spatial and temporal pattern of global radiation. GIS programs are able to handle the surface characteristics with very high accuracy, but their weakness is that the meteorological conditions (cloudiness, water vapor content, etc.) are integrated indirectly using parameterizations (see Section 2.2).

Evaluation of global radiation data provides essential information for planning and economic analyses of solar energy utilization projects in the Hernád Valley. Examinations can be carried out for any point of the region by combination of statistical analyses and geoinformation methods.

2.1. Diurnal and annual courses of global radiation

Diurnal and annual courses of global radiation have been examined using the one-year-long dataset of the weather station of the airport of Kosice, located 25 km north from the settlement of Hidasnémeti. The raw database covers the period between May 2009 and April 2010, the hourly global radiation data are given in J/cm^2 (1 J/cm^2 = 2.778 W/m^2 hour). In the followings, the unit of W/m^2 will be used. Global radiation has a nearly symmetric curve with a maximum in June-July during the year. The curve reaches its minimum in the winter period in December, when the maximum is 367 W/m^2. There are higher maximal values in January and February, with 392 W/m^2 and 483 W/m^2, respectively. Values

increase gradually in the spring reaching 714 W/m^2 in March and even 900 W/m^2 in May. There is a gradual decrease in the autumn months, although values are a bit lower than in the spring: 739 W/m^2 in September, while 422 W/m^2 in November. Highest values of global radiation occur in the afternoon, in the summer months with maxima over 800 W/m^2 and average over 435 W/m^2 between 9 and 15 UTC. Annual course of global radiation has reached its maximum in July with 933 W/m^2 during the studied period.

Diurnal curves show a symmetric distribution also with a maximum at noon independently from the seasons. Only the amplitudes of the curves are different according to the seasons (*Fig. 2*). Minima occur in December with 143 W/m^2. Intensities reach 21 W/m^2 at 9 UTC in the morning and reach 64 W/m^2 by 15 UTC. Highest intensities occur at the summer solstice in June, when it reaches 609.3 W/m^2 at noon, 202.7 W/m^2 in the morning (6 UTC), and 109.7 W/m^2 and late afternoon (18 UTC).

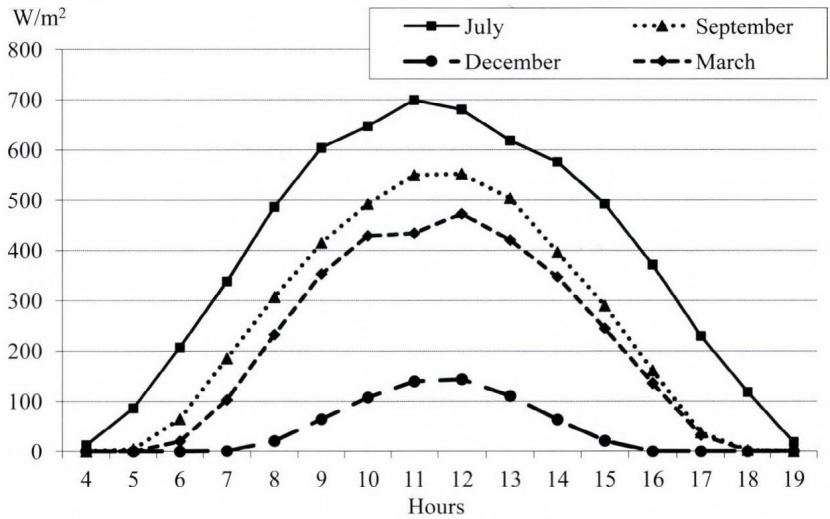

Fig. 2. Diurnal course of hourly average global radiation (W/m^2) at the weather station of Kosice during the 2009–2010 period.

Hourly values of global radiation are dependent on synoptic conditions which can change hour by hour significantly. Annual course of diurnal amounts of global radiation are presented in *Table 1*. It can be observed that values appear in 4 categories in the winter months, while they scatter in a much wider range in the summer period.

Table 1. Relative frequency of diurnal amounts of monthly global radiation (%) at the weather station of Kosice of the 2009–2010 period

W/m^2	Jan	Feb	Mar	Apr	May	June	July	Aug	Sept	Oct	Nov	Dec
0–500	22.6	3.6								6.5	**53.3**	32.3
501–1100	**51.6**	39.3		3.3					3.3	**35.5**	26.7	**54.8**
1101–2200	25.8	**46.4**	16.1	10.0	3.2	6.7		6.5	6.7	29.0	13.3	12.9
2201–3300		10.7	29.0	16.7	6.5	6.7	3.2	6.5	10.0	19.4	6.7	
3301–4400			**48.4**	23.3	3.2	16.7	12.9	19.4	**40.0**	9.7		
4401–5500			6.5	10.0	19.4	13.3	16.1	22.6	33.3			
5501–6600				**26.7**	29.0	**26.7**	16.1	**38.7**	6.7			
6601–7700				10.0	**32.3**	16.7	**38.7**	6.5				
7701–8800					6.5	13.3	12.9					

2.2. Examination of the spatial pattern of global radiation

On the base of point-like measurement data, high resolution radiation maps of the region have been elaborated using geoinformatic tools (Esri ArcGIS Solar radiation module). As the global radiation is determined by many factors, the module contains various setting options. One of the most important factors is the aspect and slope derived from the characteristics of the surface. This kind of information can be obtained from the input digital elevation model (DEM). The program recognizes the geographical latitude of the area even at the moment of loading the DEM, furthermore, the inclination angle of solar radiation can also be determined. The next step contains the time settings. The most important parameter is the sequence of the day in the given year. Based on this parameter, the inclination angel of the radiation, the way length of solar beam in the atmosphere, and the astronomical duration of sunshine can be determined. All these parameters of radiation presented above can be calculated exactly. In the following step, the input parameters refer to the atmospheric conditions like cloud cover, humidity, opacity, etc. Regarding these parameters in the module two, values can be adjusted, namely the proportion of diffuse radiation and the transmissivity of the atmosphere (τ). The values of proportion of diffuse radiation was taken from the PVGIS dataset (*http://re.jrc.ec.europa.eu*). The parameterization of transmissivity is elaborated based on measured global radiation values. The monthly radiation values are classified in function of standard deviation (σ) into three categories, namely $M \pm \sigma$ interval concerning situations with average radiation values, $M+2\sigma$ for situation with high values, and $M-2\sigma$ interval including the

situation of low global radiation. In order to determine a monthly τ parameter, an approximate τ was determined for each category weighted with the number of cases of the given category. In this way, an empirical τ parameter was calculated separately for each month (*Bartók et al.,* 2011).

Introducing the DEM of the region, the proportion of diffuse radiation, and the empirical τ parameter into the GIS Solar radiation module, high resolution global radiation maps were elaborated for different periods. Results regarding the period of May-August (warmest four months of the year) are presented in *Fig. 3*. Statistics of global radiation income (sum) of the region for the period between May and August are the following. The average is 501 kW/m^2, the minimum is 438 kW/m^2, the maximum is 563 kW/m^2, and the empiric standard deviation is 11 kW/m^2, respectively. The high resolution of the map makes it possible to evaluate radiation conditions of slopes of different expositions.

Evaluation of data of incoming global radiation provides essential information for planning and economic analyses of solar energy utilization projects planned in the Hernád Valley. Examinations like presented above can be carried out for any point of the region, where utilization of solar energy takes place by combination of statistical analyses and geoinformation methods. It is reasonable, since local features, especially orography, can modify the spatial and temporal pattern of global radiation remarkably.

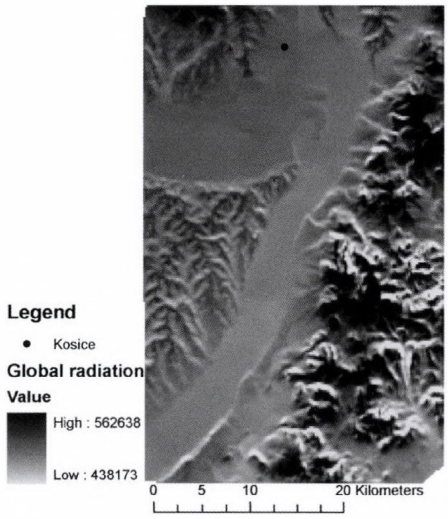

Fig. 3. Total global radiation (W/m^2) in the Hernád Valley for the period between May and August.

3. Determination of wind energy potential in the Hernád Valley

Besides the wind climatological research, other important aim of the research program was to describe the spatial characteristics of the wind energy potential related to orography in the Hernád Valley.

The data logger mounted on the measurement mast carried out measurements in every 10 seconds and calculated averages for 10-minute intervals. Resolution of the anemometer was 0.1 m/s, while wind directions have been recorded with a resolution of 1°. Measurements lasted from April 23, 2010 to April 27, 2012 with a time span of 24 month on the whole. Datasets had been tested before the statistical analyses and modeling. Time series have proved to be discontinuous due to rigorous weather conditions in the winter months. There have been lacks of data in December – February in the winter of 2010–2011, and once in July 2010. Lacks of data have not been complemented by statistical methods. This way we have gained wind data for 67% of the studied period.

3.1. Diurnal courses of different statistical parameters of wind speeds

Daily courses by 10-minute intervals of the average wind speeds, its standard deviation, variation coefficient, and the parameter in the Hellmann's wind profile (Eq. (1)) for the 525 days represented with wind measurement data of the before mentioned measurement period have been calculated for both heights. Mean diurnal course of wind speeds are presented in *Fig. 4*. Its maximum occurs between 13 and 15 UTC at both heights, while minima occur before dawn (3–4 UTC), what is in accordance with the basic characteristics of the wind climate of Hungary. Diurnal fluctuation is 1.6 m/s at 10 meters and 1.4 m/s at 20 meters, what refers to less changeable nature wind speeds of the higher level. Differences in the averages of the two levels do not exceed 0.4 m/s, with smaller differences in the day. Averages for the whole period are 3.2 and 3.4 m/s, respectively. Diurnal courses of variation coefficients (standard deviation/ average) are presented in *Fig. 5*. According to this, variability decreases in the day, especially at 10 meters.

Measurements carried out at two heights makes the determination of the α parameter possible in the equation of Hellmann:

$$\frac{v_2}{v_1} = \left(\frac{h_2}{h_1}\right)^{\alpha}, \tag{1}$$

where v_1 stands for the wind speed measured at height h_1, while v_2 is the wind speed at height h_2. The actual value of parameter α is a function of the roughness of the surface and the equilibrium conditions of the air near the

surface mainly. Due to the latter one it is temperature-dependent, therefore, it has a diurnal and seasonal course. Using α, wind speeds at higher levels can be estimated on the base of wind speeds measured at a given height.

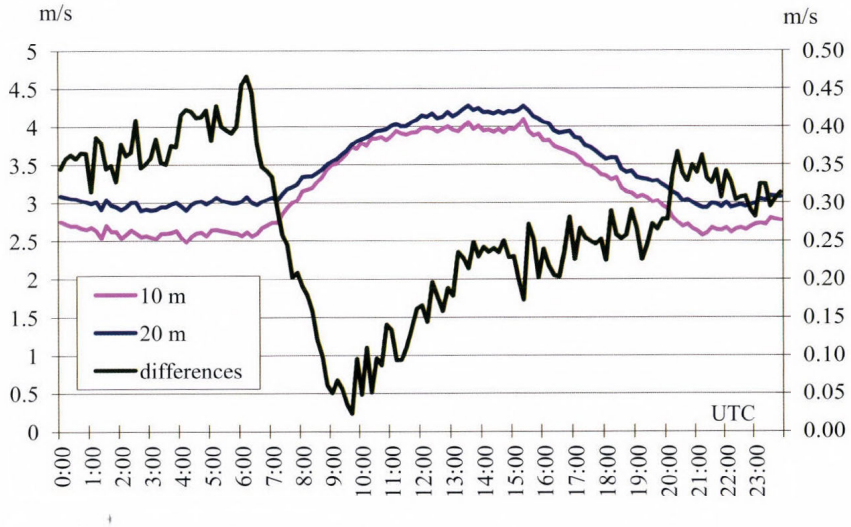

Fig. 4. 10-minute diurnal course of the average wind speeds and their differences.

Fig. 5. 10-minute diurnal course of the variation coefficient of wind speeds.

„Momentary" values of parameter α have been calculated from 10-minute wind speed averages at 10 and 20 meters using Eq. (1) for each day first, then averages for the points of time have been calculated. Diurnal course of parameter α follows the diurnal course of differences in hourly average wind speeds between the 10 and 20 meters levels, namely its value is raised between 4 and 6 in the dawn. Its average is 0.22, what is close to the value (0.25) proposed for calculations for the whole country (*Dobi* and *Mika*, 2007).

As it was mentioned before, α is temperature dependent via equilibrium conditions of the atmosphere. It means that low temperatures near the ground (atmospheric stability) leads to high values of α, while high temperatures close to the surface (atmospheric instability) cause low values of α (*Radics*, 2003). Its values are higher in the night according to other studies also (*Tar*, 2004, 2007), but its diurnal case is more regular than in our case: it can be considered as constant with a fluctuation of ± 0.05 from 21 to 6 UTC, while it decreases from 6 to 12–13 UTC and starts increasing later in the day. Fig. 6 shows a different diurnal course which could not be explained yet. It might be caused by the effect of orography or asymmetry of our data base (less winter days), or even data error cannot be excluded. To solve the problem, further examinations are required into this issue.

More regular diurnal course can be approached using hourly averages of the parameter. In such case, hourly average wind speeds for 10 and 20 meters have to be determined. After that, hourly average wind speeds for higher levels can be calculated with a better chance by Eq. (1). Diurnal course of hourly averages of wind speeds at heights of 20, 40, 60, and 80 meters have been calculated from 10-meter averages using the hourly values of the parameter. Results are presented in *Fig. 5* as well.

Comparison of values measured at 20 meters and values calculated for that height by the before mentioned method provide some information about the error of the Hellmann model. It can be seen that calculated values are higher by 0.1–0.4 m/s in each hour (0.2 m/s on average), what is 6.2% of the diurnal mean value (3.2 m/s). Higher differences occur between 1 and 7 UTC.

According to other authors and our previous examinations carried out in different parts of Hungary (*Kircsi* and *Tar*, 2008; *Tar*, 2009), there is a change in the average diurnal course of wind speeds at a height between 60 and 80 meters. Diurnal course is similar to that presented in *Fig. 4* at lower heights: it has a strong maximum at 13–14 UTC and a minimum in the night. At the same time there is an expressed minimum over that level in the early afternoon. Consequently, there have to be a so-called inflexion height, where diurnal course of (average) wind speeds is random. This hypothesis has been justified by statistical analyses. The inflexion height can be found at 50 meters at the weather stations examined so far (*Tar,* 2009). Unfortunately, inflexion height cannot be identified in *Fig. 6*. The reason for this requires further studies as well.

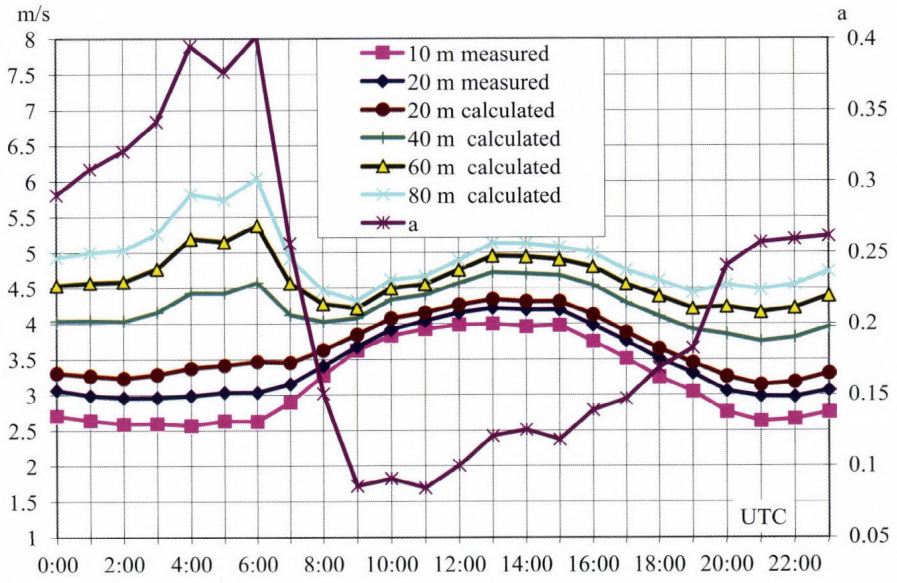

Fig. 6. Hourly average diurnal courses of the wind speeds measured and calculated for different heights and average diurnal course of the Hellmann exponent (α).

3.2. Examination of the spatial pattern of wind speeds

Speed of the air flowing over a solid surface is effected by internal and external friction, orography roughness of the surface, and artificial surface obstacles among other forces. In the case of regions with complex surface, models based on CFD analyses are used in engineering most frequently for revealing spatial patterns of wind speeds.

For wind potential survey of the Hernád Valley, the EV version of WindSim 5.1 software developed by the Norwegian VECTOR AS has been used. It is a wind farm planning tool based on computational fluid dynamic (CFD) simulations of wind flows over complex terrain. The core of the software pack is the PHOENICS software, which finite volume code based on solving the incompressible Reynolds-averaged Navier-Stokes equations (RANS) together with a two-equation turbulence model (k-epsilon turbulence model) (*Castro et al.,* 2003*; Lopez et al.,* 2007). This method favored due to their robustness and low computational costs.

The Reynolds averaged Navier-Stokes equations are used to simulate the turbulent flow field in the following way:

– continuity ($i = 1,2,3$):

$$\frac{\partial(u_i)}{\partial x_i} = 0. \tag{2}$$

– Reynolds-averaged Navier-Stokes equation ($i = 1,2,3$):

$$\rho\left(\frac{\partial \overline{u_i}}{\partial t} + \overline{u_j}\frac{\partial \overline{u_i}}{\partial x_j}\right) = -\frac{\partial \overline{p}}{\partial x_i} + \frac{\partial}{\partial x_j}\mu\left(\frac{\partial \overline{u_i}}{\partial x_j} + \frac{\partial \overline{u_j}}{\partial x_i}\right) - \frac{\partial \rho \overline{u_i' u_j'}}{\partial x_j}, \tag{3}$$

where u_i represents the velocity component, ρ is the density, p is the pressure, μ is the dynamic viscosity, and t is the time.

The software approaches the nonlinear dynamic equations describing mass-, momentum-, and energy transport by iteration.

The model has a modular structure and it approaches the spatial distribution of average wind speeds influenced by orography in several steps determining the prospective energy production of the chosen wind energy utilizing instruments practically.

The base of the running of the WindSim model is a digital terrain model. The digital terrain model used in our research has been derived from the SRTM (Shuttle Radar Topography Mission) database. It has been completed by an international consortium led by NGA (National Geospatial-Intelligence Agency) and NASA in February 2000 (*Farr et al.,* 2007). Elevation datasets of the SRTM database contain buildings, forests, and other roughness elements besides orography. For this reason, a roughness height homogeneous in space was given for the running of WindSim model. Roughness increasing effects of surface cover has not been considered in any other forms.

Before the wind climatological examinations, it had been presumable that the valley of the river has a strong effect on air movements in the study area. Northern-northeastern and the opposite southern-southeastern wind directions are the most frequent in the upper part of the Hernád Valley near the Hungarian-Slovakian border. Highest wind energy content belongs to these directions as well; therefore, they are the most important for establishment of wind energy utilization in the region. Turbulence intensity calculated on the base of standard deviation of wind speeds reaches its maximum when winds blow from the 135° SE and 270° W wind direction sectors.

Windenergy potential maps of the Hernád Valley have been generated using WindSim model for 3 heights above the surface (50, 80, and 110 meters). The numeric model has run with a grid number limited in space. The model area expands to 40 km N, E, S, and W from the measurement mast, so it spreads into the Slovakian part of the Hernád Valley. All orographic elements that have an impact on air movements have been taken into consideration from the Eperjes-

Tokaj Mountains on the east side, the ridges over 1,000 meters of the Slovak Ore Mountains in the northwest, the basin of Kosice and the Hernád Valley (*Kircsi,* 2011; *Bíróné Kircsi et al.,* 2011).

Verification of the result maps has not been carried out yet, estimations are not justified, but they can already be used for identification of areas suitable for wind energy utilization.

On the base of spatial distribution of wind speeds of the height of 50 meters it is visible (*Fig. 7a*) that the low laying basin of Kosice and the Hungarian section of the Hernád Valley is in wind shadow, so it is moderately windy. Annual average wind speeds exceed 5 m/s in the region of highest mountain ridges only. Irrespectively of this, the lower part of the Hernád Valley south of the settlement of Encs and the western side of the valley rising toward the Cserehát hills seems to be suitable for wind energy utilization. Highest wind speeds can be found over the peaks near Hejce and Vilmány.

Wind maps generated for heights of 80 and 110 meters are quite similar (*Figs. 7b* and *7c*), however, wind speed averages have not increased remarkably parallel with the height. The Hernád Valley is not the windiest region of Hungary, anyway. Wind potential in the study area makes possible to establish wind turbines with an axis height of about 100 meters at least.

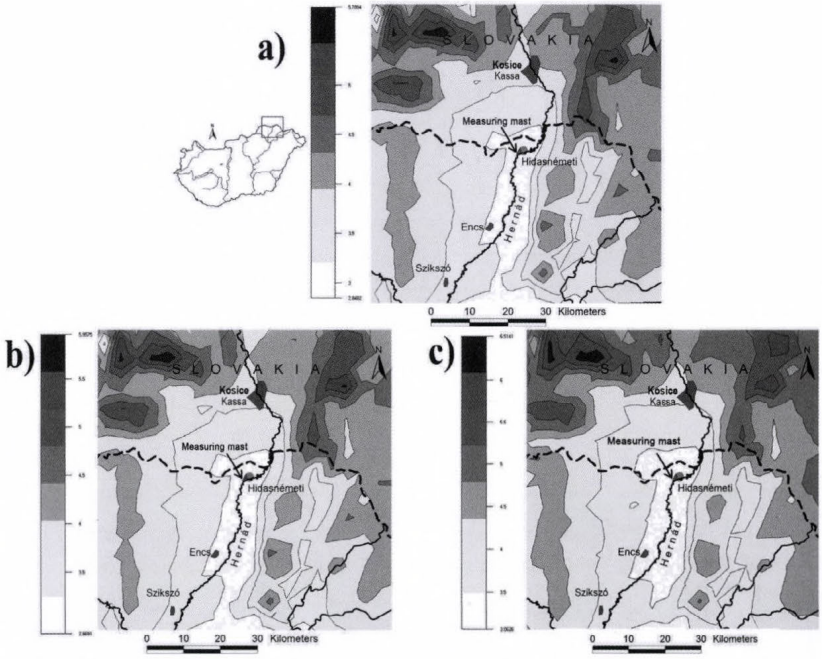

Fig 7. Modeled spatial distribution of wind speeds (m/s) 50 m (a), 80 m (b), and 110 meters (c) above the surface.

3.3. *Relationships between the diurnal average wind speeds of Kosice and Hidasnémeti*

Diurnal average wind speed data of the airport of Kosice for the studied period can be found at *http://ncdc.noaa.gov/oa/ncdc.html*, so they can be compared to our data measured at Hidasnémeti. It is a question anyway whether they are accurate or not. Accuracy of the wind speed datasets available at the homepage have been tested by comparison of base statistics of them and the purchased dataset. Our examinations have proved that they are data from the same weather station (*Tar,* 2012).

Diurnal average wind speed datasets of Kosice have been downloaded from the before mentioned homepage for the period between April 1, 2010 and October 31, 2011, what means 579 days. Our measurements cover 525 days, data for 54 days is missing. An attempt has been made to complete the diurnal average wind speed database by regression for both heights. *Figs. 8* and *9* show the relationships between the datasets available for both stations (525 days) with the two trend lines that fits best (they have the highest correlation index). Unfortunately, there is not any information on the height of the anemometer at the weather station of Kosice, but it is not important from the aspect of regression analyses. Linear trend has been selected for further analyses due to values of correlation index (R^2). T-test has showed that linear correlation coefficients differ significantly from 0. The significant correlation coefficients enable the generation of diurnal mean wind speeds to Hidasnémeti from data of Kosice with the help of regression equations without measurements.

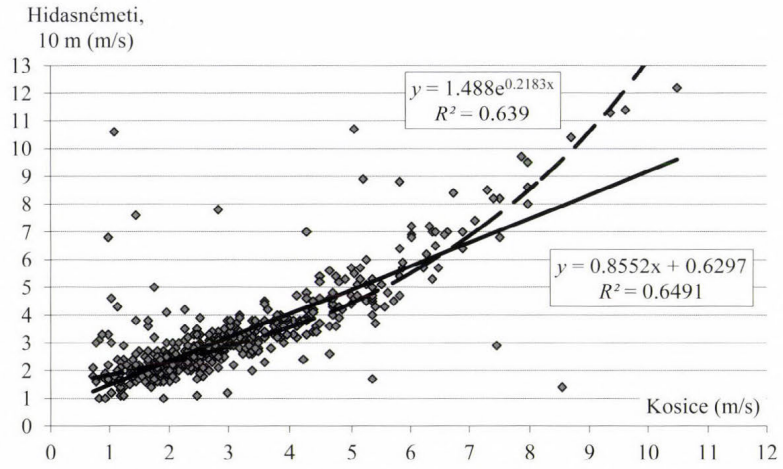

Fig. 8. Regression between datasets of diurnal average wind speeds of Kosice and Hidasnémeti at the height of 10 meters.

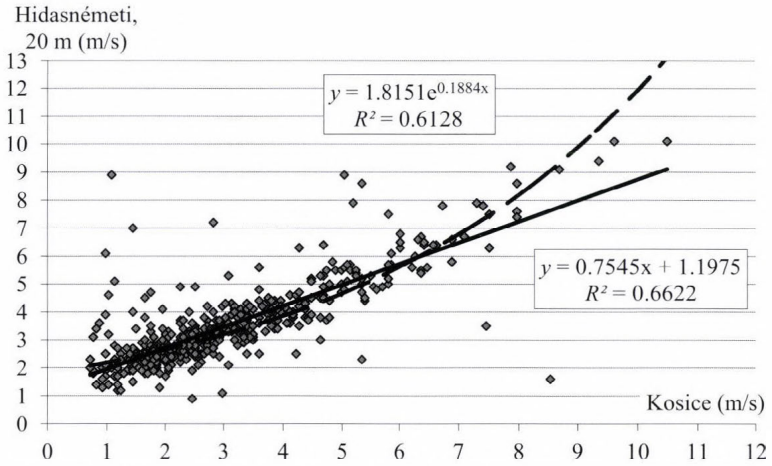

Fig. 9. Regression between datasets of diurnal average wind speeds of Kosice and Hidasnémeti at the height of 20 meters.

As a first step, datasets for 10 and 20 meters of Hidasnémeti have been reconstructed using regression equations $y = 0.8552x + 0.6297$ and $y = 0.7545x + 1.1975$ (where x stands for datasets of Kosice), in order to determine the error of the regression model. Mean relative error at 10 meters is 6.6%, standard deviation is rather high (33.3%), therefore variation coefficient is also high (5.04). Mean relative error at 20 meters is 5.7%, standard deviation is 30%, and variation coefficient is 5.27. Mean relative error is positive in 63.8% and 59.2% of all cases at 10 and 20 meters, what means that the model overestimates.

The most important statistical characteristics of the measured and estimated diurnal average wind speeds are given in *Table 2*. Variability (standard deviation, variation coefficient) of estimated, modeled values is lower than that of measured ones. Values of extremities like range have changed: the latter one has decreased from 11.2 to 8.4 at 10 meters and from 9.2 to 7.4 at 20 meters. Values of skewness and kurtosis show that modeled datasets are more regular, as it can be seen in *Fig. 10*.

The modus of the measured and estimated data falls into the 2–3 m/s interval at both heights according to *Fig. 10*. There is a higher frequency of occurrence by 3 and 2 % in the case of estimated data. It is visible as well, that frequency of values lower than the modus decreases at both heights, while frequency of values higher than the modus increases up to about the 6-7m/s interval together with the change of the coefficient of skewness (*Table 2*). However, homogeneity (χ^2) tests (*Vince,* 1975) have proved that measured and estimated values belong to the same distribution at both heights at a level of 99%.

More detailed results on the wind climatology of the study area can be found in *Tar* (2011a, b) and *Tar et al.* (2011).

Table 2. The most important statistical characteristics of the measured and estimated by regression diurnal average wind speeds at Hidasnémeti

	10 m		20 m	
	measured	**estimated**	**measured**	**estimated**
average	3.2	3.2	3.4	3.4
standard deviation.	1.71	1.38	1.49	1.22
coefficient of variation	0.54	0.44	0.44	0.35
minimum	1.0	1.2	0.9	1.7
maximum	12.2	9.6	10.1	9.1
lower quartile	2.1	2.2	2.4	2.6
median	2.7	2.8	3.0	3.1
upper quartile	3.6	3.8	4.0	4.0
skewness	2.20	1.42	1.63	1.42
kurtosis	6.03	2.30	3.29	2.30

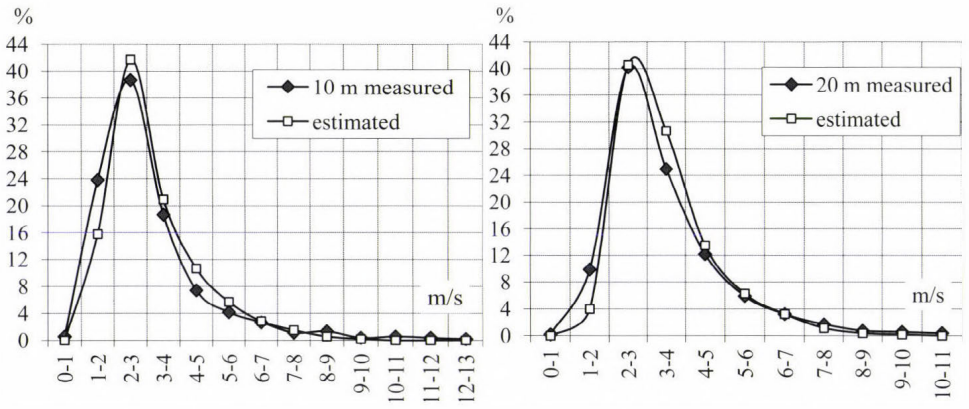

Fig. 10. Distribution of measured and estimated values of diurnal average wind speeds at 10 and 20 m heights at Hidasnémeti.

4. Supplementary investigations (biomass, social aspects)

The local support and biomass potential in the Hernád Valley were also examinated, because they are essentials for the future establishment of the renewables in the area. Results of an own questionnaire attitude survey show

that more than 80% of citizens (1,188 persons) questioned in 21 of the total 30 settlements have heard about wind and solar energy. Majority of citizens interviewed consider wind turbines, low capacity wind generators, and solar panels as acceptable, morally supportable, and realizable. However, only 10 % of citizens interviewed would tolerate a biomass burning power plant or a small heat generating power plant in their own settlement (*Tóth*, 2011; *Tóth* et al. 2012). Based on the estimations for biomass potential, about 125,000 tons of wood and herb biomass suitable for energy production is being produced annually in the study area after satisfying raw material and other demands. The estimated value of that mass is 4.4 billion forints, while bioenergy end products cost 7.8–8.6 billion forints. Approximately 75% of it remains in the region (*Bai*, 2012). All of these shows that not only solar and wind energy but bioenergy potential has also great importance in the Hernád Valley, but attitude of local inhabitants for bioenergy is not as positive as for the sun- and wind energy. Details of these results have already been published in another article.

5. Discussion

Solar energy potential of the Hernád Valley has been evaluated in the course of our examinations on the base of measured data by GIS tools. It can be stated that the region have significant solar energy potential with a total solar radiation income of 1204.8 kWh/m^2 measured at the weather station of Kosice during the studied period, what can be even higher in areas of advantageous exposition. This endowment can serve as a good base for further development of solar energy utilization in the region. Solar energy can be introduced in some new fields like ecologic and silvicultural applications.

Northerly and the opposite southerly winds are the most frequent in the upper part of the Hernád Valley near the Hungarian-Slovakian border. Highest wind speeds belong to northern-northeastern and southern-southeastern directions. Turbulence intensity calculated on the base of standard deviation of wind speeds reaches its maximum when winds blow from the southeastern and western wind directions. Wind energy potential maps of the Hernád Valley have been generated for heights of 50, 80, and 110 meters show that the Hungarian section of the Hernád Valley lays in wind shadow of the bordering mountain ridges. In the case of the model, the annual mean wind speeds weighted by wind direction distribution reach 2.8–3 m/s and 3.5–4 m/s in the northern and southern part of the Hungarian section of the Hernád Valley at heights of 50 and 110 meters. Energy content of air flows is low (nearly 60 W/m^2) at 50 meters. However, the lower part of the Hernád Valley, south of the settlement of Encs and the western side of the valley rising toward the Cserehát hills seem to be suitable for wind energy utilization. Highest wind speeds can be found over the

ridges over 1,000 meters bordering the basin of Kosice and the peaks in the Eperjes-Tokaj Mountains on the east side of the valley.

On the base of wind measurements carried out in Hidasnémeti between April 23, 2010 and April 27, 2012 it can be stated, that wind potential of the year 2011 was far behind the Hungarian annual average. It has been found that the software pack used for the spatial extrapolation of wind speeds is suitable for surveying wind energy potential of the Hernád Valley and its broader environment, and for fulfilling the tasks of the project (*Bíróné Kircsi* and *Vass*, 2011). Our examinations have showed that in spite of temporal fluctuations, utilization of wind energy in the study area can be expedient and effective, especially in the case of application of low starting speed wind turbines.

Not only solar and wind energy but bioenergy potential has also great importance in the Hernád Valley but the attitude of local inhabitants for bioenergy is not as positive as for the sun- and wind energy.

Acknowledgements: The authors thank the Hungarian Scientific Research Fund (OTKA K 75794) for the support of the research.

References

Bai, A., 2012: Az energetikai célú biomassza hasznosításának társadalmi-gazdasági kérdései a Hernád-völgyben. In: A megújuló energiaforrások hasznosításának természeti, társadalmi és gazdasági lehetőségei a Hernád-völgyben. Debreceni Egyetem Meteorológiai Tanszék, 47–60. (in Hungarian)

*Bartók, B., Imecs, Z.,*and *Tar, K.*, 2011: Modelling radiation conditions at Hernád Valley in GIS environment. *Collegium Geographicum 8, Special Edition,* Abel Publishing House, Cluj Napoca, 59–63.

Bíróné Kircsi, A., Tar, K., and *Lázár I.*, 2011: Módszer a szélenergia potenciál meghatározására a Hernád-völgy példáján. II. Környezet és energia konferencia, DAB Megújuló Energetikai Munkabizottság, Debreceni Egyetem Földtudományi Intézet, 160–166. (in Hungarian)

Bíróné Kircsi, A. and *Vass R.*, 2011: A térinformatika alkalmazása a Hernád-völgy szélenergia potenciáljának felmérésében. In: Az elmélet és a gyakorlat találkozása a térinformatikában. II. Térinformatikai konferencia és szakkiállítás, 311–318. (in Hungarian)

Castro, F., Palma, J.M.L.M, and *Lopes, A,S.*, 2003: Simulation of the Askervein flow. Part 1: Reynolds averaged Navier-Stokes equations (k-epsilon turbulence model). *Bound-lay. meteorol. 107*, 501–530.

Dobi, I. and *Mika, J.*, 2007: Adalékok a nap- és szélenergia felhasználásához az IPCC 2007. évi negyedik jelentéséhez kapcsolódva. Kedvező széllel Kunhegyestől Debrecenig. Tiszteletkötet Dr. Tar Károly 60. születésnapjára,101–109. (in Hungarian)

Farr, T.G., Rosen, P.A., Caro, E., Crippen, R., Duren, R., Hensley, S., Kobrick, M., Paller, M., Rodriguez, E., Roth, L., Seal, D., Shaffer, S., Shimada, J., Umland, J., Werner, M., Oskin, M., Burbank, D., and *Alsdorf, D.*, 2007: The shuttle radar topography mission. *Rev. geophys.* 45 art. No.-RG2004.

Kircsi, A. and *Tar, K.* (2008): Profile-tests for utilizing wind energy. *Acta Silvatica & Lignaria Hungarica 4*, 107–123.

Kircsi, A., 2011: The regional extrapolation of wind speed in the Hernád Valley. *Collegium Geographicum 8.* Special Edition, Abel Publishing House, Cluj Napoca, 73–77.

Lopes, A.S, Palma, J.M.L.M., and *Castro, F.A.*, 2007: Simulation of the asker vein flow. Part 2: Large-eddy simulations. *Bound-lay. meteorol. 125*, 85-108.

Radics, K., 2003: A szélenergia hasznosításának lehetőségei Magyarországon: hazánk szélklímája, a rendelkezésre álló szélenergia becslése és modellezése. Doktori (PhD) értekezés, ELTE, Budapest. (in Hungarian)

Tar, K., 2004: Becslési módszerek a magyarországi szélenergia potenciál meghatározására. *Magyar Energetika 12(4)*, 37–48. (in Hungarian)

Tar, K., 2007: Módszerek a magyarországi szélenergia potenciál becslésére. *Dissertationes Savarienses 44,* Societas Scentiarium Savariensis, Savaria University Press, Szombathely. (in Hungarian)

Tar, K., 2009: A potenciális szélenergia mennyiségének függése a magasságtól és kapcsolata a front-típusokkal. Változó Föld, változó társadalom, változó ismeretszerzés. Tudományos Konferencia, Eger, 148–158. (in Hungarian)

Tar, K., 2011a: Előtanulmány Hernád-völgy szélenergiájához. Geográfiai folyamatok térben és időben. Tanulmánykötet Dr. Hanusz Árpád 65. születésnapja tiszteletére. Nyíregyháza, 421–431. (in Hungarian)

Tar, K., 2011b: A Hernád-völgy szélenergiája.. In: (Eds. *Frisnyák, S., Gál, A.*) A magyarországi Hernád-völgy. Földrajzi tanulmányok. Nyíregyháza–Szerencs, 55–69 (in Hungarian)

Tar, K., 2012: Szélklimatológiai vizsgálatok a Hernád-völgyben. In: A megújuló energiaforrások hasznosításának természeti, társadalmi és gazdasági lehetőségei a Hernád-völgyben. Debreceni Egyetem Meteorológiai Tanszék, 21–31. (in Hungarian)

Tar, K., Kircsi, A., Szegedi, S., Tóth, T., Vass, R., and *Kapocska, L.*, 2011: Investigation of the wind power potential of the Hernád valley. *AGD Landsc. Environ. 5*, 93–107.

Tóth, T., 2011: A megújuló energiaforrások hasznosításának feltételei a Hernád völgyében. – In: A magyarországi Hernád-völgy. Földrajzi tanulmányok. Nyíregyházi Főiskola Természettudományi és Informatikai Kar Turizmus és Földrajztudományi Intézet, Nyíregyháza–Szerencs. 267–276. (in Hungarian)

Tóth, T., Szalontai, L., Spéder, F., and *Vass R.*, 2012: A biomassza hasznosításának társadalmi megítélése a Hernád völgyében. In: A megújuló energiaforrások hasznosításának természeti, társadalmi és gazdasági lehetőségei a Hernád-völgyben. Debreceni Egyetem Meteorológiai Tanszék, 61–72. (in Hungarian)

Vince, I., 1975: Matematikai statisztika ipari alkalmazásokkal. Műszaki Könyvkiadó, Budapest. (in Hungarian)

http://re.jrc.ec.europa.eu

http://ncdc.noaa.gov/oa/ncdc.html

IDŐJÁRÁS

VOLUME 119 * 2015

BUDAPEST, HUNGARY

AUTHOR INDEX

TABLE OF CONTENTS

I. Papers

II. News

SUBJECT INDEX

D

E

F

G

H

I

L

M

N

O

P

R

S

T

U

V

W

INSTRUCTIONS TO AUTHORS OF *IDŐJÁRÁS*

The purpose of the journal is to publish papers in any field of meteorology and atmosphere related scientific areas. These may be

- research papers on new results of scientific investigations,
- critical review articles summarizing the current state of art of a certain topic,
- short contributions dealing with a particular question.

Some issues contain "News" and "Book review", therefore, such contributions are also welcome. The papers must be in American English and should be checked by a native speaker if necessary.

Authors are requested to send their manuscripts to

Editor-in Chief of IDŐJÁRÁS
P.O. Box 38, H-1525 Budapest, Hungary
E-mail: journal.idojaras@met.hu

including all illustrations. MS Word format is preferred in electronic submission. Papers will then be reviewed normally by two independent referees, who remain unidentified for the author(s). The Editor-in-Chief will inform the author(s) whether or not the paper is acceptable for publication, and what modifications, if any, are necessary.

Please, follow the order given below when typing manuscripts.

Title page: should consist of the title, the name(s) of the author(s), their affiliation(s) including full postal and e-mail address(es). In case of more than one author, the corresponding author must be identified.

Abstract: should contain the purpose, the applied data and methods as well as the basic conclusion(s) of the paper.

Key-words: must be included (from 5 to 10) to help to classify the topic.

Text: has to be typed in single spacing on an A4 size paper using 14 pt Times New Roman font if possible. Use of S.I. units are expected, and the use of negative exponent is preferred to fractional sign. Mathematical formulae are expected to be as simple as possible and numbered in parentheses at the right margin.

All publications cited in the text should be presented in the *list of references*, arranged in alphabetical order. For an article: name(s) of author(s) in Italics, year, title of article, name of journal, volume, number (the latter two in Italics) and pages. E.g., *Nathan, K.K.,* 1986: A note on the relationship between photosynthetically active radiation and cloud amount. *Időjárás 90,* 10-13. For a book: name(s) of author(s), year, title of the book (all in Italics except the year), publisher and place of publication. E.g., *Junge, C.E.,* 1963: *Air Chemistry and Radioactivity.* Academic Press, New York and London. Reference in the text should contain the name(s) of the author(s) in Italics and year of publication. E.g., in the case of one author: *Miller* (1989); in the case of two authors: *Gamov* and *Cleveland* (1973); and if there are more than two authors: *Smith et al.* (1990). If the name of the author cannot be fitted into the text: *(Miller,* 1989); etc. When referring papers published in the same year by the same author, letters a, b, c, etc. should follow the year of publication.

Tables should be marked by Arabic numbers and printed in separate sheets with their numbers and legends given below them. Avoid too lengthy or complicated tables, or tables duplicating results given in other form in the manuscript (e.g., graphs).

Figures should also be marked with Arabic numbers and printed in black and white or color (under special arrangement) in separate sheets with their numbers and captions given below them. JPG, TIF, GIF, BMP or PNG formats should be used for electronic artwork submission.

More information for authors is available: journal.idojaras@met.hu

Published by the Hungarian Meteorological Service

Budapest, Hungary

INDEX 26 361

HU ISSN 0324-6329